Université de Neuchâtel
Institut de Microtechnique

Advanced Label-free Biochemical Sensors Based on Integrated Optical Waveguide Gratings

Theory, Modeling, Design and Characterization

Thèse

Présentée à la faculté des sciences
Pour obtenir le grade de docteur ès sciences
par

Kaspar Cottier

Neuchâtel, Mai 2004

IMPRIMATUR POUR LA THESE

Advanced Label-free Biochemical Sensors Based on Integrated Optical Waveguide Gratings

M. Kaspar COTTIER

UNIVERSITE DE NEUCHATEL

FACULTE DES SCIENCES

La Faculté des sciences de l'Université de Neuchâtel, sur le rapport des membres du jury

MM. H.-P. Herzig (directeur de thèse),
R. Dändliker, P. Seitz, R. Kunz (CSEM, Neuchâtel)
et A. Tishchenko (St-Etienne F)

autorise l'impression de la présente thèse.

Neuchâtel, le 22 juin 2004

La doyenne:

Martine Rahier

Preface

The present thesis is a result of my research at the Centre Suisse d'Electronique et de Microtechnique (CSEM) S.A. The work covered both theoretical and experimental aspects of biochemical sensors based on waveguide gratings. The emphasis of the thesis is on the development of efficient numerical models that can be readily applied to practical engineering tasks such as design and analysis of waveguide grating devices.

This work would not have been possible without the support of many people. I would like to express my profound gratitude to all of them, whether or not they have been directly involved with the work described here.
The first person I want to thank is my supervisor at CSEM, Rino E. Kunz, for his willingness to share his great expertise in the field of integrated optics and for his never-ending support and motivation. The many fruitful discussions we had during these years created a very pleasant memory for me. Then, I want to thank Guy Voirin for organizing the activities of the workgroup, for his expertise, and for his availability and patience. Eric Bernard and Réal Ischer complete the "Bio-Instruments" team; I want to thank them for their most valuable help and expertise in the fields of mechanics and electronics. Working within this team was a great pleasure.
I would also like to thank Hans Peter Herzig of the IMT at the University of Neuchâtel and Peter Seitz at CSEM for their general support, and with René Dändliker and Alexandre Tishchenko for accepting to be part of the jury.
Among the project partners, I want to thank especially Max Wiki at UNAXIS Balzers, Ltd. (Division Optics) for his support with respect to chip fabrication.
Very special thanks go to Ross Stanley, first for his disposition to share his knowledge of physics and for correcting some manuscripts.
More people from CSEM at Neuchâtel, to whom I owe many thanks are: Gérald Besson and Laurent Beynon at the mechanical workshop for realizing mechanical parts; Véronique Monnier and Fabrice Kohler for support in experimental work; Joël Brulliard for his support and patience with intellectual property questions; Johanna Neumayer for her enthusiasm and sense of the market; Hans Sigrist, Hui Chai Gao, Silvia Angeloni and François Crevoisier from CSEM/Arrayon for their expertise and help in biochemistry, and Eduardo Santoli for his kindness and help.

Last but not least, I would like to thank my superiors at CSEM (in inverted hierarchical order), Raphael Pugin, Harry Heinzelmann, Thomas Hinderling, and of course the members of the nano community for their friendship and support, namely Nicolas Blondiaux, Caterina Minelli, Myriam Losson, Rolf Eckert, Sivashankar Krishnamoorthy, André Meister, Christian Hinderling and Martha Liley.

At this point, I would also like to thank my parents, my sister, my other relatives as well as my friends for their interest, support, patience and simply for their presence.

Table of Contents

Abstract

Sensors based on waveguide gratings have proved their suitability to high sensitivity bio-chemical sensing tasks. Application fields include medical diagnostics, pharmaceutical drug screening, environmental sensing and food quality control. Recent developments led to instruments, which excel in sensitivity and robustness.

The present work introduces novel approaches for modeling such sensor devices. The methods are efficient, adapted to practical engineering tasks, and have short implementation and calculation times. The application of the different methods to the design and characterization of advanced waveguide grating sensors are presented.

A first approach consists in enhancing a set of well-known methods to include the impact of birefringent materials and parasitic substrate reflections. The development of the methods is presented in detail, together with simulations showing parameter dependencies of practical relevance. As an example, a basic requirement in sensor design is maximum sensitivity to the measurand together with minimal sensitivity to parasitic effects, such as ambient temperature changes.

The most important novelty described in the present work is the Local Interference Method (LIME). This method is a rapid approximate calculation scheme for modeling the resonance line shape of non-trivial waveguide grating configurations. Its development was motivated by the lack of practical modeling methods for such structures. The successful application of the algorithm to a difficult analysis task of a non-uniform waveguide grating is presented.

The benefits of the work are illustrated by the results obtained with enhanced sensor designs. Furthermore, an instrument is presented that was developed in the framework of this thesis, implementing some of the above-mentioned methods for the analysis of waveguide gratings in the production process.

Chapter 1

Introduction

The highly sensitive detection of molecular binding events in liquid has become a major area of interest in the past years. It has been mainly driven by the demand of the pharmaceutical industry, as the detection of molecular interactions finds a wide range of applications throughout the process of drug development. Examples are the characterization of specific drug-target interactions and the screening of drug candidates [1], traditionally performed by systems using fluorescent, radioactive or light absorbing markers. These labels are bound to a suitable molecule with a high affinity to the target molecule. A binding event is displayed by the presence of the marker. Despite their high sensitivity - with a detection limit of a fraction of a part per billion (ppb) for advanced systems - methods requiring a labeling have inherent disadvantages, as is expressed in [1]:

> At present, most screens that are used in drug discovery require some type of fluorescent labelling or radiolabelling to report the binding of a ligand to its receptor. This labelling step imposes extra time and cost demands, and can in some cases interfere with the molecular interaction by occluding a binding site, which leads to false negatives. Fluorescent compounds are invariably hydrophobic, and in many screens, background binding is a significant problem, leading to false positives. Ideally, a biosensor-based screening platform should be label-free, sensitive and have sufficient throughput to be widely applicable in drug discovery.

For this reason, the trend in systems for molecular interaction detection has turned towards label-free systems in recent years. Label-free sensors based on planar waveguides are amongst the most promising candidates for future detection systems. They provide not only yes-or-no answers, but detailed information about affinity, specificity and rate of binding through time-resolved monitoring of the binding processes.

The most important application fields include the above-mentioned pharmaceutical industry, medical diagnostics, food quality control and environmental sensors. For the pharmaceutical industry, a high throughput, i.e. a high number of tests per day, is important, as well as the compatibility with existing equipment for fluid handling and sample preparation. Detection systems

should be compatible with the well-known microtiterplate format. In medical diagnostics, food quality control and environmental sensors, the emphasis is often on portable and easy-to-use instruments. The instrument is ideally carried to the sample. In all applications, the required cost and time per test are important issues.

The most widespread label-free detection systems found on the market are based on surface-plasmon resonance (SPR) [2] [3]. Biochemical interactions at the sensor surface are monitored by observing the resonant behavior of guided waves at a thin metal film. Today, the market leader is the company BIACORE [4]. Other companies include Applied Biosystems [5] and Texas instruments [6]. SRU Biosystems [7] is a company selling instruments using waveguide gratings as discussed in this thesis. Other technologies found on the market include polarization interferometric sensors [8] quartz crystal microbalance [9] [10] and mass spectrometry [11].

Interesting approaches found in the scientific literature and making use of dielectric waveguides include Optical Waveguide Lightmode Spectroscopy (OWLS) [12] [13], Mach-Zehnder [14], and Young interferometers [15] [16]. Other methods are based on Resonant Mirrors [17], Reflectometric interference spectroscopy (RifS) [18], Scanning Angle Reflectometry (SAR) [19], Surface Acoustic Waves (SAW) [20], and of course fully electrical devices.

The main advantage of planar dielectric waveguides over SPR devices for label-free detection lies in the enhanced degrees of freedom for sensor design. In both technologies, the penetration depth of guided waves at the sensor interface is directly related to the geometrical extent of the measurement volume, where sensitivity is high. For SPR systems, this parameter is given by the material properties, with a typical penetration depth of around 200 nanometers [21]. In the case of planar dielectric waveguides, this property can be chosen by design, enhancing the application fields to the detection of relatively large objects in the micrometer range, such as cells [22]. This property is detailed in section 5.2 of this thesis.
Furthermore, the absence of a metal film can be an advantage, for instance when combining label-free with luminescent detection. Energy transfers to the metal film (which is called quenching effect) make the combination of luminescence and SPR sensors impractical at least in the classic configuration, while dielectric waveguides are used successfully to enhance the sensitivity of fluorescent sensors [23].
An other advantage of biochemical sensors based on waveguide gratings is their suitability for building sensor arrays with a high number of different sensing regions present on the same chip. This facilitates the detection of several target molecule types simultaneously present in an analyte solution, which is a key requirement for biochemical sensors in all application fields.

The story of integrated optical sensors using waveguide gratings began in 1983, when Lukosz and Tiefentaler reported the application of such structures to humidity and gas sensing [24]. With the perspective of highly sensitive, fast response, small size and low cost devices, research on this topic has been started in 1988 in Zürich by Rino E. Kunz, first at the Paul Scherrer Institute (PSI) which was incorporated 1997 into the Centre Suisse d'Electronique et de microtechnique (CSEM) S.A.. Major developments that resulted from the early work were the "Light pointer" sensing scheme making use of chirped gratings, and the cost effective production of replicated polymer substrates [25] [26]. With the upcoming of wavelength-tunable Vertical Cavity Surface Emitting Lasers (VCSELs), a novel highly sensitive approach has been developed at CSEM, the "wavelength-interrogated optical sensor" (WIOS) [27] [28]. In addition, using sensor chips on glass instead of polymer substrates [29], the stability and reproducibility of the measurements increased markedly.

The work on waveguide grating sensors at CSEM has now shifted from basic research on laboratory set-ups and demonstrators to the development and fabrication of robust instruments that meet the requirements for a commercial product. In collaboration with several industrial partners, the WIOS sensing scheme is implemented into instruments, and the sensor chips are produced in large quantities. In addition, the next generation of devices is prepared by exploring new sensing schemes, materials and fabrication methods.

In this context, my work aimed primarily at the design and characterization of advanced sensor platforms, and the development of the corresponding tools. The present thesis covers this aspect. However, some of the content has been restricted in order to preserve the interests of both the industrial partners and CSEM. For the same reason, none of the work that has been done on advanced sensing schemes is mentioned in this document. Not mentioned either are many experimental aspects, which have been summarized by Cottier et al. in the publications [27] and [29], reprinted in appendix A and B of the present thesis, respectively.

For the design and analysis of waveguide-grating devices, efficient modeling tools are required. Analytical approximations (see Chapter 3) are sufficient for many practical engineering questions, such as resonance peak position, sensitivity, or estimates of temperature drift. Other tasks such as the determination of fabrication tolerances require more detailed modeling techniques. As an example, it has been observed [29] that extremely small non-uniformities due to fabrication errors can significantly distort the signal shapes, a phenomenon which can not be predicted with the above mentioned approximations. More sophisticated methods are required for explaining these phenomena and for adjusting fabrication tolerances in consequence. Commercially available software packages and conventional calculation

methods are not suited to the problem, and have in general long implementation or calculation times. The Local Interference Method (LIME) developed in the framework of this thesis and presented in section 4.3 is an efficient method to estimate the resonance line shape of non-uniform waveguide gratings and has been successfully applied to practical design and analysis tasks.

In Chapter 2, the basic working principle of waveguide grating sensors is explained, and the different existing read out schemes are discussed. In Chapter 3, the theoretical background is presented that is the basis for modeling the behavior of waveguide grating sensors. It includes the detailed description of multilayer waveguides having a certain anisotropy, and a qualitative description of waveguide grating output couplers using a scalar approach. The methods and tools developed in the framework of this thesis for the numerical modeling of waveguide grating sensors are presented in Chapter 4, and Chapter 5 contains a number of simulation results that have been obtained using these tools. Finally, the design and testing of optimized waveguide grating sensors is described in Chapter 6, followed by conclusions and a short outlook.

Chapter 2

Sensing principle

An optical transducer is the heart of the detection system. It relates optical changes at its interface with the analyte medium to a detectable measuring variable. The changes at the interface include for instance refractive index variations, or thickness changes of a molecule layer. A resonant structure allows the amplification of tiny variations into signals that can be readily detected. The measuring variable may be for instance the wavelength or incidence angle of the input light beam.

The optical transducer is composed of two parts: a waveguide and a grating. A monomode waveguide is used as the primary resonant structure. It is composed of a very thin, high-refractive index layer on a transparent support. Light can be guided inside this layer through total internal reflection, as is done in optical fibers for telecommunication. The phase velocity of the guided light, characterized by the propagation constant, depends on the surrounding media. A change in optical properties of the latter therefore translates into a change of the propagation constant.

The grating is used to probe the propagation constant. It consists of a periodic variation of waveguide thickness or refractive index. This periodic structure allows one to couple light waves into or out of the waveguide at the resonance condition. This condition relates the waveguide's propagation constant and grating periodicity to the angle of the plane wave, for which coupling occurs at a certain wavelength. In a practical implementation, the coupling of an incident light beam into the waveguide is observed. In this case, the sensor is in the input configuration. Alternatively, light already present in the waveguide can be extracted through a grating, whose coupling condition is observed. In that case, the sensor is in the output configuration.

The sensing principle applies to two main measurement configurations. The first is called bulk refractive index sensing (refractive index of the cover medium n_c), and is illustrated in Figure 2.1(a). The second concerns measuring thickness h_l and/or refractive index n_l changes of a (bio-chemical) adlayer at the waveguide surface (Figure 2.1(b)). A sensor optimized for the second configuration allows

measuring tiny quantities of target molecules in solutions, being adsorbed to the transducer's surface. The quantity to be measured is in this case the surface mass coverage Γ of the molecules, measured in pg/mm^2 [30].

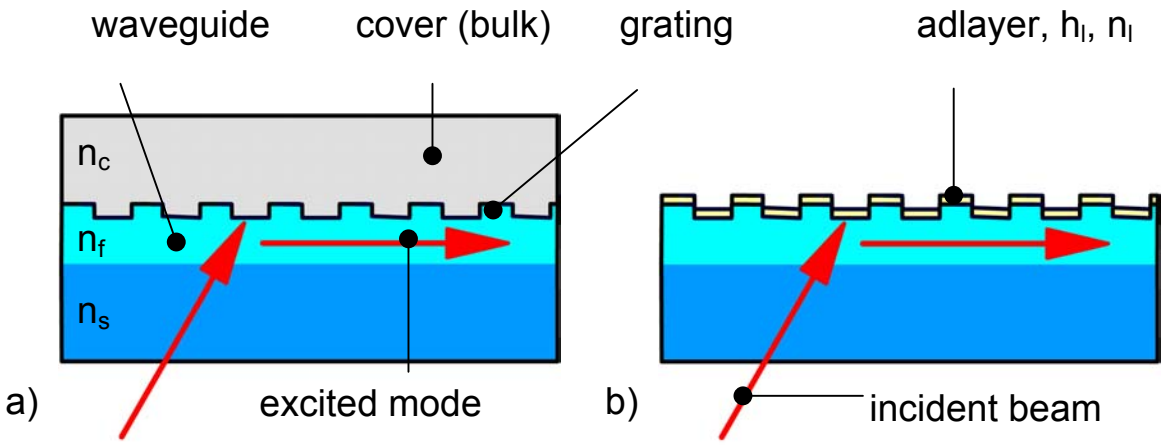

Figure 2.1: (a) Bulk refractive index sensing and (b) adlayer sensing, both in the input configuration.

2.1 Sensing layer

For the detection of small quantities of a given substance, the waveguide surface has to be functionalized in order to specifically bind the target molecules to it [31]. For each molecule to be analyzed, a specific counterpart is needed. Every molecule, for which a selective counterpart is found, may in principle be measured with the sensor system.
An illustration of the recognition process on the chip surface is given in Figure 2.2. Different sensing layers reacting to different target molecules are present on the same sensor surface.

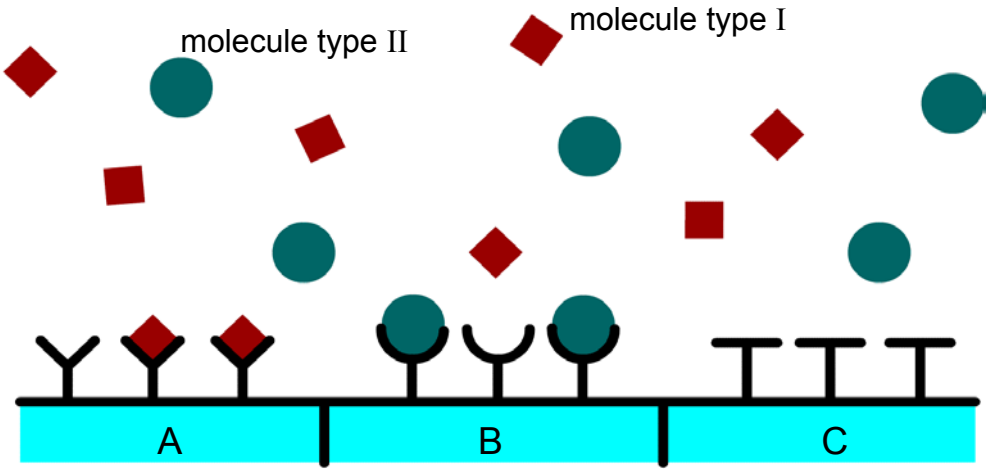

Figure 2.2: Binding of target molecules to a functionalized sensor surface

In this example, sensing region (which is called pad) A attracts the type I, region B the type II molecules. Pad C is passivated, meaning that it should block adsorption of any molecule to the surface. Pad C is therefore the reference sensor. Having a reference signal is of utmost importance, as drift and noise effects acting on all channels simultaneously can be eliminated largely by subtracting the reference [32]. This includes for instance the impact of temperature changes, light source instabilities or changes of the refractive index of the cover medium.

The sensing layer is the layer formed by the recognition and the analyte molecules on the surface. Given the small size of the molecules involved, the optical properties of this layer are well approximated by a dielectric adlayer to the waveguide, having an equivalent index of refraction and thickness. A target molecule binding to the adlayer is then modeled either as refractive index or as thickness change of this layer. The detailed optical model of the molecule deposition is given in section 4.1, where the relations between surface mass coverage and the optical properties of the equivalent layer are presented.

2.2 Sensor arrays

A key application of the waveguide-grating sensors is the detection of several target molecule types simultaneously present in an analyte solution [1], as illustrated in Figure 2.2 by the two molecule types I and II present in the liquid. This requires an array of differently functionalized sensing pads on the same sensor chip.
An advantage of biochemical sensors based on waveguide gratings is their suitability for building such sensor arrays [33]. Figure 2.3 shows a photograph of a sensor platform with 3x8 sensing units. In this example, a sensing unit consists of an input and an output grating. The chip seen in the photograph is designed to be used in a wavelength interrogated optical sensor (WIOS) system. Provided a suitable means of applying the corresponding surface chemistry, each of the sensing units can be functionalized in a different way. With the corresponding readout instrument, the 24 channels can be monitored simultaneously.
Several constraints have to be respected for the design of arrayed waveguide grating sensors. First, the crosstalk of the different sensing pads has to be minimized. For this reason, it is often preferred to introduce a second grating for light extraction (in the case of the input sensing scheme) and directing the light present in the waveguide onto a detector. In the output sensing scheme, the other grating is solely used to excite the waveguide mode. This is illustrated for instance in Figure 2.4 (a) and (b), respectively. A second consideration is the size of the sensing units. A smaller size results in closer packing. However, this is traded against increased crosstalk (or measures for avoiding it) and a larger

resonance peak. These considerations are discussed in the context of chip design in section 6.1.

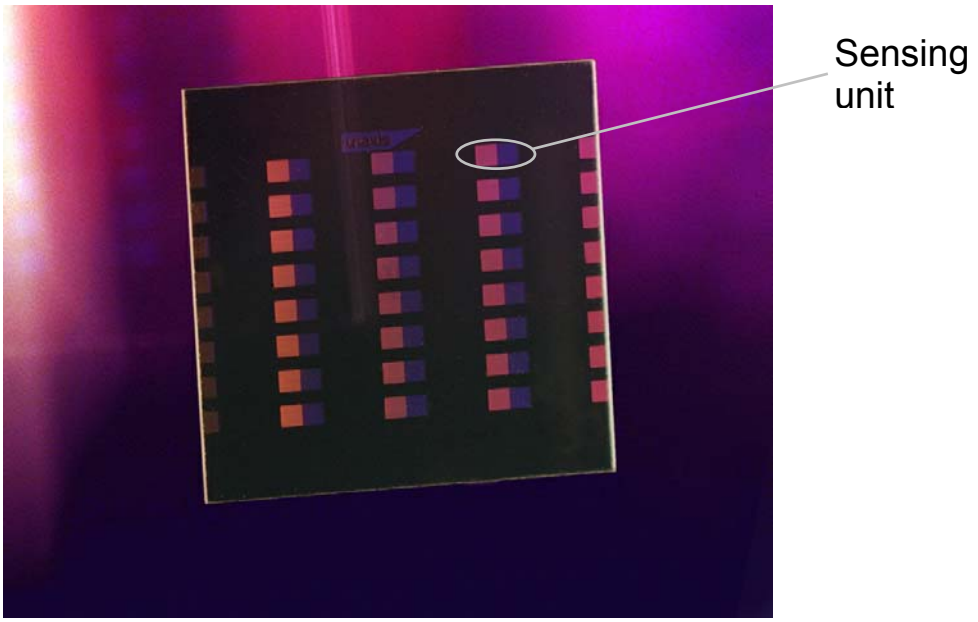

Figure 2.3: photograph of an example sensor array

The number of measurement channels on the chip is determined by the application. While point-of care diagnostic applications usually require a moderate channel number of several dozen, high-throughput screening tasks require up to 1500 channels.

2.3 Readout schemes

A multitude of different configurations can be used for practical implementation of the basic sensing scheme, the latter consisting in probing the propagation constant of a waveguide by means of a grating. The systems can be categorized by their measuring variable. The available parameters are a priori those figuring in the waveguide grating resonance condition: resonance angle, wavelength and grating period.
Furthermore, the sensors can be in either the input or output-sensing configuration. The input-sensing scheme requires in general a sweeping of the parameter of interest, while the output scheme requires its measurement, as will be illustrated in the following sections. The examples show the basic implementation of the readout schemes using two separate gratings for excitation and extraction of the guided mode. Sensing schemes using only one grating pad do also exist [34].

2.3.1 Angular readout

The angular readout is the most intuitive and simple implementation of a waveguide-grating sensor [13]. In its basic input configuration, the incidence angle θ_i of a source having a constant wavelength λ is scanned for determining the resonance condition. In the output configuration, a position-sensitive detector (e.g. a camera) is placed at the sensor grating in order to measure the resonance angle. In both cases, it is useful to have a second grating for extracting the light or exciting the waveguide mode, as is illustrated in Figure 2.4 (a) and (b), respectively.
The advantages of this type of sensor in the input configuration are the relatively simple implementation and the large measurement range. The measurement speed and resolution are limited by the mechanical movement. The output configuration on the other side can achieve fast readout without any moving parts, and is limited by the size or resolution of the detector surface, limiting the range or the sensitivity of the sensor, respectively.

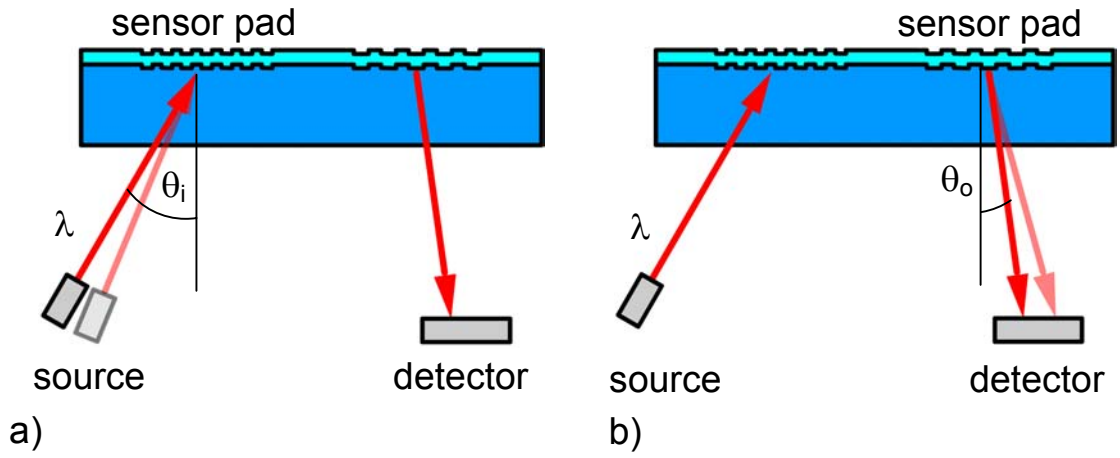

Figure 2.4: Waveguide grating sensor with angular readout in the (a) input and (b) output configuration

2.3.2 Wavelength readout

In the input configuration of the wavelength readout scheme, the wavelength $\lambda(t)$ is continuously scanned in order to monitor the waveguide grating resonance [27]. The latter is visible in the time-dependent modulation of the light excited in the waveguide. Another possibility is to illuminate the grating with a certain spectral width of the incident light, and to analyze the wavelength of the excited mode [34].
In the output configuration, the wavelength of the light exiting the grating under a specific angle $\lambda(\theta)$ is determined by means of a spectrometer. For this configuration to work, the mode has to be excited with a certain spectral width $\Delta\lambda$. Figure 2.5 illustrates the two configurations.

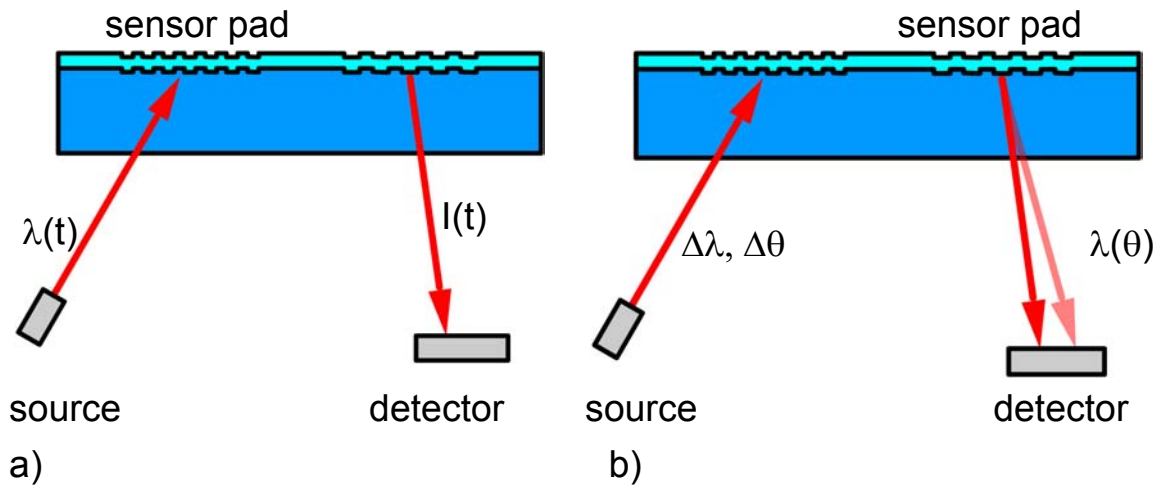

Figure 2.5: Wavelength readout in the input (a) and output (b) configuration.

Using a wavelength-tunable semiconductor laser diode, the input configuration has its advantages over angular schemes with respect to readout speed and resolution. The measurement range, however, is limited by the tuning range of the laser.
The configurations using wavelength analyzers are limited by the properties of the latter. Very sensitive devices with a high range can be built, but they are in general costly and are in principle not suited for large arrays, because for each channel, a separate spectrometer is required.

2.3.3 Variable grating period

Slightly more exotic sensor systems are the configurations using a spatial variation of the waveguide-grating periodicity [25]. Figure 2.6 shows the chip layout of such a sensor, where both input and output gratings have the same variation of the period $\Lambda=\Lambda(y)$. The waveguide-grating resonance takes place at a given location y of the sensor, which can be detected by a camera and image processing tools analyzing the intensity distribution I(y) of the excited mode.
The performance of the system is mostly limited by fabrication tolerances and spatial variations of the biochemical processes that are observed.

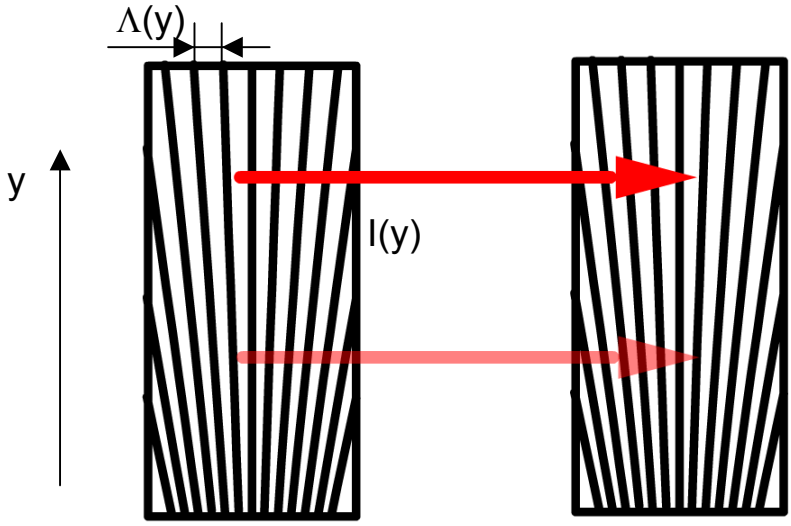

Figure 2.6: Waveguide grating sensor having a spatial variation Λ=Λ(y) of the grating period resulting in a spatial variation I(y) of the mode intensity.

Chapter 3

Theory

In this section, an approximate analytic treatment of waveguide gratings is presented as a basis for analyzing their properties. Figure 3.1 summarizes the process to be described for the case of an input-sensing device. A monochromatic wave excites the waveguide mode through a grating at the resonance condition. This condition is modified by optical changes near the waveguide surface, such as adlayer growth or refractive index changes. The theoretical treatment shall be limited to the optical transducer, i.e. assuming ideal light sources and detectors, and simple optical models of the biochemical processes.
The primary design questions to be addressed by the theory are parameter optimization for maximizing sensitivity and minimizing parasitic effects. Other tasks include the definition of fabrication tolerances, the analysis of measurement data, and performance estimation in general.

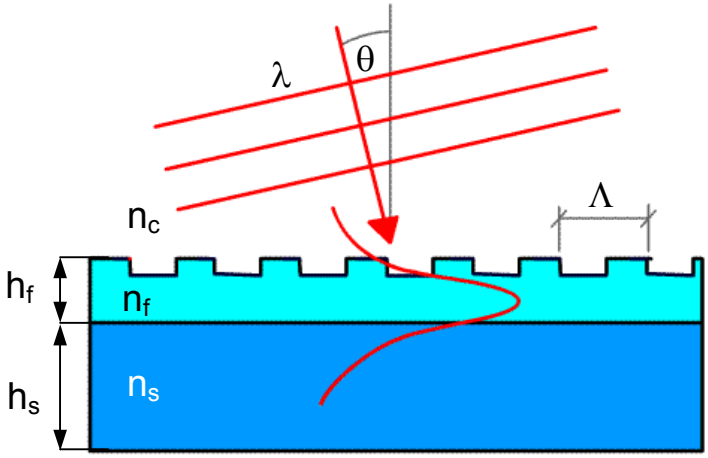

Figure 3.1: Optical transducer.

For many practical engineering tasks, approximate analytical solutions deliver sufficiently exact results. These tasks include for instance the evaluation of sensitivity or temperature drift. The approximate analytical solutions presented

in the next sections are obtained by separating the whole problem into the treatment of an ideal waveguide and the grating.

For a more thorough simulation of the behavior of the system, numerical modeling is required. This is the case if for instance the impact of structural non-uniformities is to be evaluated. Chapter 4 presents the corresponding approximate methods and simulation tools developed during this thesis.

If the exact optical behavior of waveguide grating couplers is to be calculated, rigorous methods are required. A fair number of rigorous and exact methods exist, including rigorous coupled wave analysis (RCWA) also known as the Fourier modal method (FMM) [35] [36] [37], the S-and R-matrix methods [38], the C-Method [39] and the equivalent source method [40], and more exotic methods like the one suggested by Morf in [41].
The methods are in general time-consuming for both implementation and calculation. Furthermore, as the biochemical binding processes can only be modeled in an approximate way due to the complexity of the phenomena involved, the benefits from rigorous calculations do sometimes not justify the expenses for this particular task. For these reasons, these methods have not been applied in the framework of this thesis, and will not be presented.

In section 3.1, a detailed description of multilayer waveguides presenting a certain anisotropy (birefringence oriented along the principle axes of the waveguide) is given, which has been applied in the waveguide grating analysis software presented in section 4.2. A qualitative description of waveguide grating output couplers using Fourier transform spectral analysis is given in section 3.2. The phenomenon of parasitic substrate reflections, which may significantly deteriorate the signal quality, is treated in section 3.3.

3.1 Waveguide modes

The loss-less guiding of light inside a waveguide is made possible through the phenomenon of total internal reflection occurring at interfaces between high index to low index of refraction dielectric materials above a critical angle. Consider a layer of high refractive index, and with a thickness at the wavelength scale, surrounded by lower index media. The multiple internal reflections in this layer, called film, give rise to interference effects. Light can only exist in the confined space upon constructive interference. For this reason – unlike in free space, where light can propagate in every direction - optical waves in waveguides propagate only at a discrete set of states, which are called modes. The modes are characterized by their propagation constant, which is a measure for the speed at which the phase fronts propagate along the structure.
The waveguide-grating structure can be approximated by an equivalent waveguide structure for determining the propagation constant. Using this approach, the presence of the grating regions in the structure can either be neglected (thin grating approximation) or modeled as equivalent layers [42]. These equivalent layers have a thickness corresponding to the thickness of the grating, which can be of surface relief or volume type, and an averaged index of refraction. The resulting waveguide structure consists of homogeneous layers separated by planar interfaces of infinite extent. An example of such a structure is shown in Fig. 3.2, where a grating present at the top and bottom boundary of the film is modeled as grating-equivalent intermediate layers.

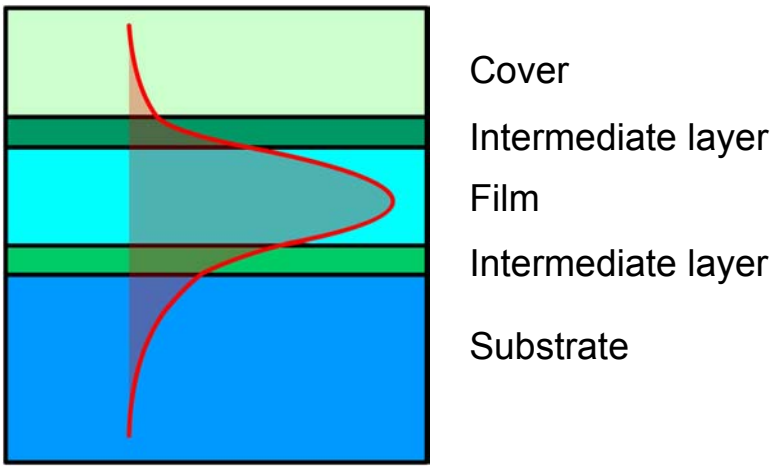

Figure 3.2: Equivalent waveguide structure

The materials are assumed homogenous, without scattering, and uniaxially birefringent with the main axes of the refractive index ellipsoid oriented along the main axes of the waveguide. Figure 3.3 shows the possible configurations for each layer. Material absorption may be included by introducing a non-zero complex component of the refractive index [43].

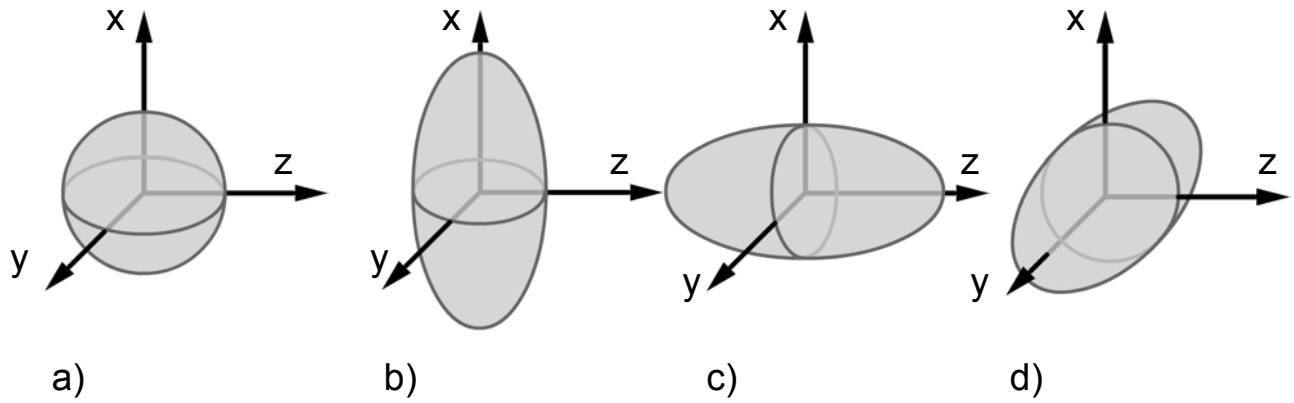

Figure 3.3 Possible orientations of the refractive index ellipsoid for each layer: (a) isotropic, (b) $n_e=n_x$, c) $n_e=n_z$, d) $n_e=n_y$

In summary, each layer is characterized by its thickness and by its complex refractive indices n_x, n_y, n_z. The birefringence is characterized by the ordinary and extraordinary refractive indices n_e and n_o, respectively [43].
In the following sections, the propagation constants of guided modes are determined by solving the electromagnetic boundary conditions for a suitable set of fields. The mode condition will be given in a simple and robust form, where the multilayer structure is reduced to two reflection coefficients.

3.1.1 TE and TM Polarization

The guided-wave phenomena show a polarization dependency, which can be reduced to an analysis of two orthogonal linear polarizations. They are treated separately for the case of an ideal waveguide.
The orientation of the two polarizations is defined by the orientation of the electromagnetic fields of a plane wave with respect to a planar interface. For a TE wave, the electric field ($\mathscr{E}$) oscillates in the plane of the interface. For the TM wave, the same is true for the magnetic field ($\mathscr{H}$). In both cases, the electric and magnetic fields oscillate in the plane perpendicular to the direction of propagation (**k**) of the plane wave. Figure 3.4 illustrates the definition.

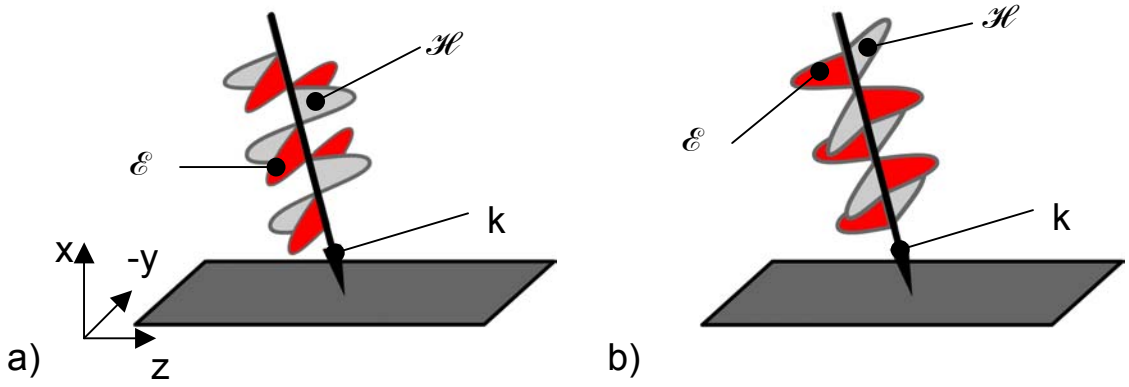

Figure 3.4: Definition of (a) TE and (b) TM waves

3.1.2 Birefringent multilayer slab waveguide

The behavior of electromagnetic fields is described by Maxwell's equations. For monochromatic electromagnetic waves in media that are homogeneous, stationary, non-magnetic, charge and current free and without scattering, the four equations take the forms

$$\nabla \times \boldsymbol{H} = \frac{\partial \boldsymbol{D}}{\partial t} \tag{3.1.1}$$

$$\nabla \times \boldsymbol{E} = -\frac{\partial \boldsymbol{B}}{\partial t} \tag{3.1.2}$$

$$\nabla \cdot \boldsymbol{D} = 0 \tag{3.1.3}$$

$$\nabla \cdot \boldsymbol{B} = 0 \tag{3.1.4}$$

In above equations, the monochromatic waves are described in terms of their complex amplitudes

$$\mathscr{E}(\mathbf{r},t) = \mathrm{Re}\left\{\boldsymbol{E}(r)e^{-i\omega t}\right\} \tag{3.1.5a}$$

$$\mathscr{H}(\mathbf{r},t) = \mathrm{Re}\left\{\boldsymbol{H}(r)e^{-i\omega t}\right\} \tag{3.1.5b}$$

Where $i=\sqrt{-1}$, $\boldsymbol{E}$ is the complex amplitude of the electric field, $\boldsymbol{H}$ is the complex amplitude of the magnetic field, $\boldsymbol{D}$ is the complex amplitude of the electric flux density (or electric displacement), and $\boldsymbol{B}$ is the complex amplitude of the magnetic flux density, the flux densities being defined in a similar way as the complex amplitudes of the electric and magnetic field, respectively. The time dependency of the wave is characterized by the angular frequency $\omega=2\pi\nu$, where ν is the frequency of the oscillation.
Given the planar geometry of the problem, we consider planar waves of the form

$$\boldsymbol{u}(r) = \boldsymbol{u}_0 e^{i\boldsymbol{k}\cdot\boldsymbol{r}} = \boldsymbol{u}_0 e^{i(k_x x + k_z z)} \tag{3.1.6}$$

Where $\boldsymbol{u}$ stands for the complex amplitude of either the electric or the magnetic field, and $\boldsymbol{k}$ is the wavevector. With these assumptions on the position and time dependence of the fields, Maxwell's equations (3.1.1) and (3.1.2) reduce to

$$\boldsymbol{k}\times\boldsymbol{H} = -\omega\boldsymbol{D} \tag{3.1.7a}$$

$$\boldsymbol{k}\times\boldsymbol{E} = \omega\boldsymbol{B} \tag{3.1.7b}$$

It can be seen from eqs (3.1.7a) and (3.1.7b), that the $\boldsymbol{D}$ is normal to $\boldsymbol{k}$ and $\boldsymbol{H}$ and that $\boldsymbol{B}$ is normal to $\boldsymbol{k}$ and $\boldsymbol{E}$. However, $\boldsymbol{D}$ is not necessarily normal to $\boldsymbol{E}$, and therefore, the Poynting vector

$$\boldsymbol{S}=\frac{1}{2}\boldsymbol{E}\times\boldsymbol{H}^* \tag{3.1.8}$$

describing the amplitude and direction of the power flow, is not necessarily parallel to the direction of the wave vector $\boldsymbol{k}$. This is the case for materials presenting an optical anisotropy as illustrated in Figure 3.3. The anisotropy is described by the relation between $\boldsymbol{D}$ and $\boldsymbol{E}$

$$\boldsymbol{D}=\begin{pmatrix} n_x^{\,2} & 0 & 0 \\ 0 & n_y^{\,2} & 0 \\ 0 & 0 & n_z^{\,2} \end{pmatrix}\cdot\varepsilon_0\boldsymbol{E}=\boldsymbol{\varepsilon}\varepsilon_0\boldsymbol{E} \tag{3.1.9}$$

For a non-magnetic material, the relation between $\boldsymbol{H}$ and $\boldsymbol{B}$ is given by

$$\boldsymbol{H}=\mu_0\boldsymbol{B} \tag{3.1.10}$$

Inserting eqs (3.1.9) and (3.1.10) into eqs (3.1.7a) and (3.1.7b), and using $k_0=\omega/c$, where $c=(\mu_0\varepsilon_0)^{-½}$ is the speed of light, yields the wave equation

$$\boldsymbol{k}\times(\boldsymbol{k}\times\boldsymbol{E})+k_0\boldsymbol{\varepsilon}\boldsymbol{E}=\boldsymbol{0} \tag{3.1.11}$$

Furthermore, The definitions of TE and TM polarized waves in the chosen geometry require that

TE: $E_x=0,\ E_z=0 \rightarrow \quad k_y=0,\ H_y=0$ (3.1.12a)

TM: $H_x=0,\ H_z=0 \rightarrow \quad k_y=0,\ E_y=0$ (3.1.12b)

Inserting (3.1.12a) into (3.1.11) leads to

$$k_x^{\,2}=n_y^{\,2}k_0^{\,2}-k_z^{\,2} \tag{3.1.13a}$$

for TE waves. With little more effort, inserting (3.1.12b) into (3.1.11) leads to

$$k_x^{\,2}=\frac{n_z^2}{n_x^2}\left(k_0^{\,2}n_x^2-k_z^{\,2}\right) \tag{3.1.13b}$$

for TM waves. Since eqs (3.1.13a) and (3.1.13b) have two solutions for k_x, the total field inside the waveguiding film is given by

$$u(,z,t) = u^{+}(x,z,t) + u^{-}(x,z,t) = \left(A e^{ik_x(x-x_0)} + B e^{-ik_x(x-x_0)}\right) e^{ik_z z} \tag{3.1.14}$$

with A and B being the complex amplitude of the upwards (u^{+}) and downwards (u^{-}) traveling wave at $x=x_0$, $z=0$, respectively. The field $u(x,z)$ is defined as $u=E_y$ for a TE, and $u=H_y$ for a TM polarization. The upwards and downwards traveling components of the total field are illustrated in Figure 3.5(a).
In order to find the condition for the existence of guided waves, the field is expressed at the top and bottom interface of the film. Without loss of generality, this is done for $z=0$.

At $x=x_0$

$$u(x_0) = A + B \tag{3.1.15}$$

At $x=x_0+h_f$

$$u(h_f) = A e^{ik_x h_f} + B e^{-ik_x h_f} \tag{3.1.16}$$

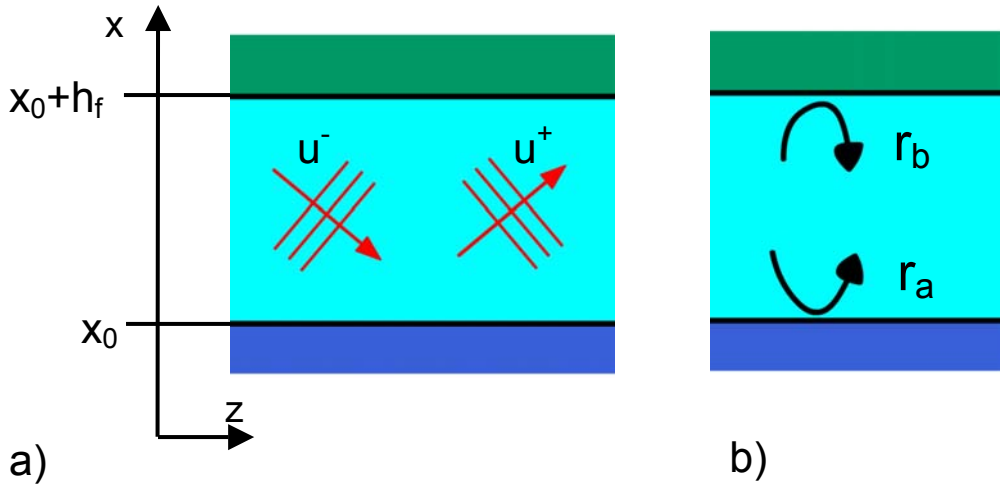

Figure 3.5: (a) Waves inside the waveguiding film, (b) upper and lower reflection coefficients

Regardless of what is behind an interface, the ratio between the upwards and downwards traveling waves at this interface corresponds to the reflection coefficient. Defining r_a as the (complex) reflection coefficient at the lower film interface, and r_b as the reflection coefficient at the upper interface as illustrated in Figure 3.5 (b).

$$r_a = A/B = |r_a| e^{i\varphi_a} \tag{3.1.17}$$

$$r_b = \frac{Be^{-ik_x h_f}}{Ae^{ik_x h_f}} = |r_b| e^{i\varphi_b} \tag{3.1.18}$$

and inserting eqn (3.1.17) into eqn (3.1.18)

$$r_b = \frac{Be^{-ik_x h_f}}{r_a Be^{ik_x h_f}} = \frac{e^{-2ik_x h_f}}{r_a} \tag{3.1.19}$$

results finally in

$$r_a r_b e^{2ik_x h_f} = 1 \tag{3.1.20}$$

This is the condition for the existence of a waveguide mode. It says that the upper reflection coefficient multiplied by the lower reflection coefficient and multiplied by the roundtrip phase perpendicular to the waveguide interfaces must be equal to unity. Taking the imaginary part of eqn (3.1.20)

$$Im\{r_a r_b\} = |r_a| \cdot |r_b| \cdot sin(\varphi_a + \varphi_b + 2k_x h_f) = 0 \tag{3.1.21}$$

Reveals the classic mode equation

$$2 h_f k_x + \varphi_a + \varphi_b = 2\pi m \tag{3.1.22}$$

The propagation constant $\beta = k_z$ and the effective refractive index N of a mode are related by

$$N = \beta / k \tag{3.1.23}$$

respectively. The propagation constant $\beta = k_z$ is calculated from k_x using (3.1.13).

Since the reflection coefficients do not show phase shifts greater or lower than $\pm 2\pi$, the classic mode equation (3.1.22) may lead to problems with the numbering of modes for multilayer systems having thick layers. A second disadvantage of eqn (3.1.22) is its discontinuity.
For these reasons, it was chosen to rather evaluate the imaginary and real parts of eqn (3.1.20) for the implementation of a robust mode search algorithm (see section 4.2).

3.1.3 Reflection coefficient at an interface

The boundary conditions of the Maxwell equations require that at every interface:

$E_{||}$, $H_{||}$ continuous, and
$D_{\perp}$, $B_{\perp}$ continuous

For **TE** modes, the boundary condition require therefore for the given geometry:

E_y continuous and $\frac{\partial E_y}{\partial x}$ continuous

since H_z continuous, $\omega\,\mu_0$ constant and $\frac{\partial E_y}{\partial x} = \omega\,\mu_0\,H_z$.

For **TM** modes,

H_y continuous and $\frac{1}{\varepsilon_z}\cdot\frac{\partial H_y}{\partial x}$ continuous,

since E_z continuous, ω constant and $\frac{\partial H_y}{\partial x} = -\omega\,\varepsilon_z\,E_z$

The boundary value problem can now be solved by means of an Ansatz, which superposes an incident, a reflected, and a transmitted wave (u_i u_r u_t, respectively) at the interface. the following results are obtained for TE and TM modes, respectively:

$$k_{iz} = k_{rz} = k_{tz} \equiv k_z \equiv \beta \tag{3.1.24}$$

$$r_{TE} = \left.\frac{u_r}{u_i}\right|_{x=0} = \frac{k_{ix} - k_{tx}}{k_{ix} + k_{tx}} = \frac{\sqrt{n_{1y}^2 - k_z^2} - \sqrt{n_{2y}^2 - k_z^2}}{\sqrt{n_{1y}^2 - k_z^2} + \sqrt{n_{2y}^2 - k_z^2}} \tag{3.1.25}$$

$$r_{TM} = \left.\frac{u_r}{u_i}\right|_{x=0} = \frac{\varepsilon_{1z}^{-1}\cdot k_{ix} - \varepsilon_{2z}^{-1}\cdot k_{tx}}{\varepsilon_{1z}^{-1}\cdot k_{ix} + \varepsilon_{2z}^{-1}\cdot k_{tx}} = \frac{n_{2x}\cdot n_{2z}\cdot\sqrt{n_{1x}^2 - k_z^2} - n_{1x}\cdot n_{1z}\cdot\sqrt{n_{2x}^2 - k_z^2}}{n_{2x}\cdot n_{2z}\cdot\sqrt{n_{1x}^2 - k_z^2} + n_{1x}\cdot n_{1z}\cdot\sqrt{n_{2x}^2 - k_z^2}} \tag{3.1.26}$$

3.1.4 Reflection coefficient at multiple interfaces

In the following, the calculation of the reflection coefficient of a multilyer structure composed of M+1 interfaces as seen in Fig. 3.6(a) is presented. The coefficient ρ_l describes the reflection from interface l to the end of the stack, while r_l denotes the single-interface reflection coefficient from medium l to medium $l+1$.
Given the above definitions, the overall reflection coefficient ρ_1 is calculated [44] using the recursive formulation

$$\rho_l = \frac{r_l + \rho_{l+1} e^{i2kx_l d_l}}{1 + r_l \rho_{l+1} e^{i2kx_l d_l}} \quad , l=M, M-1, \ldots, 1 \tag{3.1.27}$$

with an initial value of $\rho_{M+1} = r_{M+1}$

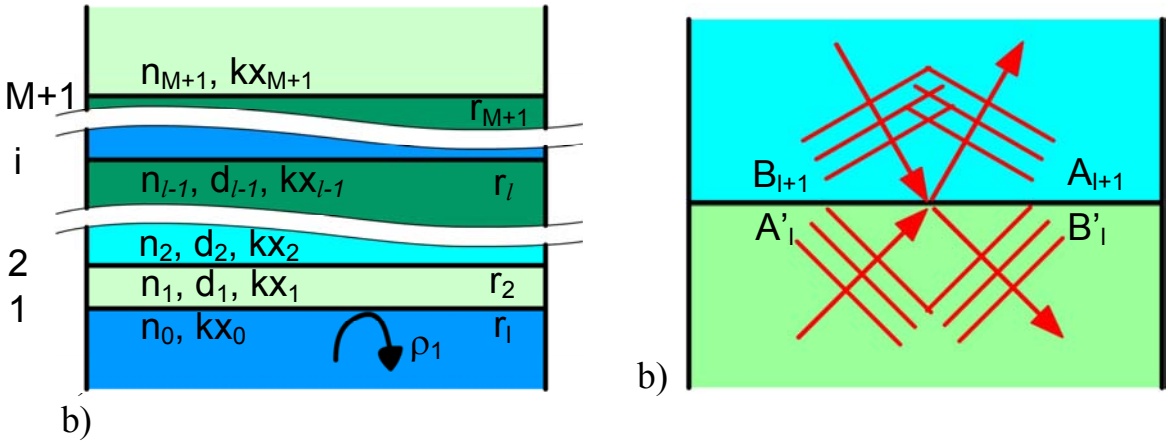

Figure 3.6 (a) Reflection coefficients and (b) wave transmission at multiple interfaces.

3.1.5 Mode intensity profiles and power flow

For calculating the intensity profiles and the power flow, the total field has to be known at any position x inside the structure. In each layer, it is given by (3.1.14), where A and B are given by the boundary conditions.
The procedure for calculating the fields in the whole waveguide is as follows. In the waveguiding film, either A and B are chosen arbitrarily, and the other component is calculated using (3.1.17). For the layers above the film, the two field components are calculated successively:
Given A_l and B_l defined as the complex field amplitude components at the lower interface of layer l, the field components at the upper interface A_l' and B_l' are given by simple propagation of the waves through the layer:

$$A_l' = A_l e^{ikx_l h_l} \tag{3.1.28a}$$

$$B_l' = B_l e^{-ikx_l h_l} \tag{3.1.28b}$$

Using the boundary conditions on the field and its derivative, the components A_{l+1} and B_{l+1} (see Fig. 3.6(b)) for the next layer $l+1$ are given by

$$A_{l+1}=\frac{1}{2}\left[A_l'\left(1+\left(\frac{nx_{l+1}}{nx_l} \right)^{2p} \frac{kx_l}{kx_{l+1}} \right) + B_l'\left(1-\left(\frac{nx_{l+1}}{nx_l} \right)^{2p} \frac{kx_l}{kx_{l+1}} \right) \right] \tag{3.1.29}$$

$$B_{l+1}=A_l'+B_l'-A_{l+1} \tag{3.1.30}$$

Where $p=0$ for TE and $p=1$ for TM polarized waves.
For the layers below the film, the field components after the interface A_{l-1}' and $B\text{-}1_l'$ are first calculated

$$B'_{l-1}=\frac{1}{2}\left[B_l\left(1+\left(\frac{nx_{l+1}}{nx_l} \right)^{2p} \frac{kx_l}{kx_{l+1}} \right) + A_l\left(1-\left(\frac{nx_{l+1}}{nx_l} \right)^{2p} \frac{kx_l}{kx_{l+1}} \right) \right] \tag{3.1.31a}$$

$$A_{l-1}'=B_l+A_l- B'_{l-11} \tag{3.1.31b}$$

Finally, except for the substrate, the fields are defined at the lower layer interface and are calculated using

(3.1.32a)

$$B_l= B_l' e^{-ikx_l h_l}$$

$$A_l= A_l' e^{ikx_l h_l} \tag{3.1.32b}$$

In the case of non-absorptive media, in the substrate: $A_l=0$ and in the cover: $B_l=0$. Note that even if the x-component of the wavevector is imaginary in an intermediate layer, the wave is not evanescent in the classical sense of a purely exponential decay due to the presence of the second field component.
For comparing two structures, it is convenient to normalize the fields to unity power per unit width Δy carried in the mode. It is obtained by integrating over the mode intensity S_z:

$$\Delta P_m = \int_{y=0}^{\Delta y} \int_{x=-\infty}^{\infty} S_z \, dx \, dy = \Delta y \int_{x=-\infty}^{\infty} S_z \, dx \tag{3.1.33}$$

Using eqs (3.1.8) and (3.1.12a), one obtains for the TE polarization

$$S_z = \frac{1}{2} \mathrm{Re}\left\{ E_y \cdot \left(- H_x^* \right) \right\} \tag{3.1.34}$$

Using eqn (3.1.2)

$$H_x = \frac{1}{i\mu_0\omega} \frac{\partial E_y}{\partial z} = \frac{\beta E_y}{\mu_0 \omega}$$

$$S_z = \frac{1}{2} \mathrm{Re}\left\{ E_y \cdot \left(- \frac{\beta}{\mu_0 \omega} E_y^* \right) \right\} = \frac{\beta}{2\mu_0\omega} \left| E_y \right|^2$$

And using the relations

$$\beta = N \cdot k_0, \qquad \omega = \frac{k_0}{\sqrt{\varepsilon_0 \mu_0}} \tag{3.1.35}$$

we obtain finally

$$S_z = \frac{N}{2} \sqrt{\frac{\varepsilon_0}{\mu_0}} \left| E_y \right|^2 \tag{3.1.36a}$$

Using a similar development, the intensity for the TM polarization is found

$$S_z = \frac{N}{2} \sqrt{\frac{\mu_0}{\varepsilon_0}} \frac{1}{n_x^2} \left| H_y \right|^2 \tag{3.1.36b}$$

The total power carried in the waveguide per width element Δy is therefore given by

$$\Delta P_m = \Delta y \int_{x=-\infty}^{\infty} S_z \, dx = c_p \cdot N \cdot \Delta y \cdot \left(\sum_l P_l + P_c + P_s \right) \tag{3.1.37}$$

With P_l the power contribution inside the intermediate layer l, P_s the contribution of the substrate, P_c the contribution of the cover, and

$$c_p = \frac{1}{2}\sqrt{\frac{\varepsilon_0}{\mu_0}}, \quad \text{TE} \tag{3.1.38a}$$

$$c_p = \frac{1}{2}\sqrt{\frac{\mu_0}{\varepsilon_0}}, \quad \text{TM} \tag{3.1.38b}$$

In each layer and for both polarizations, the square of the amplitude of the field as given by (3.1.16) is

$$|u|^2(x) = |A|^2 e^{-2k_x''x} + |B|^2 e^{2k_x''x} + 2|A||B| \cos\left(2k_x' x + \varphi_A - \varphi_B\right) \tag{3.1.39}$$

Where k_x' is the real and k_x'' the imaginary part of the x-component of the k-vector inside layer l. Integration of (2.1.39) reveals for layers with real k_x (n_l>N, no absorption):

$$P_l \cdot {n_{xl}}^{2p} = \left(|A|^2 + |B|^2\right) h_l + \frac{|A||B|\left(\sin\left(2h_l k_x' + \varphi_A - \varphi_B\right) - \sin\left(\varphi_A - \varphi_B\right)\right)}{k_x'} \tag{3.1.40a}$$

For layers with purely imaginary k_x (n_l<N, no absorption):

$$P_l \cdot {n_{xl}}^{2p} = \frac{|A|^2\left(1 - e^{-2h_l k_x''}\right) + |B|^2\left(e^{2h_l k_x''} - 1\right)}{2k_x''} + 2|A||B| h_l \sin\left(\varphi_A - \varphi_B\right) \tag{3.1.40b}$$

And for layers with kx'≠0, kx''≠ 0:

$$P_l \cdot {n_{xl}}^{2p} = \frac{|A|^2\left(1 - e^{-2h_l k_x''}\right) + |B|^2\left(e^{2h_l k_x''} - 1\right)}{2k_x''} + \frac{|A||B|\left(\sin\left(2h_l k_x' + \varphi_A - \varphi_B\right) - \sin\left(\varphi_A - \varphi_B\right)\right)}{k_x'} \tag{3.1.40c}$$

where $\varphi_A = Phase\{A\}$, $\varphi_B = Phase\{B\}$

Assuming true evanescent waves in the cover and substrate ($k_x'=0$), the power carried in the cover and substrate are given by

$$P_c = \frac{|A_c|^2}{2|k_{xc}|n_{xc}^{2p}} \tag{3.1.41a}$$

$$P_s = \frac{|B_s|^2}{2|k_{xs}|n_{xs}^{2p}} \tag{3.1.41b}$$

With $p=0$ for TE, $p=1$ for TM.

For the basic three layer system composed of substrate, film and cover, inserting the reflection coefficients into eqs (3.1.40a), (3.1.41a) and (3.1.41b) lead to a total power per unit width for the TE polarization

$$\Delta P_m = c_p \Delta y \cdot N\left(P_f + P_c + P_s\right) = c_p \Delta y \cdot \frac{N|A_f|^2}{2}\left(h_f + \frac{1}{|k_{xc}|} + \frac{1}{|k_{xs}|}\right) \tag{3.1.42a}$$

and for the TM modes

$$\Delta P_m = c_p \Delta y \cdot \frac{N|A_f|^2}{2n_{f,x}}\left(h_f + \frac{1}{|k_{xc}|} + \frac{1}{|k_{xs}|}\right) \tag{3.1.42b}$$

The results obtained in this section are the basis for the waveguide part of the analysis software presented in section 4.2.

3.2 Grating coupling: Scalar diffraction approach

The goal of this section is to give some insight into the coupling process of light in and out of a waveguide by means of a grating. For this purpose, the angular distribution of the light propagating away from an output coupler is analyzed. The results are both important for waveguide grating design and analysis of measurement results.

The approach is based on the fact that any field at a given position can be considered to be formed by the superposition of a continuum of plane waves, where the local plane wave spectrum is obtained using the Fourier transform [45]. Supposed that a local field *u(z)* is independent of y and is known at a given position x_0, its plane wave spectrum $\hat{U}(k_z)$ is given by

$$\hat{U}(k_z) = \int u(z)\, e^{-ik_z z} dz \tag{3.2.1}$$

Where the k_z correspond to the z-components of the wavevectors $\boldsymbol{k}$ of the plane waves composing the field. The angular distribution of the of the light extracted from the waveguide is obtained from $\hat{U}(k_z)$ using the relation

$$\sin\theta = \frac{\lambda k_z}{2\pi n_a} \tag{3.2.2}$$

for the part of the spectrum representing propagating waves (k_z real), where λ is the wavelength in air, and n_a is the refractive index of the isotropic medium, in which θ is measured.

The difficulty in this approach lies in the fact that the exact field *u(z)* has to be known at a position x_0 in order to calculate the plane wave spectrum. In our case, an estimation of the form of the field near a waveguide grating output coupler is sufficient for gaining some insight into the working principle of the latter.

Consider a waveguide grating output coupler of finite length *L*, with a guided mode incident from the left. The field at the waveguide grating surface ($x=x_0$) is estimated to have the following main components, illustrated in Figure 3.8:

A) An amplitude and phase modulation due to the grating structure
B) An exponential intensity decay due to the gradual loss of energy through diffraction inside a windowing function describing the finite width L of the grating
C) A linear phase term due to the mode propagation

The three components A, B and C can be associated with three contributions that are multiplied to form the total field, where f_{grat} stands for the modulation due to the grating as described in A, f_{wg} stands for the waveguide and windowing

contribution described in B, and β is the propagation constant of the equivalent waveguide (see section 3.1):

$$u(z) = f_{grat}(z) \cdot f_{wg}(z) \cdot e^{i\beta z} \tag{3.2.3}$$

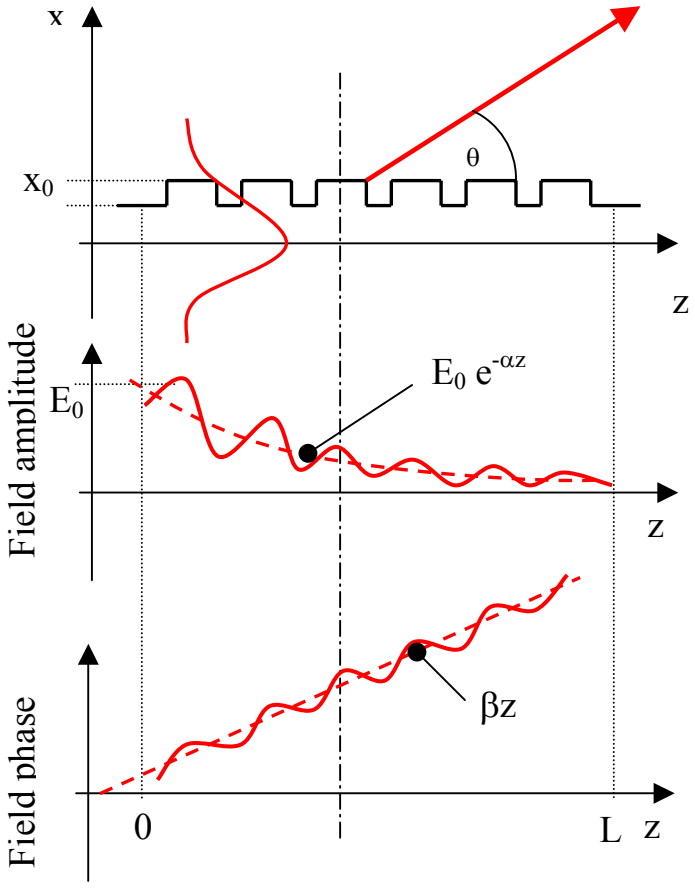

Figure 3.8 Field components at the waveguide grating surface

With the goal of obtaining the plane wave decomposition of this field, and with it the angular spectrum of the light extracted from the waveguide, the Fourier transforms of the three components are studied in the following. The periodic grating modulation can be expressed as a convolution between an infinite Dirac comb and a base function $f_b(z)$

$$f_{grat}(z) = \sum_{l=-\infty}^{\infty} \delta(z - l\Lambda) * f_b(z) \tag{3.2.4}$$

$f_b(z),\ 0 \leq z < \Lambda\ ;$ $\quad f_b(z=0) = lim_{z->\Lambda}\ f_b(z)$

The Fourier transform of the modulation $f_{grat}(z)$ is therefore a Dirac comb of period $2\pi/\Lambda$ multiplied by the Fourier transform of the base function

$$\mathcal{F}(f_{grat}(z)) = \sum_{m_g=-\infty}^{\infty} \delta\left(k_z - m_g \frac{2\pi}{\Lambda}\right) F(f_b) \qquad (3.2.5)$$

where m_g is called the diffraction order. This corresponds to the result obtained for an infinitely long periodic transmission grating illuminated by a plane wave under 0° incidence. In Figure 3.9, the intensity modulation of the spectral Dirac peaks corresponding to different orders is given for the example of a rectangular base function $f_b = rect(z/\Lambda - ½)$. The intensity distribution shown in Figure 3.9 corresponds to the square of the spectrum. As can be seen from eqn (3.2.5) and Figure 3.9, the form of the base function determines the ratios of the amplitudes of the different orders. In the case of the rectangular modulation, the second order is cancelled out. The engineering of the base function by changing the grating profile in order to modify amplitude relations of the orders is called blazing.

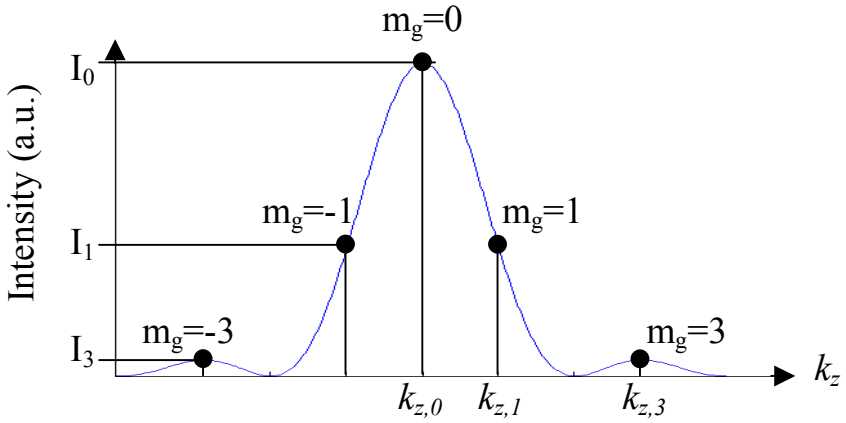

Figure 3.9: Grating order intensities for a rectangular grating. The second order is suppressed.

The waveguide and aperture function (component B) on the other hand determines the shape of the resonance of the individual orders, as will be shown in the following. Its contribution to the field is given by

$$f_{wg}(z) = u_0 e^{-\alpha z} \cdot rect(z/L - ½) \qquad (3.2.6)$$

where α is the leakage factor or parameter. Its amplitude is influenced by the grating geometry such as refractive index contrast and grating depth.
The spectral intensity distribution corresponding to this field is given by a convolution between a Lorentz curve of width $\Delta k_z = 2\alpha$ and a squared sinc of width $\Delta k_z = 2\pi/L$. Depending on the product $\alpha \cdot L$, the exponential decay or the rectangular aperture becomes dominant, as is illustrated in Figure 3.10.
With the goal of obtaining information about the wavelength-spectral peak of the light coupled out at a fixed angle at one grating order, a field $f_{wg} \neq f(\lambda)$ that is

constant with respect to the wavelength can be assumed. The wavelength distribution of the light coupled out can then easily be determined using eqn (3.2.2). For the geometries used for biochemical sensing devices, the approximation is only valid for evaluating the resonance line shape of one order, as the fields can no longer be assumed constant over the larger spectral width that is needed for an evaluation of several orders.

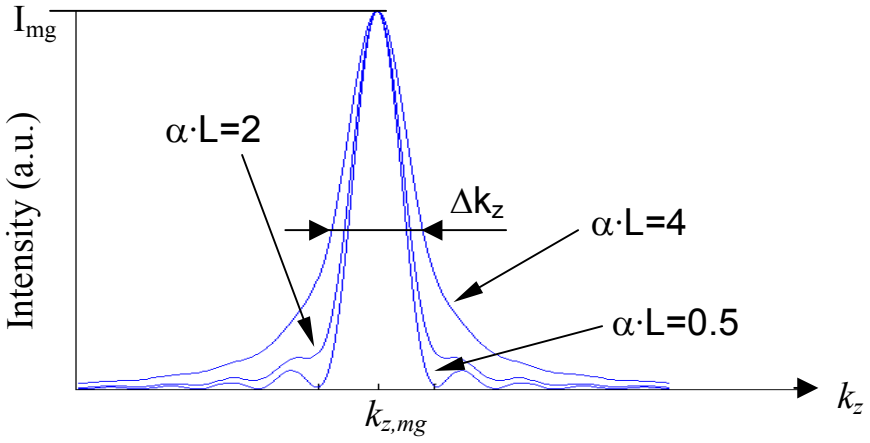

Figure 3.10: Outcoupling line shapes in k-space for different values of the product $\alpha \cdot L$.

The last contribution (C) is characterized by the waveguide mode propagation. Due to the translation theorem, this phase term results in a simple shift by the propagation constant β:

$$\mathcal{F}(u(z)\cdot e^{i\beta z}) = \hat{U}(k_z-\beta) \tag{3.2.7}$$

The complete response of the system is therefore given by:

$$\hat{U}(k_z-\beta) = \mathcal{F}(f_{wg}(z)) * \mathcal{F}(f_{grat}(z)) \tag{3.2.8}$$

Under the condition of distinct frequency scales of the contributions ($L>1/\alpha>>\Lambda$), the peaks are well separated. Their position is given by the periodicity and the propagation constant of the waveguide. Their shape is given by the decay and windowing functions.

Given a feature base function f_b having a Fourier transform which is maximum around a frequency of 0, the conditions for maximum coupling for a given grating order m_g is given for eqn (3.2.8) by

$$k_z-\beta = m_g 2\pi/\Lambda \tag{3.2.9}$$

Expressing (3.2.9) in terms of effective refractive indices and angles using eqn (3.2.2) reveals the well-known waveguide grating resonance condition

$$n_a \cdot \sin\theta = N - m_g \lambda_r / \Lambda \qquad (3.2.10)$$

In summary, the approximate angular (and some wavelength) dependency of the light intensity extracted from a waveguide grating output coupler has been derived by estimating the field at its surface and using a scalar diffraction appraoch. In the case of an input coupler, however, the same treatment is not possible for evaluating the dependence of the intensity of the excited mode on the spectrum of the light incident on the device. This is because the field near the waveguide grating is not known a priori, and even strongly dependent on the spectrum of the incident light. Nevertheless, by using reciprocity and overlap integrals, the results obtained for a waveguide grating in the output coupler configuration can be used to calculate the response of the same device in the input configuration [46]. For the waveguide gratings used in biochemical sensing, it can be stated that the behavior of the input coupling device is very similar to the case of the output coupler as treated above. Experimental evidence is given in section 5.4, where measurement data for two input coupling configurations of different leakage factor are compared to the Fourier transform method. In the geometries used here, the above approximate statements about resonance peak width, shape and position of an output coupler are also valid for input couplers.

It can be concluded from the statements made in this section, that the available design parameters for a periodic grating coupler are quite limited. In practice, the grating length, periodicity and depth can be adapted to meet the design requirements. An approach using non-periodic grating couplers for overcoming these limitations was presented in [47].

Figure 3.10 is important for waveguide grating sensor applications, as it shows signal shapes that are actually observed when scanning the resonance of a given order. For achieving a high resolution and measurement range, it is advantageous to have narrow peak widths. This is the reason why in our case, gratings having a relatively low leakage parameter ($\alpha < 1/L$) and a length L in the order of 1mm have been chosen. It is important to note however, that the resolution of the waveguide grating sensor is not limited to the halfwidth of the peak. This would be the case if two different laser wavelengths had to be distinguished. In our case, the change of the waveguide's effective refractive index N results in a shift of the resonance peak, which can be detected with much higher resolution. Again, the shift in resonance wavelength, as observed in the wavelength interrogated optical sensor (WIOS), is related to the change in effective refractive index by eqn (3.2.10).

3.3 Substrate reflections

For accurate peak position detection, a resonance line shape that is constant over the measurement range is a prerequisite. It has been observed [27] that parasitic interference modulations, originating from reflections at the substrate interfaces, can significantly disturb the results. For estimating the possibilities for calibration and optimized chip designs, a suitable theoretical treatment has to be established.

Figure 3.11 shows the situation at the input and output pads of a typical sensor chip. At the input coupler (sensing pad), one fraction of the incident laser beam is coupled into the waveguide with a phase φ_1, another is reflected at the substrate-grating interface, and a third fraction (not illustrated) is transmitted. The reflected wave, upon arrival at the substrate-air interface, can either be transmitted (not illustrated), or be reflected. The part that is hereby twice reflected and then coupled into the waveguide with phase φ_2 contributes to the modulation, as it picks up a phase shift $\Delta\varphi = \varphi_2 - \varphi_1$ when traveling through the substrate. A similar reasoning can be done for the output coupler. As the phase shifts $\Delta\varphi$ of both interference contributions are not constant for different wavelengths and angles, a clearly visible modulation is superposed to the resonance line signal in both angular and wavelength readout schemes.

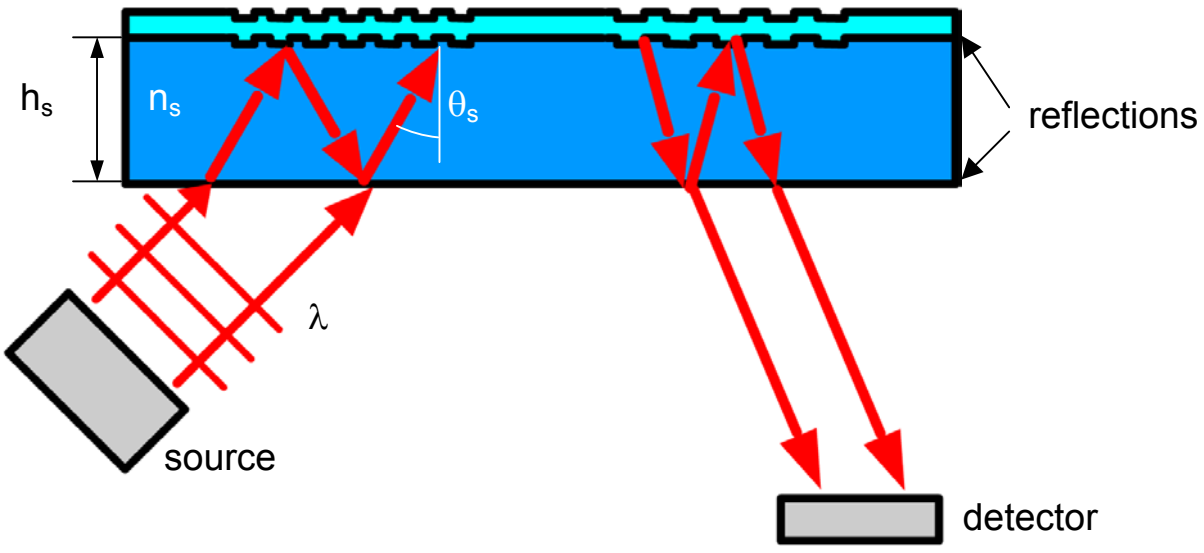

Figure 3.11: Origin of the parasitic interference modulation

Let us take a look at the situation of the incoupler being illuminated by a plane wave of wavelength λ as illustrated in Fig. 3.11. The phase shift $\Delta\varphi = \varphi 2 - \varphi 1$ is calculated by comparing the doubly reflected wave with the one incident at the same spot, having traveled a longer distance in the air.

$$\Delta\phi = \frac{4\pi h_s n_s}{\lambda}\left(\frac{1}{\cos\theta_s} - \sin^2(\theta_s)\right) + \varphi_{sf} + \varphi_{sa} \tag{3.3.1}$$

where n_s is the index of refraction of the substrate, φ_{sf} is the Fresnel phase shift at the substrate film boundary, and φ_{sa} is the Fresnel phase shift at the substrate-air boundary.
The amplitude a_2 of the reflected wave is related to the amplitude a_1 of the original wave as

$$a_2 = a_1\, r_{sf}\, r_{sa}$$

where r_{sf} the amplitude of the reflection coefficient at the substrate-film boundary, r_{sa} the amplitude of the reflection coefficient at the substrate-air boundary. The intensity modulation I_{mod} of the signal corresponds to the interference term of the two waves.

The impact on the signal peak shape is evaluated by expressing the modulation in terms of wavelength for a wavelength sensing scheme:

$$\frac{I_{\mathrm{mod}}}{I_1} = 2\frac{a_1 a_2}{a_1^{\,2}}\cos(\Delta\phi) = 2r_{sf}\, r_{sa}\cdot\cos\left(\frac{\partial\Delta\phi}{\partial\lambda}\cdot\Delta\lambda\right) \tag{3.3.2}$$

where

$$\frac{\partial\Delta\phi}{\partial\lambda} = -\frac{4\pi h_s n_s}{\lambda^2}\left(\frac{1}{\cos\theta_s} - \sin^2(\vartheta_s)\right) + \frac{\partial\varphi_{sf}}{\partial\lambda} + \frac{\partial\varphi_{sa}}{\partial\lambda} \tag{3.3.3}$$

is the modulation frequency. A similar development leads to the same result for the output coupler grating pad, with different angles due to the different grating period. The total deformation of the coupling line shape due to the reflection modulation is given by the superposition of the two modulations:

$$a_{dist}(\lambda) = [1 + r_{s,in} + 2\cdot r_{s,in}\cdot\cos(\Delta\phi)] \cdot [1 + r_{s,out} + 2\cdot r_{s,out}\cdot\cos(\Delta\phi + \phi_0)] \tag{3.3.4}$$

Figure 3.12 compares the simulation of an undisturbed peak to the case of a peak that is modulated due to the parasitic reflections. The impact on the peak position detection is presented in section 5.6.

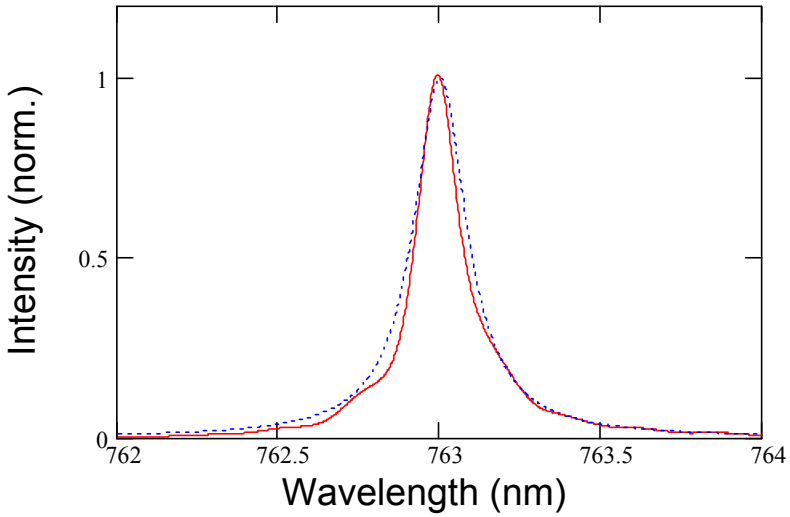

Figure 3.12: comparison of undisturbed peak (dashed) and peak that is modulated due to parasitic substrate reflections (solid)

The calculated interference amplitude corresponds to the maximum value that can be obtained in an experiment. Effects such as reduced beam overlap due to the geometry, reduced planarity of the interfaces, an angular spread or reduced coherence of the beams all contribute to an attenuation of the modulation amplitude. The reduced beam overlap will be presented in section 6.1 for designing optimized chips.

Chapter 4

Numerical modeling

As mentioned in section 3.1, the analytical equations describing the waveguide mode structure (3.1.20) and the grating resonance condition (3.2.12) are sufficient approximations for a large number of practical engineering tasks. This is the case for design tasks such as optimization of sensor sensitivity, where the effects due to the peak shape can be neglected. The practical and robust implementation of a waveguide grating sensor model based on these equations was part of this thesis. Details about the modeling of biochemical adlayers are given in section 4.1, while the implementation of the model into a dedicated software tool is presented in section 4.1.

For other tasks such as definition of tolerances and design of robust sensor platforms, the resonance line shapes of the structures have to be estimated. The typical structures used for biochemical sensors consist of monomode slab waveguides with surface relief gratings of small depth (10-20nm) but with large refractive index differences, grating periods in the order of the wavelength, and a grating length in the order of the millimeter. These characteristics make them difficult to model with many (approximate) methods used in integrated optics: The refractive index differences are too large for classical perturbation theory [48], and too many features are present for FDTD [49] or modal [50] approaches.

The output coupler is well approximated by scalar diffraction theory as for instance the Fourier transform method (see section 3.2). By reciprocity of the coupling process, the input coupler configuration can be evaluated based on the results for the equivalent output coupler. This calculation is done by means of overlap integrals [46]. The method is best suited for configurations where the integration can be performed analytically, i.e. uniform waveguides, or waveguides presenting simple types of non-uniformities that vary slowly with respect to the grating period. Another method for evaluating waveguide grating inhomogeneities applied to biochemical sensors is presented in [12], where the authors treat the problem with a less elegant zigzag ray approach.

The effect of non-uniformities, as for instance non-periodic gratings, thickness or refractive index changes, or particle deposition, is an important aspect in sensor applications, where the high Q-factor of the resonant structure needed for a high resolution is easily disturbed. An example has been described in [29], where extremely small waveguide thickness variations significantly affected sensor performance.

In order to have a simple and efficient tool for calculating these non-uniformity phenomena, the local interference method (LIME) has been developed in the framework of this thesis, and is described in section 4.3. It is a simple recursive algorithm, whose calculation complexity is comparable to the Fourier transform method. The LIME includes the treatment of the input or output coupler in one calculation step. A major advantage of the method lies in the fact that the essential parameters, which may vary along the structure -such as film thickness and grating periodicity - are explicitly appearing in the formulation. It provides a simple and versatile tool for rapidly evaluating non-trivial waveguide grating structures.

4.1 Adlayer growth

An important question for the modeling of sensor performance is how the biochemical adlayer, composed of recognition and target molecules, is modeled. The biochemical binding processes to be detected are in general very complex, and a complete description of the optical changes occurring at the sensor interface cannot be given. The simple model that is generally adopted describes changes of an equivalent adlayer, which is called sensing layer, as illustrated in Figure 4.1. This layer is characterized by its thickness (h_l, usually several nanometers) and its refractive index (n_l, around 1.45 for the example of a protein layer). Molecular deposition is modeled as a change in thickness ("growth") or refractive index ("density") of this layer.

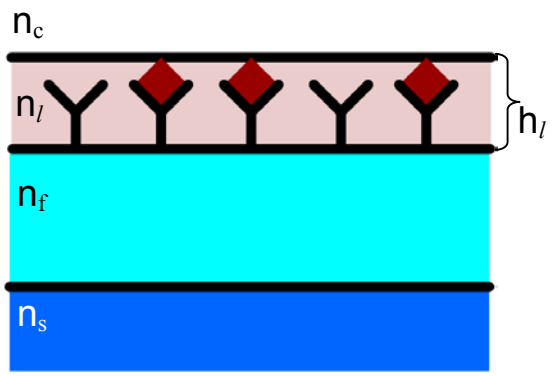

Figure 4.1: Biochemical layer modeling by an equivalent layer of thickness h_l and refractive index n_l.

In a simple model, the molecular interactions correspond directly to changes in refractive index n_l or thickness h_l of the adlyer. The change in thickness is the most commonly used model and the result correspond well to the experimental data [27][30]. Using this model, the quantity to be measured is the change of the effective index N upon changes of the layer thickness h_l, while the actual parameter of interest for the measurement is usually a change in surface mass coverage $\Delta\Gamma$ of molecules deposited on the waveguide surface. The surface mass coverage $\Delta\Gamma$, expressed in pg/mm^2, is related to the measured effective refractive index difference ΔN by

$$\Delta\Gamma = \frac{\Gamma_1}{h_1}\cdot\left(\frac{\partial N}{\partial h_l}\right)^{-1}\cdot\Delta N = \frac{\Gamma_1}{h_1}\cdot(S_h)^{-1}\cdot\Delta N \qquad (4.1.1)$$

where Γ_1 is the surface mass coverage of a saturated layer, h_1 its thickness, and S_h denotes the waveguide sensitivity to adlayer thickness changes. For the case where the molecule deposition is modeled as a simple refractive index change, the corresponding surface mass coverage change is given by

$$\Delta\Gamma = \frac{\Gamma_1}{n_1}\cdot\left(\frac{\partial N}{\partial n_1}\right)^{-1}\cdot\Delta N = \frac{\Gamma_1}{n_1}\cdot(S_n)^{-1}\cdot\Delta N \tag{4.1.2}$$

where S_n denotes the waveguide sensitivity to adlayer refractive index changes, and n_1 is the thickness of the saturated adlayer. However, this model is rarely used, because it does not correspond well to the experiment. The reason for this is that often, low molecule concentrations are measured, resulting in unsaturated molecular adlayers. In this case, the refractive index of the layer is also function of the cover refractive index n_c.

In [42] it has been shown that a good approximation of the optical properties of such an unsaturated layer is obtained by an effective medium approach. The equivalent biochemical layer is modeled as having a fixed thickness corresponding for instance to a molecular monolayer, as is illustrated in Figure 4.1. The refractive index of this monolayer depends on the density of the molecules inside the layer. In consequence, the molecular deposition is modeled as increase of the fraction occupied by equivalent particles.

Assuming the particles to have the shape of rectangular plates, two cases have to be considered [51]. Depending on the manner of averaging the dielectric functions of the two lossless materials forming the intermediate layer, two different layer indices $\bar{n}$ and $\underline{n}$ are obtained according to the expressions

$$\bar{n}(f_p, n_p, n_c) = \sqrt{f_p\cdot n_p^{\,2} + (1-f_p)n_c^{\,2}} \tag{4.1.3}$$

and

$$\underline{n}(f_p, n_p, n_c) = \sqrt{\left(f_p\cdot n_p^{\,-2} + (1-f_p)n_c^{\,-2}\right)^{-1}}\,. \tag{4.1.4}$$

where f_p is called the particle fraction and n_p is the refractive index of the particles. Equations (4.1.3) and (4.1.4) correspond to [51], p. 707, Equations (17) and (14), respectively.

An average value

$$n_l = \bar{n} + c_n\cdot(\underline{n} - \bar{n}) \tag{4.1.5}$$

of the intermediate layer refractive index is obtained by interpolating between the indices $\bar{n}$ and $\underline{n}$ given by (4.1.3) and (4.1.4). As has been shown in [42], a value of about c_n=0.5 delivers good results for the modeling of a molecular

monolayer. Expressing the change in surface mass coverage $\Delta\Gamma$ in terms of particle fraction changes leads to

$$\Delta\Gamma = \Gamma_1 \cdot \left(\frac{\partial N}{\partial f_p} \right)^{-1} \cdot \Delta N = \Gamma_1 \cdot \left(S_f \right)^{-1} \cdot \Delta N \qquad (4.1.6)$$

where Γ_1 is the surface mass of a layer with f_p=1, and S_f is the sensitivity of the waveguide to particle fraction changes.

The sensitivities S_f, S_n and S_h, which are called primary or waveguide sensitivities, depend on the waveguide configuration, and on the data for the molecule layer to be detected. In [30], the following data is given for a saturated immunoglobulin G (IgG) monolayer: refractive index n_p=n_1=1.46 (λ=633 nm), thickness: h_1=8.5 nm, surface mass Γ_1=5 ng/mm^2.

For sensor design, the primary sensitivities should be maximized. However, as is shown in section 5.1, a careful analysis of the whole system is needed for optimal performance. This includes the analysis of the grating properties and parasitic effects such as cover refractive index changes.
For calculating all these aspects of the waveguide grating sensor, a dedicated software was written in the framework of this thesis, presented in the next section.

4.2 Waveguide grating analysis software

For sensor design and measurement analysis tasks, a dedicated software tool was written in the framework of this thesis. The "waveguide grating analyzer" (wagralizer), is designed to exploit the full potential of the analytical expressions (3.1.20) and (3.2.10) describing the waveguide and the grating, respectively. Figure 4.2 shows a screenshot of the main application window.
The program presents the following features:

- Robust mode search algorithm for the treatment of multilayer systems composed of layers that are isotropic, birefringent or have averaged indices of refraction
- Solver for one waveguide or grating parameter, e.g. determination of the resonance wavelength knowing all other relevant parameters of the system
- Multi-variable optimization for the determination of several parameters based on a set of measurements, for instance the calculation of both film thickness and refractive index based on the resonance angles of two distinct modes
- Freely configurable 2D and 3D Plots of all relevant dependencies, such as the dependence of the resonance wavelength on incidence angle and grating period
- Freely configurable 2D and 3D Plots of all relevant derivatives and sensitivities, for instance waveguide sensitivity versus film thickness and refractive index
- Visualization of the normalized mode intensities

The goal was to write a stand-alone application, therefore the program was written using the Delphi® integrated development environment, which uses an object-oriented version of the Pascal programming language. The reason for this choice was primarily the short development times achieved using this package, which is traded against slightly slower calculation with respect to the C++ programming language.
The program was structured in a modular way, which is facilitated by the object-oriented language, in order to allow the integration and test of different calculation modules, and for reuse of the components in other applications. As an example, the multi-variable optimization modules have been re-used in the chip characterization instrument which is presented in section 6.2. While the implementation details on the programming level will not be mentioned in this thesis, the calculation schemes and algorithms that have been used for the most important features are given in the following paragraphs.

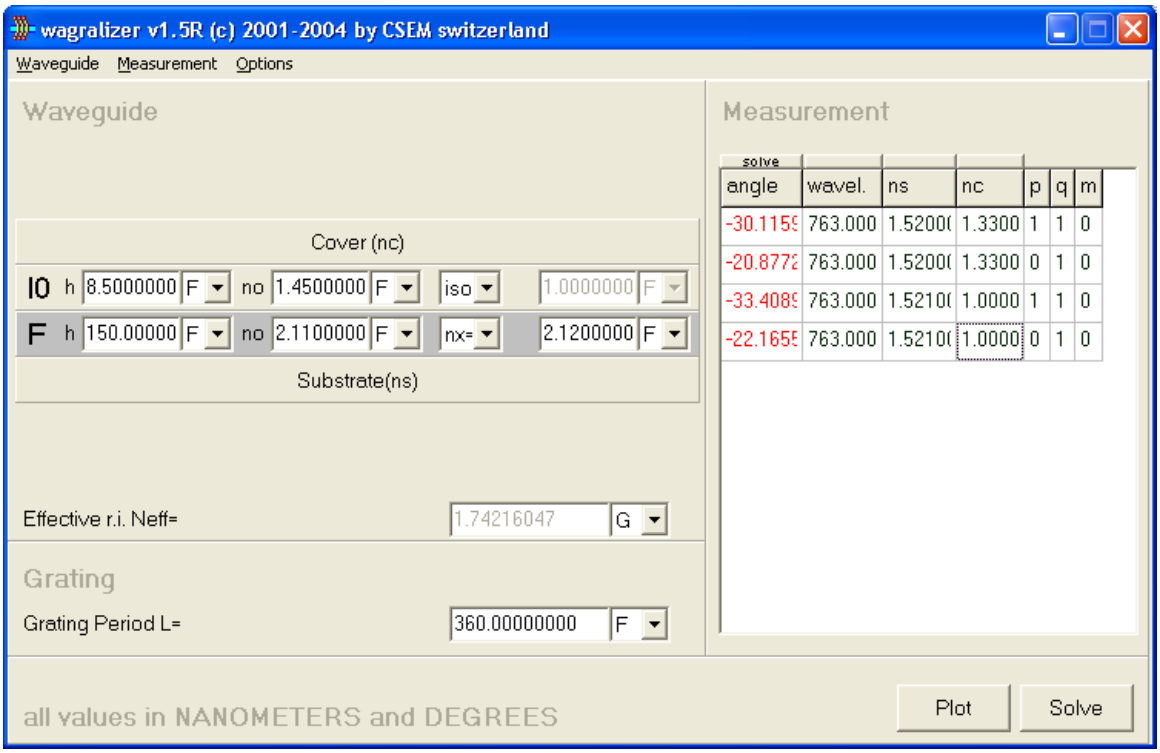

Figure 4.2: Screenshot of the "wagralizer" main application window

4.2.1 Waveguide-grating structure definition

In wagralizer, a maximum of 6 layers (the number is only limited by the display) may be inserted between the substrate and cover medium for constructing the waveguide. While the substrate and cover are always assumed to have an isotropic refractive index, the intermediate layers may exhibit birefringence, with the main refractive index axes parallel to the main axis of the structure as illustrated in Figure 3.3. Alternatively, the topmost layer can be modeled as being composed of particles, having an averaged and isotropic index of refraction. The calculation of the index of refraction is based on the particle refractive index n_p, the cover index of refraction and the particle fraction f_p. The averaged refractive index is calculated by eqn (4.1.5) using an averaging value of c_p=0.5.

The definition of waveguide structure is depicted in the left part of Figure 4.2, where the configuration of the waveguide composed of a birefringent film and an isotropic adlayer is shown. The refractive indices of the substrate and cover are entered in the table on the right hand side, where also the angle of incidence, wavelength, polarization, diffraction order and mode number are entered. In the example, the resonance angles for light at a wavelength of 763nm have been calculated for both polarizations, and in water (n_c=1.33) and air (n_c=1).

4.2.2 Mode search algorithm

The task of this algorithm consists in finding all solutions of eqn (3.1.20) and the corresponding effective refractive indices N for a given waveguide structure. This is done by evaluating the system for a number of start values N_l, l=1..M, where the values of the N_l are chosen such as $\max(n_l) \geq N_l \geq \max(n_s, n_c)$, where n_l denotes all refractive indices of the layers between substrate and cover, including the film.
By noting $f(N)$ the imaginary part of eqn (3.1.20), the modes are bracketed by the condition illustrated by the following pseudo-code

For l=1..M-1 do
    If ($f(N_l) \cdot f(N_{l+1}) < 0$) and ($f(N_l) < 0$) then
        Mode between $f(N_l) \cdot$ and $f(N_{l+1})$

Which is nothing else than finding negative-to-positive zero crossings. The modes being located at the zero crossing, a zero finding is then executed between every pair N_l, N_{l+1} that has been found with the statement above. An implementation of the secant method [52] is used for finally finding the actual effective refractive indices corresponding to the modes.
If an insufficient number of start values M is used, some modes can be missed. For most configurations used in this thesis, M=20 has been proved to be sufficient.

4.2.3 Solver

Depending on the nature of the parameter to be calculated, different approaches are taken. If the researched value is either the grating period Λ or the resonance angle θ, the effective refractive index of the mode is searched as explained in section 4.2.2, and inserted directly into the grating resonance condition (3.2.10). For calculating all other parameters, a method similar to the mode search is used. In this case, the complete mode search algorithm has to be executed several times in order to prevent convergence on a wrong mode.

4.2.4 Multi-variable parameter optimization

If a set of measurement data is to be used to find the corresponding structure parameters, a multivariable optimization is needed. A good example of practical relevance is the determination of waveguide film thickness and refractive index based on the resonance angles for a TE and TM mode knowing all other parameters. The Levenberg-Marquardt method [52] was therefore implemented into wagralizer.

4.2.5 Plotting features

Figure 4.3 shows a screenshot of the wagralizer plot widow. In this example, the resonance angle is traced against film thickness for the waveguide-grating configuration and for all four conditions visible in Figure 4.2. The open drop-down list on the right-hand side in the figure illustrates how the interface is designed to allow the comfortable selection of the parameters to be plotted. As special features, the plots may be in three dimensions, and the possibility is given to evaluate all relevant derivatives, for instance the sensitivity of the resonance wavelength to layer thickness changes $\partial\lambda_r/\partial h_l$. For maximum flexibility, the derivatives are calculated numerically. In the example cited before, two resonance wavelengths $\lambda_1(h_l)$ and $\lambda_2(h_l+\Delta h)$ are calculated, and the numerical derivative is given by

$$\partial\lambda_r/\partial h_l \approx (\lambda_2-\lambda_1)/\ \Delta h$$

where h_l is the actual layer thickness and Δh is a small thickness variation.

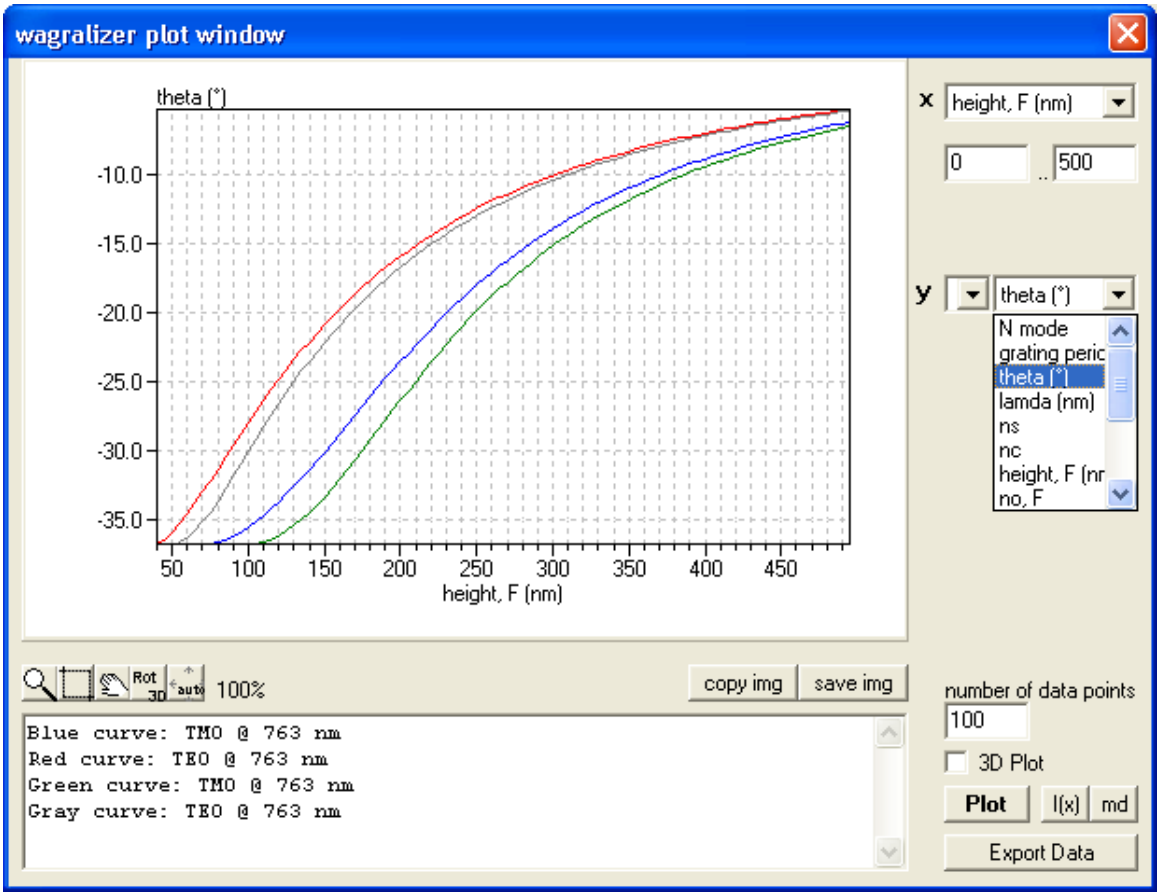

Figure 4.3: Screenshot of the wagralizer plot window

4.2.6 Application of wagralizer

The program proved very useful for gaining insight in the behavior of waveguide-grating sensors. Based on “simple” analytical expressions, it has led to interesting results partly illustrated in Chapter 5 and partly submitted for publication [53]. Furthermore, it has been used intensively and with success in several projects involving industrial partners.

4.3 Local Interference Method (LIME)

In the LIME approach, the grating lines are modeled as scatterers of infinitesimal extent. In the present formulation, the algorithm applies to monomode waveguides showing weak perturbations. An approach that is similar to the presented method has been published in [47] as a technique for calculating non-periodic gratings. There, the difficult task of calculating the scattering properties of the individual grating lines has been fulfilled using the multiple multipole technique (MMP). However, as is mentioned in section 4.3.2, using a matrix-based algorithm for calculating the cumulative effect of the individual scatterers limited its application to several dozen grating lines.
In summary, the LIME approach reduces the description of waveguide grating couplers to the interaction and propagation of the following waves:

- The forwards and backwards propagating modes
- An incident wave (and its transmission and reflection)
- A diffracted wave

Using the LIME scheme, the coupling process is therefore modeled in two steps: The first step, illustrated by Figure 4.4(a), consists in the power exchange between radiative and guided modes at each grating line due to scattering. The "local interference" takes place between the incident light and the light already present in the waveguide. Figure 4.4(a) illustrates this exchange at a single grating line. A guided wave u^f_l incident from the left (forward propagating) and hitting the grating line l is either transmitted into u^f_l', reflected into u^b_l, or scattered into radiative modes w_l. The guided wave incident from the right u^b_l' (backward propagating) is either transmitted into u^b_l, reflected into u^f_l', or scattered into radiative modes w_l. A wave v^i_l propagating outside the waveguide and incident on the grating line l is transmitted into v^t_l, scattered into radiative modes w_l, or scattered into the forward (u^f_l') or backward (u^b_l) traveling guided mode.
The second part, illustrated by Figure 4.4(b), describes propagation between two perturbations. The whole grating length is divided into slices of local width Λ_l being the distance between two adjacent perturbation lines l and $l+1$; $l=1..M-1$, where M is the number of grating lines. The bound modes (u^x) are propagated over this distance according to the local propagation constant β_l. This parameter is given by the local modal structure of the waveguide (see section 3.1). The radiative waves (v^x,w) are propagated according to their local z-component of the wavevector.
Section 4.3.1 establishes the algorithm for the case of a unidirectional mode excitation, where the influence of the backward propagating wave is neglected. The treatment (using slightly different notation) has been published by Cottier et al. in [54], and is valid for a wide range of structures. Section 4.3.2 gives the complete algorithm for bi-directional mode excitation, which is important for

evaluating waveguide gratings with a resonance at normal incidence. Section 4.3.3 shows how to calculate the coupling line shapes of the input and output configuration. Section 4.3.4 gives an overview of the possibilities for determining the important parameters, section 4.3.5 contains a discussion about the relation between LIME and the coupled wave method, and section 4.3.6 compares results of exact calculations of the coupling efficiency of an input coupler to results obtained using LIME.

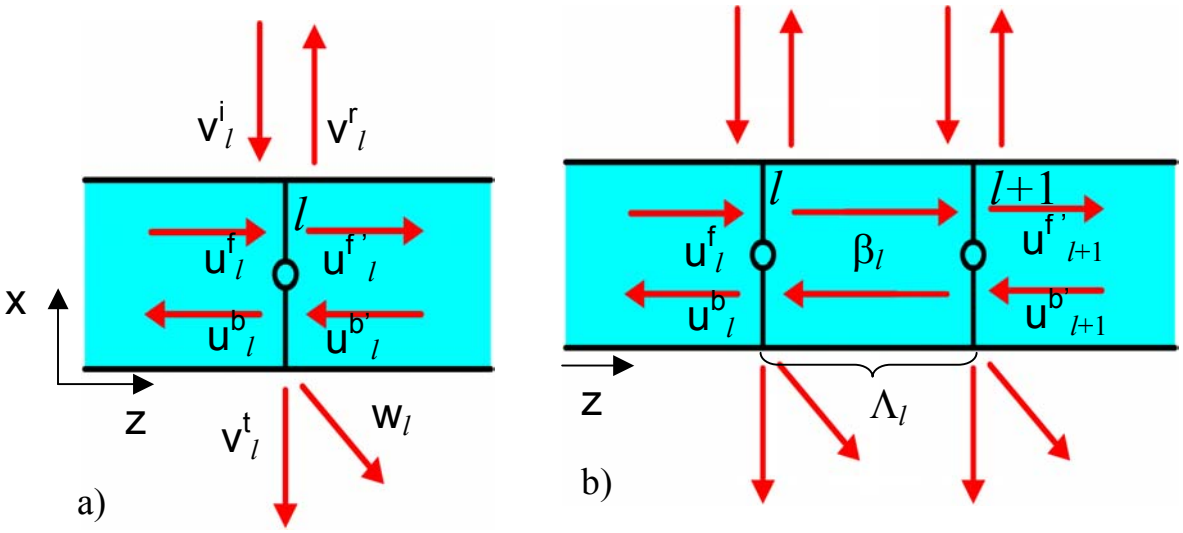

Figure 4.4: Illustration of (a) the power exchange of waves at a grating line, and (b) propagation between two grating lines.

4.3.1 Uni-directional mode excitation

Throughout the structure, the forward-travelling wave is expressed in terms of its electromagnetic field properties, i.e. amplitude and phase. The complex mode amplitude $u_l(z)$, described at a constant vertical position x_0 throughout the structure, corresponds to the electromagnetic field $E_y(z)$ for TE modes and $H_y(z)$ for TM modes. In both cases, the total intensity of the waveguide mode is proportional to the square of the amplitude of the wave.
The incident wave v^i_l is described by its amplitude $a(z)$ and phase $\varphi(z)$ at the same vertical position x_0 as above. For the case of a plane wave excitation, the amplitude is constant over the whole grating length, and the phase is proportional to the z-position, and the z-component k_z of the wave vector $\boldsymbol{k}$.
Using these definitions, the incident light v^i_l hits the l^{th} grating line at position z_l with a given amplitude a_{il} and phase φ_{il}. Due to the scattering process at the grating line, a partial wave u^v_l is excited in the guide. Its amplitude is related to the amplitude of the incident wave by the local line input coupling factor γ_l:

$$u_l^v = \gamma_l(\theta,\lambda)\cdot a_{il}e^{i\varphi_{il}} \tag{4.3.1}$$

At the same time, the perturbation causes an energy transfer from the field u_l present in the guided mode towards radiative modes, leading to a modified mode amplitude. After interference of the partial excited wave u^v_l with the remaining wave present in the waveguide, the resulting wave is given by

$$u_l^f{}' = \tau_l(\lambda)\cdot u_l^f + u_l^v, \tag{4.3.2}$$

where τ_l is the mode transmission factor of the given line.
The two complex coupling factors γ_l and τ_l depend on the grating line characteristics (geometry, refractive indices), the wavelength and the incidence angle. The different methods of calculating these factors will be given in section 4.3.4.

Finally, at the next grating line, the complex field amplitude is given after propagation with constant β_l over a distance Λ_l:

$$u_{l+1}^f = \tau_l(\lambda)\cdot e^{i\beta_l\Lambda_l}\cdot u_l^f + \gamma_l(\theta,\lambda)\cdot e^{i\beta_l\Lambda_l}\cdot v_l^i \tag{4.3.3}$$

l=1..M-1

4.3.2 Bi-directional mode excitation

Gratings with a resonance near normal incidence show an excitation of both forward and backward propagating modes. In order to model this type of structures, bi-directional mode propagation and line reflection effects are included. In [47], a matrix formalism is given for this specific task. There, the calculation time limited the application to a few dozen grating lines. It was found that calculating the counter-propagating modes separately is considerably more efficient without generating convergence problems.
Accounting for the presence of the backward traveling mode u^b, its reflection at grating line *l* is added to the forward propagating mode of eqn (4.3.3)

$$u_{l+1}^f = \tau_l(\lambda)\cdot e^{i\beta_l\Lambda_l}\cdot u_l^f + \gamma_l(\theta,\lambda)\cdot e^{i\beta_l\Lambda_l}\cdot v_l^i + \rho_l(\lambda)\cdot e^{i2\beta_l\Lambda_l}\cdot u_{l+1}^b \tag{4.3.4a}$$

l=1..M-1

$$u_l^b = \tau_l(\lambda)\cdot e^{i\beta_l\Lambda_l}\cdot u_{l+1}^b + \gamma_l(-\theta,\lambda)\cdot e^{i\beta_l\Lambda_l}\cdot v_l^i + \rho_l(\lambda)\cdot u_l^f \tag{4.3.4b}$$

l=M-1..1

where ρ_l is the line reflection coefficient, whose determination is explained in section 4.3.4.

The recursions (4.3.4a) and (4.3.4b) are executed several times until convergence is reached. For reasonable gratings for use with biochemical sensors (α in the order of $1/L$) with at least several dozen lines, convergence is achieved in less than 5 algorithm repetitions, as the line reflection coefficients are in this case relatively small.

4.3.3 Coupling line shape calculation

The original target application for the LIME algorithm is the evaluation of the coupling line shape of a single grating order of a grating presenting small non-uniformities [54]. The limitation to a small range of angles and wavelengths allows the assumption of constant line parameters, which can be determined experimentally or by approximate methods (see section 4.3.5) in the case of a grating with a resonance significantly far from normal incidence. Furthermore, the line coupling parameter γ appears only as a scaling factor for the case of a pure input coupler (with initial mode $u^f_l=0$).
The calculation of the coupling line shape for the input coupling configuration is straightforward by evaluating eqs (4.3.3) or (4.3.4) for a range of angles or wavelengths and by setting $u^f_l=0$.
The output configuration with $u^f_l\neq 0$ is calculated by reciprocity. First, eqn (4.3.3) or (4.3.4) is evaluated for a given wavelength by setting the incident wave v^i to zero, resulting in a complex field amplitude distribution u^f_l at every grating line l. In the case of a uniform grating coupler, this distribution corresponds to the decaying exponential shown in Fig. 3.8. The total radiation into a given direction is calculated by summing the radiation from the individual scatterers coherently and in phase using the Huygens principle:

$$v^o(\theta)=\sum_{l=1}^{M}\gamma_l(\theta)\cdot u_l\cdot e^{ik_z(\theta)\cdot(z_l-z_0)} \tag{4.3.5}$$

where k_z is the z-component of the wave vector corresponding to the output wave

$$k_z=|k|\,\sin\theta, \tag{4.3.6}$$

z_0 is an arbitrary reference point, and z_l the z-coordinate of the grating line l.
Eqn (4.3.5) corresponds to the Fourier transform method. Its advantage over calculating the fast Fourier transform lies in the fact that the sampling may be

irregular and that the frequency spacing is not fixed by the sampling. Hence, a smaller frequency range may be evaluated with a better resolution.

4.3.4 Line parameters

There are several ways to determine the line parameters τ, ρ and γ. As mentioned in 4.2.3, the parameter τ is the only one needed for an evaluation of coupling line shapes of gratings with resonances away from normal incidence and presenting only small non-uniformities. It is interesting to note that in this case, τ is related to the grating leakage factor α (c.f section 3.3) as

$$\tau = e^{-\alpha\Lambda}, \tag{4.3.7}$$

with Λ being the mean grating period. Using this relation, the parameter τ can be determined experimentally or using approximate methods [55] [56] for calculating α.
A good way of calculating the line parameters τ and ρ is using mode matching techniques [50]. Those parameters can be determined with moderate effort, they concern only "intra-waveguide" phenomena between bound modes. The power exchange between radiative and bound modes however, which is described by the line coupling parameter γ, is a complex phenomenon and has to be treated by rigorous methods. An example of the calculation of the scattering properties of a single grating line is found in [47]. If the absolute grating efficiency has to be calculated, the exact value of $\gamma(\theta,\lambda)$ is needed.
The spectral dependency of the coupling parameter around a reference value $\gamma(\theta_0,\lambda_0)$, can be approximated using the Fourier transform methods described in section 3.2. Using this method, a rectangular corrugation results in a sinc-shaped spectral dependency of the coupling parameter γ.

4.3.5 Relation to coupled wave method

Equations (4.3.3) and (4.3.4) show a remarkable resemblance to well known coupled wave equations [46]. Looking at the example of the interaction of one free wave *v* with one guided wave *u* as is expressed in (4.3.3), the corresponding coupled wave equation states for the guided wave

$$\frac{du}{dz} = -\alpha(z)u(z) + \kappa(z)v(z) \tag{4.3.8}$$

where α is the leakage parameter and κ the coupling "constant". It can be calculated approximately using a perturbation approach [48] or rigorously by formulating the equations for a suitable set of eigenmodes and solving the

boundary conditions of Maxwell's equations [57]. Of course, the approximate LIME scheme does not intend to compete with any rigorous approach.
The discrete version of eqn (4.3.8) becomes

$$\Delta u = u_{l+1} - u_l = \frac{du}{dz}\Delta z = -\Delta z \alpha_l u_l + \Delta z \kappa_l v_l \tag{4.3.9}$$

leading finally to

$$u_{l+1} = (1 - \Delta z \alpha_l) u_l + \Delta z \kappa_l v_l \tag{4.3.10}$$

which is nothing else than (4.3.3) using different constants. Equation (4.3.10) is the discrete form of the coupled wave equation, and is only valid in this formulation for a step size Δz distinctly smaller than the wavelength. This is because a basic assumption in the coupled wave method is the continuous and distributed interaction between waves. A consequence for grating modeling is that diffraction effects are not included a priori in the formulation. These effects are inserted through spectral dependencies of the coupling constant κ, which necessarily have to be determined prior to using (4.3.8).
The LIME algorithm on the other hand assumes that the interaction takes place only at the grating lines. Due to this choice of discretization, the diffraction effects are directly included in the formulation. This allows using constant line parameter estimates. The author believes that the LIME algorithm is the simplest possible way of describing both waveguiding and diffraction effects of waveguide grating mode excitation at the same calculation step. As can be seen from the next section and the various examples in chapter 5, remarkably good modeling results are obtained with this approximate scheme.

4.3.6 Model validation

For the validation of the LIME scheme, the calculated coupling efficiencies of a waveguide grating using different illumination geometries are compared to exact results. The reference data has been obtained using a dedicated software tool ("Sensor for Windows", written at the General Physics Institute, Moscow, Russia) based on the generalized source method [58]. In comparison with the layouts used for biochemical sensing, a relatively short grating presenting a large refractive index contrast and a deep profile has been chosen, which is a difficult task for any approximate calculation scheme. A configuration in a telecom wavelength band is chosen, for which the calculation of the line transmission τ and reflection ρ parameters is straightforward using the freeware mode-matching software tool "camfr" [59]. The parameters τ and ρ correspond to the amplitude transmission and reflection coefficients of the guided mode through and at the perturbation, respectively; the time required for their

calculation was below one minute on a Pentium 4 running at 1.6GHz. The following parameters have been used for the calculation. The light has a wavelength of 1.55 μm and is TE-polarized. The waveguide is composed of a h_f=240 nm thick GaAs film of refractive index n_f=3.37 on an oxide substrate of refractive index n_s=1.65 and with an air cover (n_c=1). The periodic rectangular grating is etched h_g=35nm deep into the top film interface with a periodicity of Λ=588 nm and a duty cycle of 0.5 over a length of L=100μm. A Gaussian beam is used for illumination, with a waist of radius w_0=50μm, located at the grating. In Figure 4.5, the angular dependency of the absolute coupling efficiency is shown for different positions of the beam center c_b as illustrated in the insets of Figure 4.5.
The line parameters $\tau=0.984e^{-3.0816i}$, $\rho=0.0154e^{-0.6288i}$ and γ=0.07 have the same constant values for all curves calculated using the LIME algorithm (solid lines). While the transmission τ and reflection ρ have been calculated using the above mentioned tool camfr, the incoupling parameter γ has been adjusted to match approximately the reference coupling efficiency corresponding to the beam center position c_b=0.7 L. The absolute coupling efficiency η is defined as the power per unit width carried in the mode ΔP_m (c.f. eqn (3.1.42)) at the end of the grating z=L for a total incident power per unit width ΔP_i=1.
Since in this example, the line transmission coefficient calculated using the mode-matching tool already contains the phase shift of the mode passing from one side of the line perturbation to the other, the propagation term $\Lambda_l \cdot \beta$ in the LIME algorithm must be chosen as the duty cycle times the period times the propagation constant of the unperturbed waveguide $0.5 \cdot \Lambda \cdot \beta$.

Considering that all parameters of the LIME model are assumed constant for all graphs shown in figure 4.5, the correspondence with the exact results is impressive. The performance of the algorithm with respect to diffraction effects is best illustrated by the difference between the resonance peak widths corresponding to the beams at c_b=0.7L and c_b=L. Due to the restricted illumination at c_b=L, the resonance is larger than for the broader illumination at c_b=0.7L. A good illustration showing that the waveguiding effects are well included is the dramatic difference between the results obtained for the beam position at c_b=0 and at c_b=L. in the first case, most of the excited mode energy is gradually coupled out before reaching the end. In the second case, this is not the case.
The position of the coupling peak maxima are slightly shifted for the results obtained with LIME with respect to the exact result. However, this shift is very small considering that the sensitivity of the coupling angle to the grating period $d\theta/d\Lambda$ is approximately 0.26°/nm.

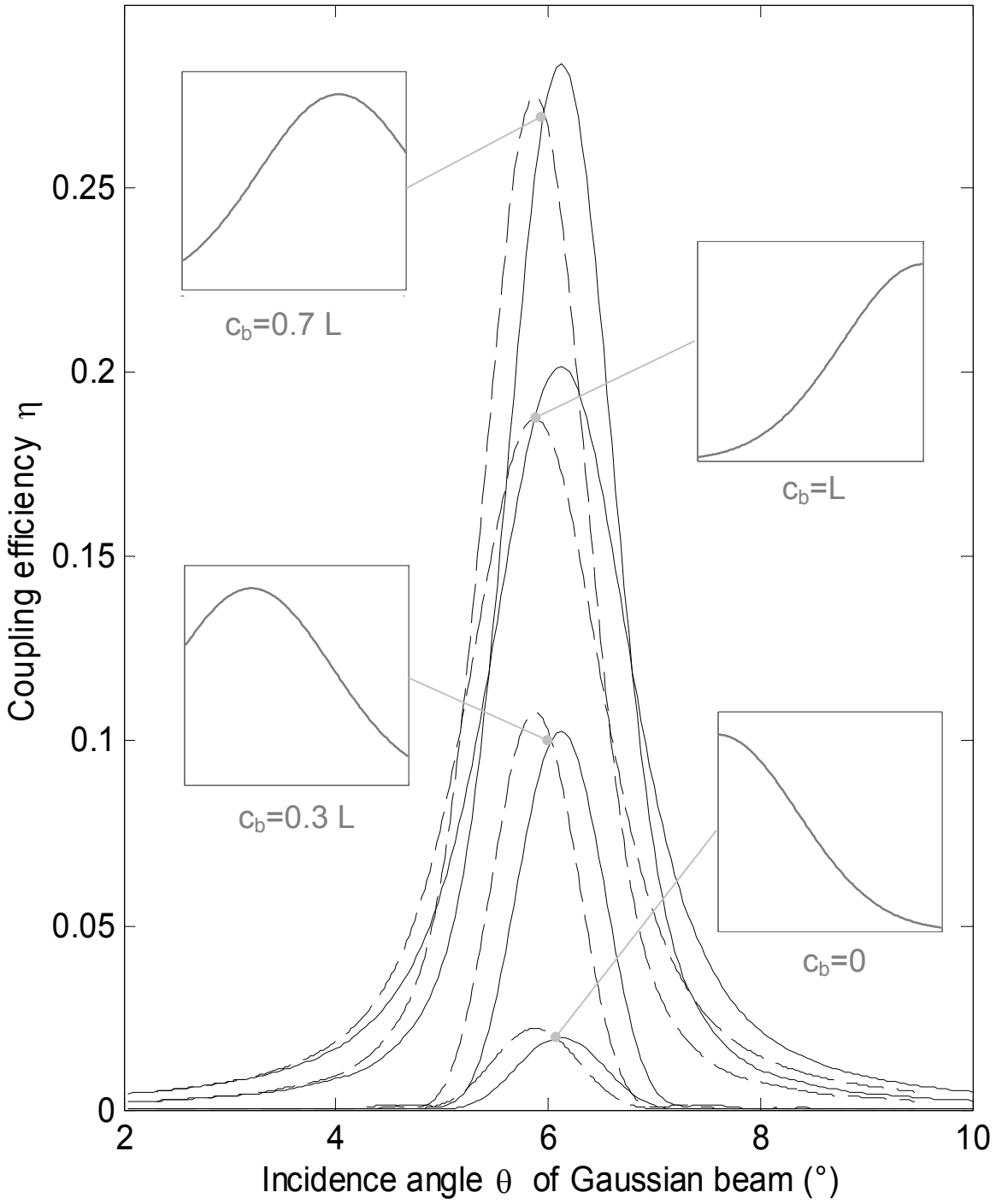

Figure 4.5: Comparison of simulation results obtained using the LIME (solid line) with the exact results (dashed). The amplitude distributions of the beams corresponding to the different peaks are shown in the insets.

Chapter 5

Modeling results

5.1 Sensitivity

The overall waveguide grating sensitivity can be separated into a primary waveguide sensitivity S_w and a secondary grating sensitivity S_g. The primary sensitivity relates the change in effective refractive index N to the optical changes at the sensor interface and has been treated in section 4.1. The secondary sensitivity relates the measurement variable to effective refractive index changes. The overall sensor sensitivity S is given by the multiplication of the primary sensitivity with the secondary sensitivity

$$S = S_w \cdot S_g$$

The two sensitivities are treated separately in the following sections.

5.1.1 Primary sensitivity

Using the particle model of molecule adsorption (see section 4.1), the primary or waveguide sensitivity S_w which is independent of the grating properties, is defined as the sensitivity of the effective refractive index of the waveguide to the volume fraction f_p occupied by the molecules of interest.

$$S_w = S_{fp} = dN/d_{fp}$$

As an example, the primary sensitivity S_{fp} is plotted against film thickness and film refractive index in Fig. 5.1(a) for n_s=1.52, n_c=1.33, λ=763nm, h_l=8.5nm, n_l=1.46. Two main conclusions can be drawn from the graph, namely that the highest sensitivities can be achieved with a high-index film and that different optimal film thicknesses are obtained for different refractive film indices. However, optimizing a sensor to maximum waveguide sensitivity is not sufficient, as will be shown in the next sections.

5.1.2 Sensing layer-to-Bulk volume Signal Ratio (SBSR)

An important aspect in sensor design is the sensitivity to cover refractive index changes. This sensitivity S_{nc} is defined as follows:

$$S_{nc}=dN/dn_c$$

It is a common mistake to assume that S_{nc} has to be maximized for a maximum performance of the biochemical sensor device. In fact, the opposite is true: as the molecule fraction in an adlayer is the parameter of interest and not the cover refractive index, S_{nc} has to be kept as low as possible. A high sensitivity to the cover refractive index translates into a high sensitivity to parasitic effects (drift) due to changes in the buffer solution, such as temperature changes.
Hence, a measure for the quality of a sensor device is the "Sensing layer-to-Bulk volume Signal Ratio" (SBSR) introduced by Kunz and Cottier in [53] and defined as the ratio of the sensitivities

$$SBSR=S_{fp}/S_{nc}$$

In the case of a sensor system, which is limited by background fluctuations and not by its sensitivity, it is more important to design the sensor for higher SBSR than for higher primary sensitivity. Figure 5.1(b) shows the SBSR for the same configuration as in Figure 5.1(a). Comparing the two graphs shows that they have a distinct behavior, leaving room for optimizing a sensor chip for specific needs: for a higher SBSR, suppressing unwanted fluctuations, or for higher sensitivity, resulting in a maximum signal. Moreover, the graph underlines once again the necessity of having a high refractive index film for maximum performance of the sensor.
A thorough treatment of the behavior of the waveguide sensitivity and SBSR for different configurations and different sensing tasks has been performed using the software tool developed in the framework of this thesis (see section 4.2). The results have been submitted for publication [53].

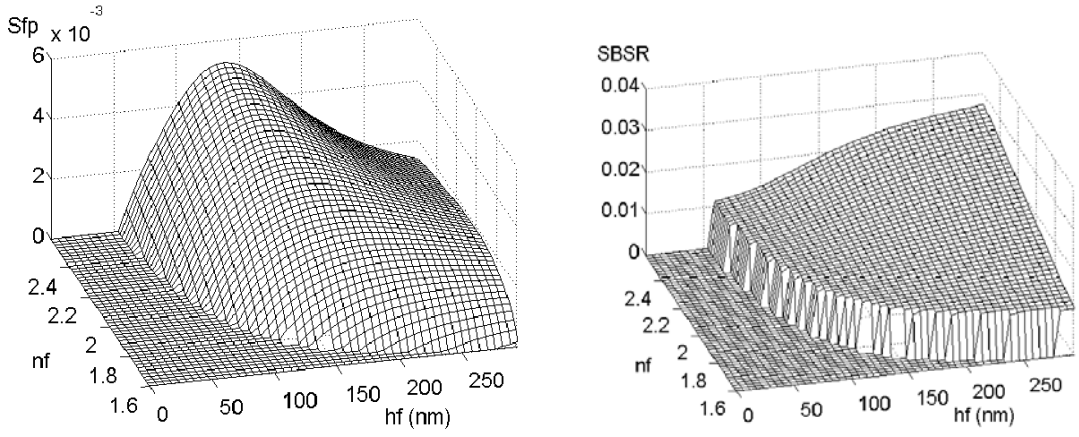

a) b)

Figure 5.1: (a) Primary sensitivity S_{fp} and (b) SBSR for the following waveguide configuration: n_s=1.52, n_c=1.33, λ=763nm, h_l=8.5nm, n_l=1.45, f_p=0.1

5.1.3 Secondary sensitivity

For the case of a wavelength and angular interrogation of the waveguide grating, respectively, the secondary sensitivities take the forms

$$S_{2\lambda} = d\lambda/dN\,, \qquad S_{2\theta} = d\theta/dN$$

Taking the corresponding derivatives of the condition for maximum coupling (3.2.12), the following relations are found:

wavelength readout: $d\lambda/dN \sim \Lambda$

angular readout: $d\theta/dN \sim 1/\cos(\theta)$

For maximum sensitivity, a long period grating should be chosen for the wavelength readout schemes, while for the angular readout, an angle far from normal incidence is preferred.

It should be pointed out that as the secondary sensitivity increases, the resonance peak width also increases, possibly limiting the measurement range. This needs careful examination for a given geometry. As has been discussed in section 3.2, the resolution is less affected by the resonance peak broadening, as the measurement signal corresponds to a peak shift.

5.1.4 Overall sensitivity and mass detection limit

The overall sensitivity of the measurement variable to the optical changes in the adlayer is best calculated numerically as explained in section 4.2. For the case of the particle model and wavelength interrogation, the overall sensitivity is given by $S = d\lambda/df_p$. Knowing this value and the minimum wavelength shift of the resonance peak that can be detected $\Delta\lambda_{lim}$, the mass detection limit $\Delta\Gamma_{lim}$ can be calculated. This value is the minimum change in target molecule mass per area that can be detected with a given sensor. It is calculated as follows

$$\Delta\Gamma_{lim} = \Gamma_1 \cdot \left(\frac{\partial\lambda}{\partial f_p}\right)^{-1} \cdot \Delta\lambda_{lim} = \Gamma_1 \cdot (S)^{-1} \cdot \Delta\lambda_{lim}$$

Where Γ_1 corresponds to the surface mass coverage of a saturated layer (f_p=1).

In table 5.1, Γ_{lim} of two different configurations are compared. The sensitivities are calculated using the same parameters for a biochemical adlayer as described in Figure 5.1. Both layouts are based on the currently used WIOS sensor platforms, with a substrate refractive index of 1.52, a Ta_2O_5 waveguiding film (n_f=2.11) with a water cover (n_c=1.33) at a wavelength of 763nm. Configuration A corresponds to the currently used WIOS sensor platforms, with a film thickness of h_f=150nm, and grating periodicity of 360nm. Configuration B has a film thickness of h_f=180nm, and a grating periodicity of 900nm. The values given in sections 4.1 for the biochemical adlayer and a (measured) wavelength-difference detection limit $\Delta\lambda$ of $7\cdot10^{-5}$ have been used for the calculations.

Config	h_f (nm)	Λ(nm)	$d\lambda/df_p$ (nm)	Γ_{lim} (fg/mm^2)	Rel. SBSR (%)
A	150	360	1.02	340	100
B	180	900	2.06	170	111

Table 5.1 Comparison of mass detection limit and SBSR for two different sensor platforms

As can be seen from the table, a remarkable improvement of the detection limit, as well as a decrease (11%) in sensitivity to cover refractive index drift is obtained. This optimized layout will be further presented in section 6.1.

5.2 Penetration-depth tuning

For every sensor based on evanescent waves, the penetration depth of the latter is related to the geometrical extent of the sensitive region near the waveguide interface. As a rule of thumb, maximum sensitivity can be obtained in the regions where a high fraction of the waveguide mode power is located [42]. An important aspect for sensor design is therefore the size of the substances to be detected and their distance to the waveguide surface.
A major advantage of sensors using planar dielectric waveguides over SPR sensors is the possibility to adjust the penetration depth of the evanescent wave [53]. While for the SPR sensors, this parameter is determined by the material properties, it can be engineered by proper design for dielectric waveguides, by choosing appropriate substrate and film refractive indices and film thicknesses. The penetration depth is independent of the grating properties in a first approximation.

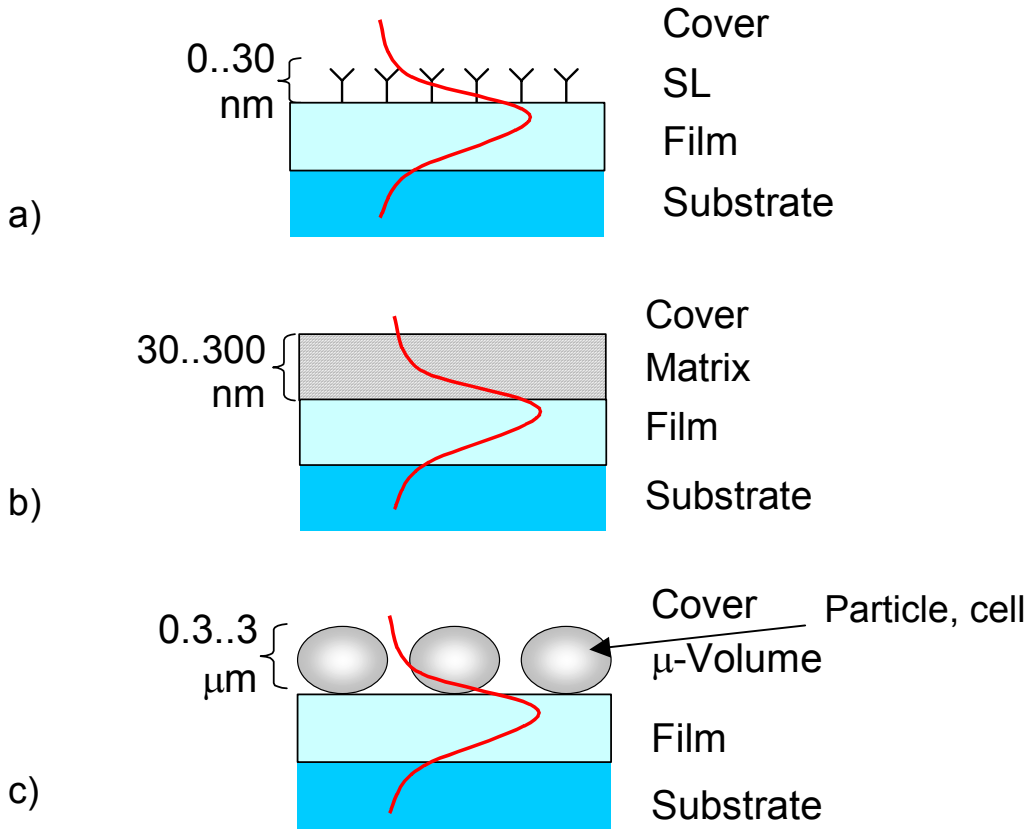

Figure 5.2 different sensor configurations: (a) surface sensing, (b)Matrix sensing and (c) µ-volume sensing

Figure 5.2 shows an overview of some representative sensor configurations. In the surface sensing case seen in Fig. 5.2(a), the (small) molecules are attached

directly to the film. A short penetration depth is preferred in this case, minimizing the effects due to parasitic cover refractive index changes. In the second case (Figure 5.2(b)), the receptors and the target molecules are spread in a sensing matrix of a thickness of typically several hundreds of nanometers [60] [61]. Such a matrix can enhance the number of receptor sites through an enlarged sensing surface, and minimize parasitic interactions with large molecules such as dust particles or even cells in whole blood measurements. In this case, the penetration depth is chosen according to the thickness of the sensing matrix. For the last case seen in Figure 5.2(c), where large objects, for instance cells, are to be detected [22], a large penetration depth is preferred.
The penetration depths can be tuned by a proper choice of film thickness and refractive indices of the substrate and the cover. Figures 5.3(a) and (b) show the mode intensity profiles for two different sensor configurations.

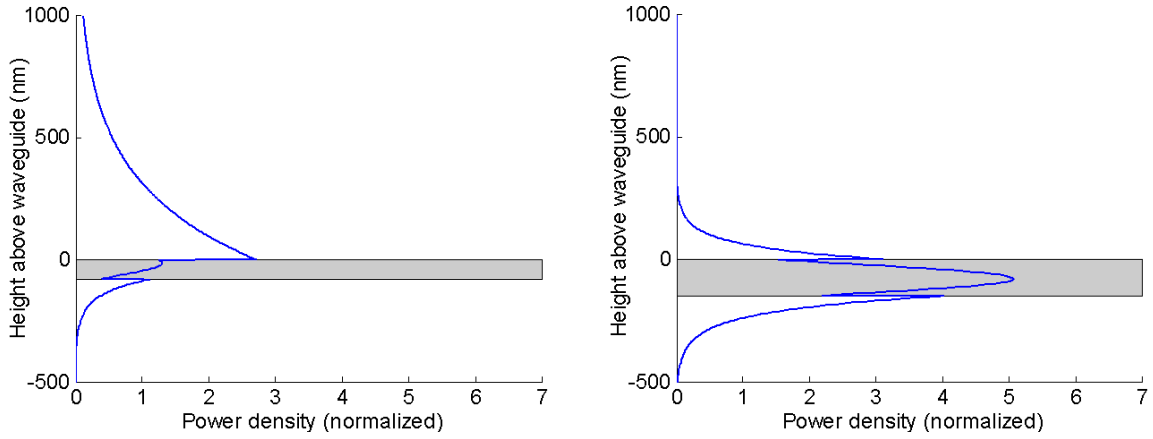

Figure 5.3: Mode intensity profiles for two different configurations: (a) low substrate index of refraction ($n_s<n_c$) and (b) classic configuration

For both configurations, results are given for the TM_0 mode at 633 nm wavelength, with a cover refractive index of n_c=1.389 corresponding to a water cover partially filled (f_p=0.5) with particles of refractive index n_p=1.45.
In the configuration with low substrate index of refraction (Fig. 5.3(a), $n_c>n_s$=1.2, h_f=80nm), the evanescent wave stretches deeply into the cover, while in the classic configuration (Fig. 5.3(b), $n_c<n_s$=1.52, h_f=150nm), it is rapidly decreasing.

5.3 Birefringent layers

The materials used for substrates and waveguides exhibit in some cases a strong birefringence. This is usually considered as parasitic effect. However, the magnitude and orientation of this birefringence can be used as additional degree of freedom, as will be shown in this section. The theoretical background for this section has been established in section 3.1.

First, the example of a strongly birefringent polymer layer is examined, characterized by its refractive indices n_e=1.85 and n_o=1.55. These values have been measured on real polymer waveguide samples. The other calculation parameters have the following values: n_s=1.52, n_c=1.33, λ=633nm, h_f=600nm.

The mode intensity profiles of two waveguide configurations are compared in Figs 5.4(a), (b) and (c). While Fig 5.4(a) shows the situation for the case of an average index of refraction n_f=1.7, Figs 5.4(b) and (c) show the mode profiles for two different orientations of the index ellipsoid of the film. The impact of the orientation on primary sensitivity is shown in Figs 5.4 (e) and (f), compared to the sensitivity of the isotropic material shown in Fig. 5.4(d). The simulations show that the properties of the TE and TM mode differ drastically for the two configurations. This is due to the fact that the TE mode always "sees" the refractive index n_y, while the TM mode "sees" a refractive index between n_x and n_z.

This property can be exploited by setting the effective refractive index of the two orthogonal modes to approximately the same value. In the isotropic case, the two propagation constants are always different. This translates into a significantly different grating resonance condition. However, being able to measure both TE and TM mode at the same time is an advantage, as more information can be deduced from the two measurements. By determining the evolution of the two modes, information about both refractive index and thickness changes of a sensing layer can be determined.

Figure 5.5(a) shows the effective refractive index N versus film thickness for a birefringent film with n_o=1.75, n_e=n_x=1.85. Again, the substrate refractive index was n_s=1.52, the cover refractive index n_c=1.33, and the wavelength λ=633nm. At a film thickness of h_f=145nm, the effective refractive indices of both polarizations are matched. Figure 5.5(b) shows the corresponding mode profile. Despite the closely matched effective refractive indices, a difference in behavior with respect to the refractive index and thickness of the sensing layer is preserved. This is shown in table 5.2, where the sensitivities for both polarizations with respect to adlayer thickness and refractive index changes are listed. With such a system, thickness and refractive index changes of an adlayer could be detected with a low cost sensing device, where TE and TM mode can be excited at similar coupling conditions.

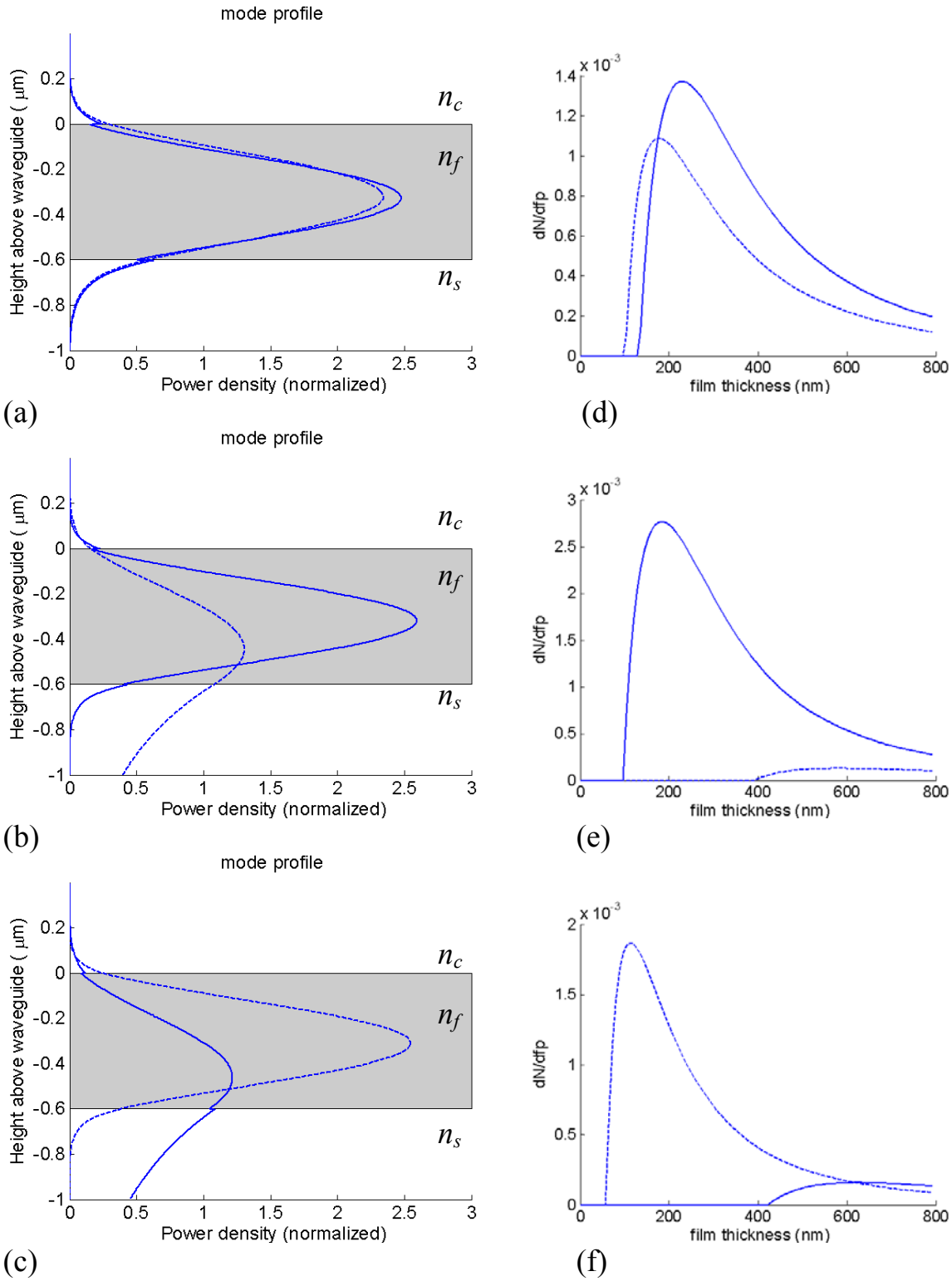

Figure 5.4: (a) Mode intensity profiles for an isotropic film n_f=1.7, (b) birefringent n_e=n_x=1.85, no=1.55 and (c) the configuration ne=ny=1.85, no=1.55; (d),(e),(f)are the corresponding particle fraction sensitivities dN/dfp. Continuous line: TM, dashed: TE.

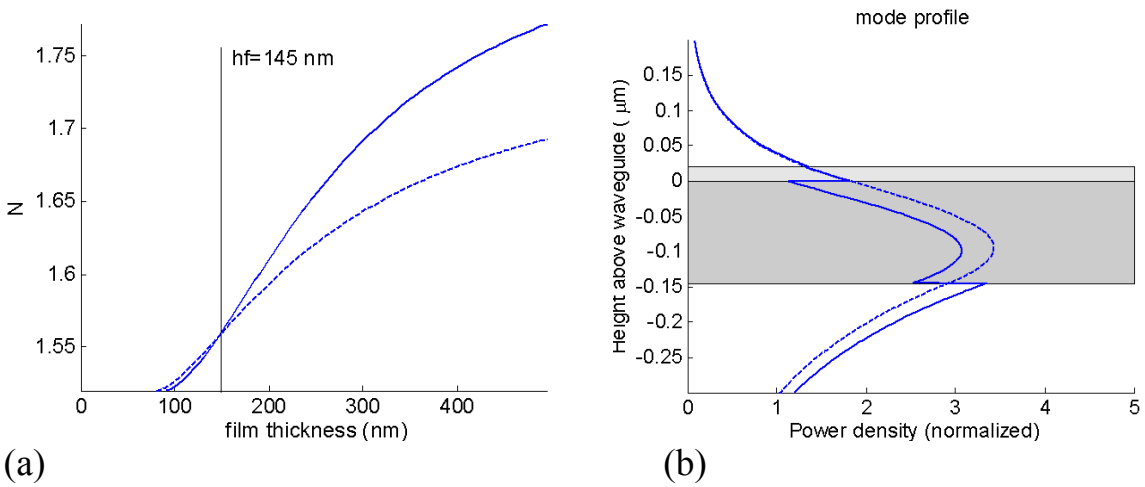

Figure 5.5: (a) Effective refractive index N versus film thickness h_f for n_o=1.75, n_x=n_e=1.85. (b) mode profile for a film thickness of h_f=145nm.

	TE	TM	Rel. S_{TE}/S_{TM}
$S_{nl}=dN/dn_l$	$2.97\cdot10^{-2}$	$4.18\cdot10^{-2}$	100 %
$S_{hl}=dN/dh_l$ (nm^{-1})	$1.46\cdot10^{-4}$	$2.33\cdot10^{-4}$	114 %

Table 5.2 Comparison of adlayer sensitivities for TE and TM modes of the waveguide configuration from Figure 5.5(b)

5.4 Mode excitation by a finite periodic uniform grating

Figure 5.6(a) shows the resonance peak of a finite periodic and uniform waveguide grating with low efficiency, as it is used for biochemical sensor platforms. The simulations obtained with LIME and with the Fourier transform method are compared to the experimental data obtained for a waveguide grating of the same configuration. The graphs show the intensity inside the waveguide at the grating exit versus the incidence angle θ.

The waveguide grating characteristics were: substrate refractive index n_s=1.521, cover refractive index n_c=1.000, n_f=2.117, λ= 632.8 nm, h_f= 150 nm, grating period Λ=360.0 nm, plane wave excitation, TM polarization. The grating has a depth of h_g=12 nm over a length of L=1mm. The effective refractive index of the structure is N=1.628.

For the LIME algorithm, the line transmission factor is the only parameter that has been used to match the model to the experimental data and is τ=0.9993, corresponding to a leakage parameter of $\alpha = 2$ mm^{-1}. In a Matlab® implementation, the calculation time for evaluating the structure composed of 2777 grating lines for 100 different incidence angles was 0.7s on a Pentium 4 running at 1.6GHz.

To obtain the resonance peak shape using the Fourier transform, the structure has been modeled as phase transmission grating between the two media of refractive indices n_f and n_c, with an incident wave having a z component $k_z=k_0 \cdot N$ of the wave vector $\boldsymbol{k}$. This corresponds to the case of an output coupler of infinitely small leakage parameter. The analytical solution of the peak shape is then given by a sinc of width $\Delta\theta \approx \lambda/L = 0.036°$.

Figure 5.6(b) shows the simulation results for both methods for a grating coupler with relatively deep grooves. For this example, the waveguide grating parameters were: n_s=1.456, n_c=1.000, n_f=2.12, λ= 632.8 nm, h_f= 160 nm, Λ=663 nm, plane wave excitation, λ=632.8 in TM polarization. The grating had a depth of h_g=68 nm over a length of L=0.9 mm. The effective refractive index of the structure is N=1.597.

Again, the line transmission parameter has been used to fit the LIME model to the experimental data and is τ=0.97. The curve for the Fourier transform modeling has been obtained by assuming an infinite output coupler of leakage parameter $\alpha = 45$ mm^{-1}. In this case, the analytical solution of the peak shape is given by a Lorentzian curve of width $\Delta\theta \approx 0.68°$.

Figure 5.6(c) shows the evolution of the intensity inside the waveguide of the same configuration as is Figure 5.6(a) for different angles of incidence, as obtained with LIME.

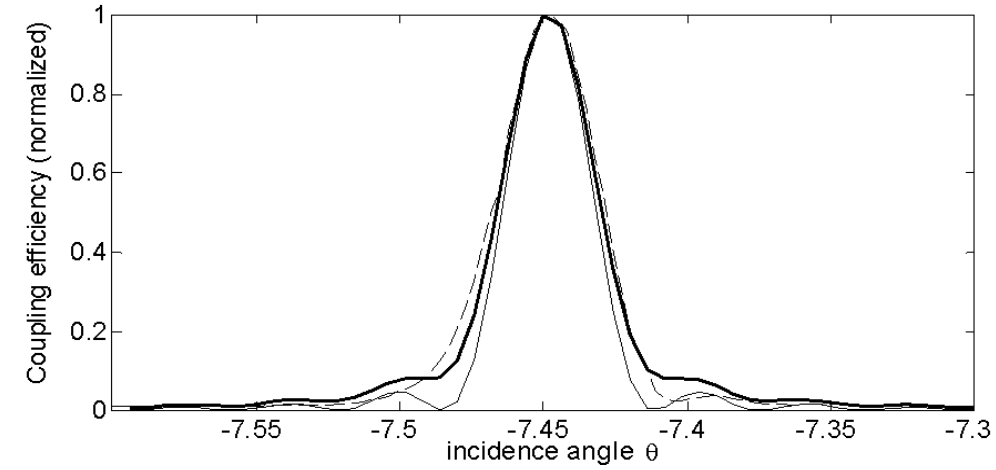

(a)

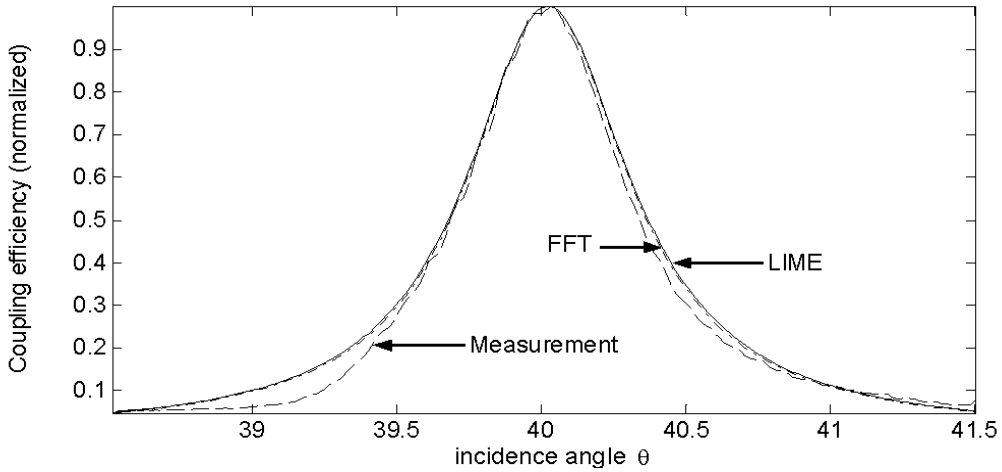

(b)

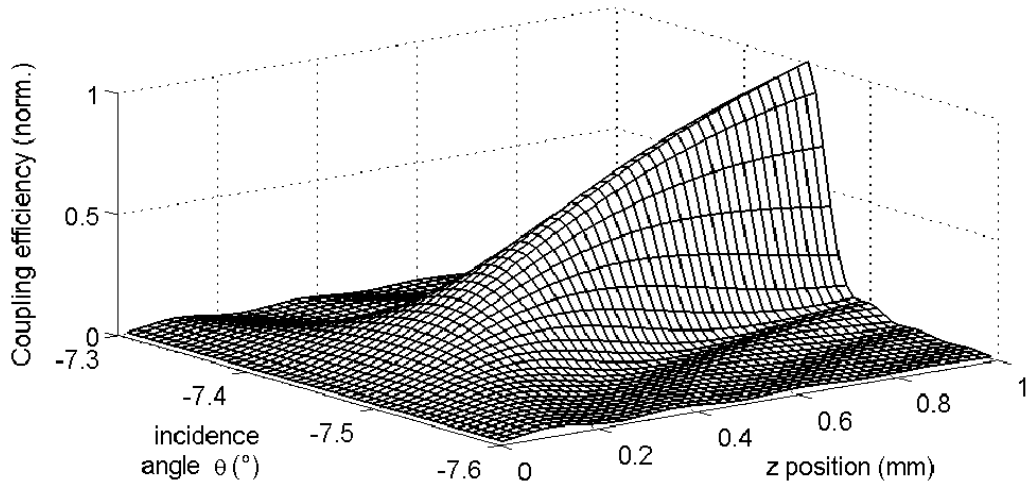

(c)

Figure 5.6: (a) Relative coupling effciences calculated with the LIME (thick solid), and FFT (thin solid) compared to the corresponding experimental data (dashed) for a weakly coupling and (b) for a strongly coupling grating. (c) Evolution of the mode intensity inside the waveguide grating

5.5 Sub-nanometer film thickness variations

Experiments have been reported in [29] suggesting that small effective refractive index variations inside the waveguide grating may lead to a significant distortion of the resonance peak shape.
Figure 5.7 compares an actual measurement to the simulation of the peak shape by LIME. The waveguide grating differs from the first example in section 5.4 for the following characteristics: n_f=2.126, h_f=173.8 nm, N_0=1.695. The same line transmission factor as in the first example has been used.

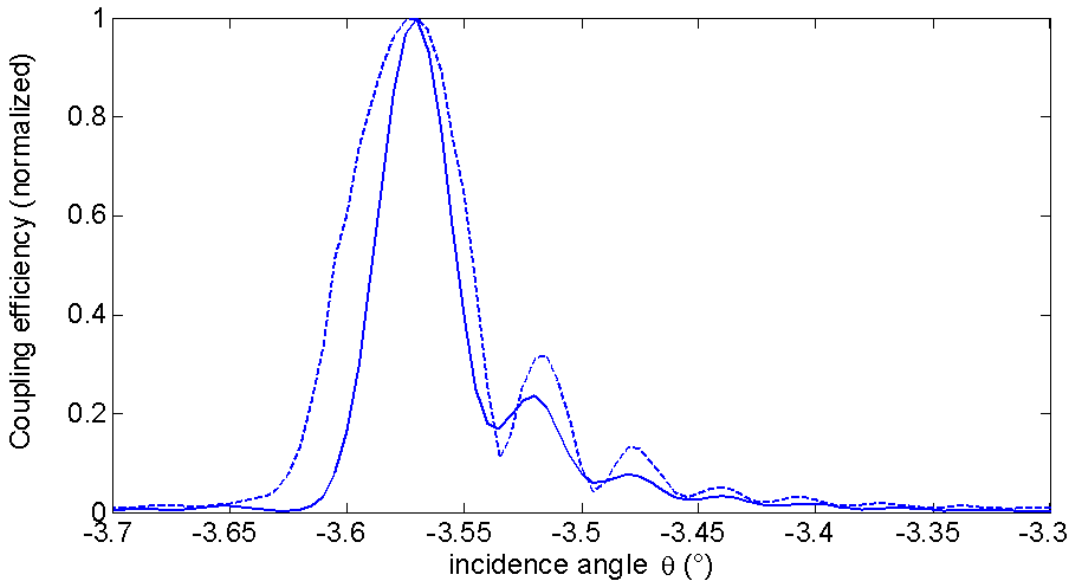

Figure 5.7: LIME Simulation results for a non-uniform waveguide grating (solid) compared to experimental data (dashed)

The effective index variations had been experimentally determined by measuring the local resonance conditions with small spots, created by focussing the beam on the grating as illustrated in Figure 5.8.
A quadratic effective refractive index distribution with respect to the propagation direction was then fitted to the experimental results and used for simulating the line shape. For the above example, the distribution is given by

$$N(z) = N_0 + 5\cdot10^{-3}\ \mathrm{mm}^{-2} \cdot (z\text{-}L/2)^2 \text{ , and } \beta_l = k\cdot N(z_l).$$

The asymmetry observed in the line shapes is caused by the asymmetric propagation constant variations. The partial waveguide modes travelling with different propagation constants sum up coherently, resulting in the caracteristic single-sided lobes visible in Figure 5.7.

As the grating presented non-uniformities both along the y and z coordinate, the measurement visible in Figure 5.7 was taken at a certain position y using a "line-style" illumination, also illustrated in Figure 5.8, and realized using a cylindrical lens of large focal length.
In this example, the non-uniformities were caused by sub-nanometer variations of film thickness across the grating region, introduced by a second etching step of the waveguiding film during the fabrication process. The maximum height variation can be calculated from the effective refractive index distribution and is Δh_f = 0.45 nm. Considering that these extremely small variations occur over a large length scale (the grating length is L=1mm), their impact on the line shape would have been extremely difficult to model with other numerical methods such as FDTD.
Considering the simplicity of the LIME approach, the agreement between measurement and simulation is impressive. The method gives us an insight into the subtle mechanisms including fabrication tolerances that can significantly distort the coupling line shape.

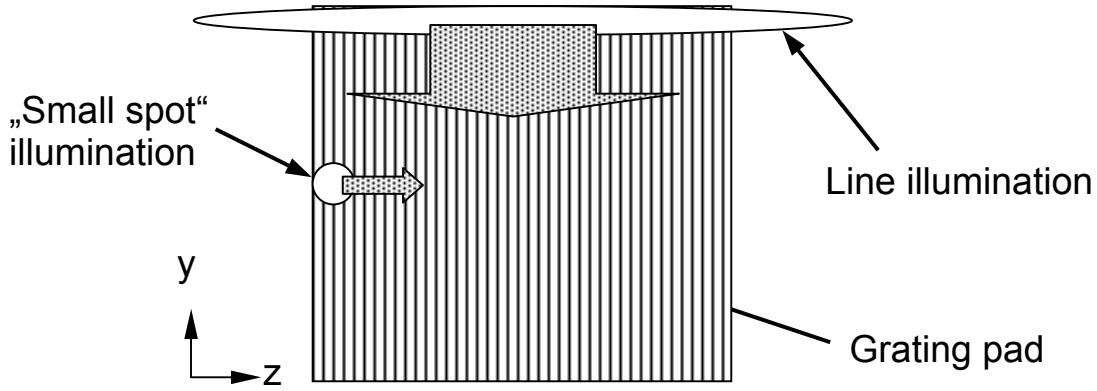

Figure 5.8: Illumination geometry for determining the local propagation constant variations (small spots), and determining the coupling line shape (line-type illumination). The partial illuminations have been scanned across the grating pad as illustrated by the arrows.

5.6 Parasitic substrate reflections

The origin and a theoretical treatment of the parasitic substrate reflections have already been presented in section 3.3. The numerical modeling shown in this section has the goal of evaluating the impact of these reflections on a measurement using the WIOS scheme. The behaviour of an actual measurement with changes of the effective refractive index N is compared to a calibration procedure as suggested in [27], where the incidence angle is varied at a fixed effective refractive index N.

The parameters in eqn (3.3.4) differing for an angular scan and a effective refractive index change are the incidence and exit angles at the input and output coupler, respectively. For an angular scan, the incoupling angle $\theta_{s,in}$ is scanned, while the outcoupling angle $\theta_{s,out}$ follows eqn (3.2.12) and N_{out} remains fixed. In the case of an effective refractive index change, the input coupling angle $\theta_{s,in}$ remains fixed, while the outcoupling angle $\theta_{s,out}$ follows eqn (3.2.12), and N_{out} varies. N_{out} may exhibit a different behavior than N_{in}, as is the case for instance for a depth-modulated sensor layout [29].

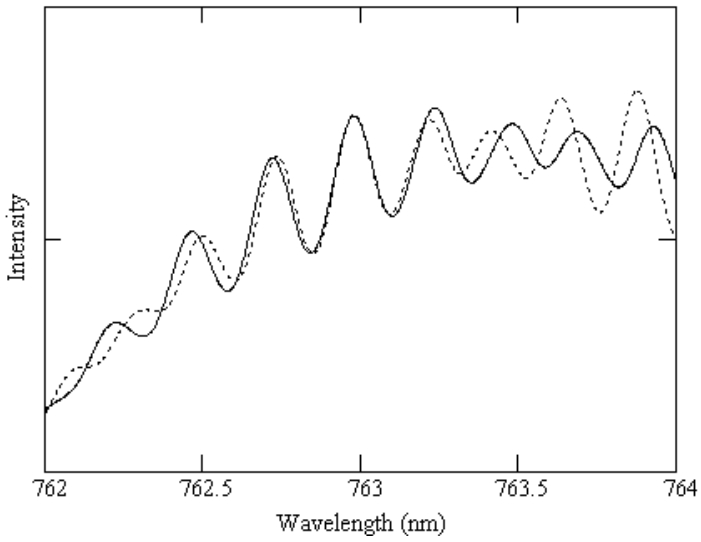

Figure 5.9: Simulation of the amplitude distortion for an angular scan (dashed) and an effective refractive index scan (solid)

Figure 5.9 shows a simulation of the amplitude distortion function $a_{dist}(\lambda)$ for an angular scan (dashed line) and for an effective refractive index scan (solid line), including a reality-inspired laser power non-linearity. The chip parameters correspond to the current depth-modulated chips. The working point for the effective refractive index variation curve is set to an angle corresponding to the center of the wavelength resonance range. An intensity vs. wavelength distribution

$I_1 = f(\lambda)$ has been chosen which corresponds to a VCSEL emission, while the interference modulations are calculated based on (3.3.4).
The amplitude of the modulations is visibly quite high , and the superposition of the two interference contributions of different phase shift $\Delta\phi$ results in a beat visible on both curves. Furthermore, the interference modulations in the case of an angular scan differ significantly from the ones obtained for effective refractive index changes for peaks outside a range of approximately 100 WU (WIOS unit, corresponding to approximately 0.007 nm) around the working point.

A simulation of the deviation of the detected peak position from the theoretical (input) peak position is shown in Figure 5.9. Again, curves for an angular scan and for effective refractive index changes (working point 150 WU) are shown for a depth-modulated chip. The following model was adopted for the simulation: A perfect Lorentz function centered at a wavelength λ_0 was distorted by the corresponding amplitude distortion function from Figure 5.8. Then, the distorted peak was sampled, and a Gaussian fit applied to detect center wavelength λ_{fit}. The difference $\lambda_{fit} - \lambda_0$ is finally plotted in the Figure 5.10.

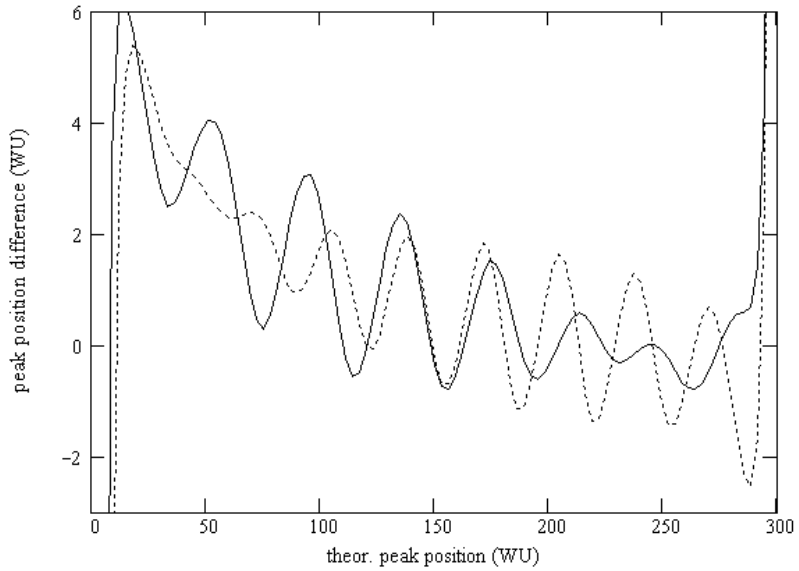

Figure 5.10: deviation of detected peak position from its actual value due to interference modulations: angular scan (dashed) and effective refractive index scan (solid).

Figure 5.11 shows the amplitude distortion function of an angular scan measured on depth-modulated chips. The plot shows the detected wavelength resonance peak amplitude versus incoupling angle. As in the simulations, the resonance wavelength range covers approximately 2nm.

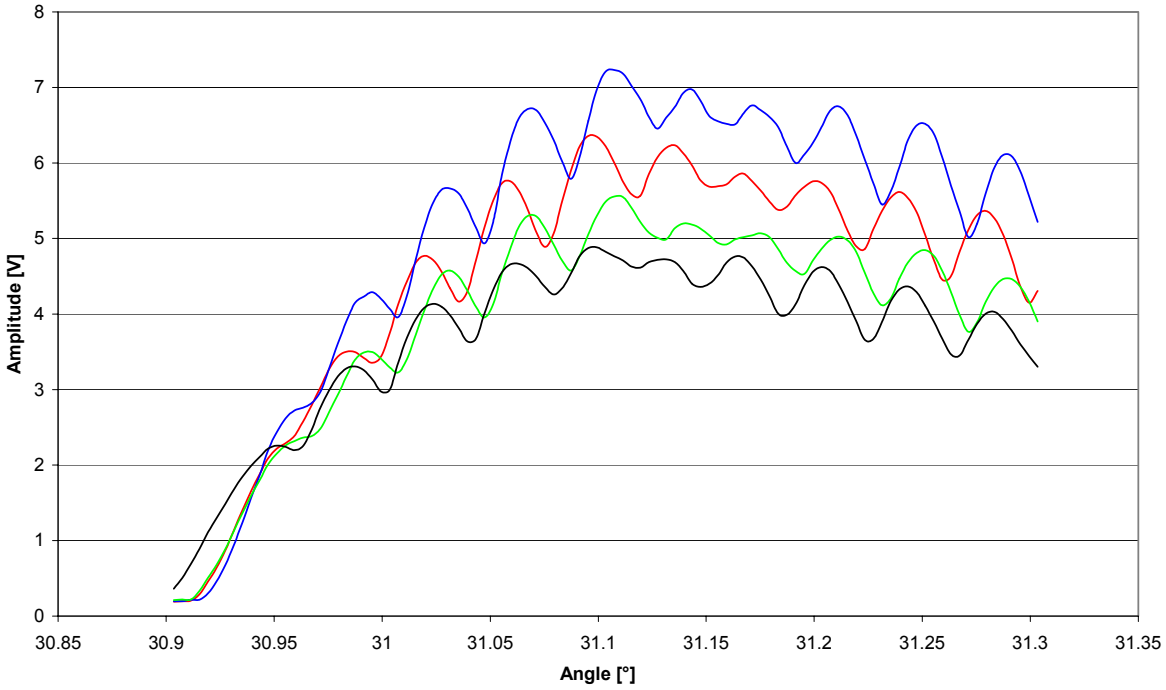

Figure 5.11: Amplitude distortion function for an angular scan of a depth-modulated chip.

Comparing the experimental data with the simulations, it is observed that the periodicity of the main modulation and the beat is in very good agreement with the theoretical predictions for an angular scan. The amplitude of the modulation is approximately ¾ of the calculated maximal value.

The simulations and the measurements show that a calibration of the parasitic substrate reflections is not feasible using an angular scan. For an accurate measurement, it is therefore a prerequisite to avoid these reflections.

Chapter 6

Applications

6.1 Chip design

Based on the theory and modeling established in the framework of this thesis, an overview of the criteria for designing optimized waveguide grating sensor platforms (chips) is given in this section. Furthermore, a chip layout will be presented having improved linearity and sensitivity at potentially lower production costs with respect to current designs.
In summary, the criteria for chip design, which will be explained in this section, include:

1. Acceptable resonance angles
2. Maximum sensitivity
3. Minimum sensitivity to parasitic refractive index changes
4. Minimal interference modulation
5. Low crosstalk
6. Acceptable resonance peak width
7. Minimum size for maximum arraying
8. Low production cost

In theory, the wavelength and the refractive indices of the different layers of the waveguide structure can be chosen freely for chip design. In practice, most parameters are given by the capacities of the production facilities and the availability of the components used for sensor readout. In the example of the wavelength readout using a vertical cavity surface-emitting laser (VCSEL), the availability of interesting lasers is currently limited to the near infrared. The choice of Glass substrates instead of replicated polymer chips is justified by the improved mechanical and chemical stability [28], which however results in increased production costs. Furthermore, a Ta_2O_5 metal-oxide film is chosen, as the production of this kind of chips has been optimized throughout the past years at Unaxis Balzers Optics, Ltd. The films are of excellent quality and reproducibility.

The following parameters are therefore given for the optimization:

n_s	Substrate index of refraction	1.52	(Schott D263 or AF45)
h_s	Substrate thickness	0.7 mm	
n_f	Film index of refraction	2.10	
n_c	Cover index of refraction	1.328	(water)
λ	Center wavelength	763 nm	
n_l	adlayer index of refraction	1.45	(protein)
f_p	particle fraction (see section4.1)	0.1	(unsaturated layer)

A description of the fabrication process used can be found in [29].

6.1.1 Acceptable resonance angles

The criteria for acceptable resonance angles are given by practical considerations. Except for configurations where this is the actual measured variable, reflections from the excitation beam should not be incident on the detector. Otherwise, this would result in background or interference. To avoid this, the condition for the input and output beam should be chosen to happen at different angles.
Furthermore, the angles should be chosen in order to allow simple mechanical realization without the use of elements like beamsplitters etc. Finally, every resonance angle should be comprised between –60° and 60°. Angles outside this range result in difficulties with respect to illumination, as the intensity incident on the grating scales with the cosine of the incidence angle.

6.1.2 Maximum sensitivity

Guidelines for optimizing sensitivity have been already presented in section 5.1.

6.1.3 Minimum sensitivity to parasitic refractive index changes

Parasitic refractive index changes of the cover medium have been treated in section 5.1.3. The sensing layer to bulk signal ratio (SBSR, introduced by Kunz and Cottier in [53]) is an important design criterion and has to be balanced against maximum sensitivity.

6.1.4 Minimum interference modulation

The theoretical background of the interference modulation effect has been established in section 3.3, while modeling results have been presented in section 5.7.

Based on this knowledge, the following approaches are suggested for avoiding or minimizing the effect:

a) Limit the reflection coefficient at the substrate-air interface
b) Limit the reflection coefficient at the waveguiding film
c) Reduce the overlap of the two interfering waves

Point a) is implemented by an anti-reflective (AR) coating, or by choosing resonance conditions near the Brewster's angle. The latter solution has the advantage of not causing additional production steps. Point b) may be implemented by choosing an appropriate film thickness, i.e. have the film behave like an AR-coating. However, the film thickness is an important parameter for sensitivity and SBSR optimization (see section 5.1). Therefore, it is preferred not to include it into the interference modulation considerations. Finally, Point c) is best addressed by choosing a small grating pad length and high resonance angles. Especially for output couplers, the overlap of the twice-reflected beam with the original beam can be effectively reduced by this means.
Other possibilities like reducing the planarity of the substrate or reducing the coherence of the beam are not considered here, as good results are already obtained with the less complicated and expensive solutions cited above.

6.1.5 Low Crosstalk

On sensor arrays where several sensing units are read out in parallel and at the same time (see section 2.2), it is important to minimize the crosstalk between the different channels. This requires a careful layout of the detection. Approaches for suppressing the crosstalk include the isolation of the sensing units by etching down the waveguiding film below cutoff outside the active area, or by using "strong" output couplers that almost completely remove the light from the waveguide.

6.1.6 Acceptable resonance peak width

The resonance peak width has an impact on resolution and measurement range. A narrow peak does not necessarily mean high resolution, as a spread of the peak over several sampling points results in an effective averaging. The resonance peak width is primarily determined by the grating length and the grating depth (see section 3.2). As a rule of thumb, long grating pads result in narrow peaks, and short pads in broad peaks; efficient gratings result in broad peaks, and weak gratings in narrow peaks.

6.1.7 Minimum size for maximum arraying

The smaller the size of the sensing units, the more of them can be packed onto the same chip surface. Close packing is usually traded against increased crosstalk.

6.1.8 Low Production cost

A cost-effective layout has a reduced number of fabrication steps. Furthermore, cost effective steps are preferred over cost-intensive steps, for instance by replacing holographic exposure steps by standard exposures. An example is found in [29], where the fabrication of thickness-modulated chips is described.
Another aspect of production cost is the yield. For this reason, chip optimization includes considerations about sensitivity to fabrication tolerances. For a given production process, the chips with a lower sensitivity to the tolerances will show a higher yield, resulting in a lower overall cost per chip.

6.1.9 Improved layout

Based upon the design considerations mentioned in 6.1.1 through 6.1.8, an improved input coupler layout for the WIOS sensing scheme has been designed, fabricated and characterized. The design is based upon a long-period grating. Traditionally, short period ($\Lambda<\lambda$) are preferred over long-period ($\Lambda>\lambda$) gratings, as higher orders are suppressed. For wavelength readout schemes however, the secondary sensitivity scales with the grating period. The parameters of the proposed layout are as follows:

n_s	Substrate index of refraction	1.52
h_s	Substrate thickness	0.7 mm
n_f	Film index of refraction	2.10
h_f	Film thickness	180nm
Λ	Grating period	900nm
λ	Design wavelength	763 nm

The layout is optimized for the following adlayer and cover configuration

n_c	Cover index of refraction	1.328	(water)
n_l	adlayer index of refraction	1.45	(protein)
f_p	particle fraction (see section4.1)	0.1	(unsaturated layer)

The following key advantages over current designs are achieved:

- 100% Higher sensitivity due to long period gratings
- 10% Higher SBSR due to higher film thickness
- No interference modulations due to incidence near Brewster's angle
- Potentially lower production cost due to longer-period gratings

The disadvantage of this layout is a slightly reduced measurement range due to a broadened resonance peak.

A first batch of optimized chips was produced having a slightly different configuration, as this way a rapid and inexpensive fabrication was assured. The layout had a second waveguiding film on top of the primary waveguide while the substrate was a quartz wafer. The parameters measured at 763nm were

n_s	Substrate index of refraction	1.46	(Quartz)
h_s	Substrate thickness	0.5 mm	
n_{f1}	Primary film index of refraction	2.10	(Ta_2O_5)
h_{f1}	Primary film thickness	150nm	
n_{f2}	Secondary film index of refraction	1.88	(SiN)
h_{f2}	Secondary film thickness	48nm	
Λ	Grating period	900nm	

The corresponding theoretical values of the optimized (A) compared to the actually fabricated (B) and the current design (C) are given in table 6.1. The (measured) wavelength difference detection limit $\Delta\lambda$ of $7 \cdot 10^{-5}$ has been used for the calculations.

Config	$d\lambda/df_p$ (nm)	$\Delta\Gamma$ (fg/mm^2)	SBSR	Incidence angle (°)	Intensity modul. (%)
A	2.06	170	$1.53 \cdot 10^{-2}$	56	0
B	1.79	190	$1.55 \cdot 10^{-2}$	54	<1
C	1.02	340	$1.38 \cdot 10^{-2}$	-32	20

Table 6.1 Comparison of key performance data of optimized (A), fabricated (B) and current (C) chip layout: Sensitivity, mass detection limit, incidence angle and expected intensity modulation due to interference effects.

The chips have been characterized both on a dedicated chip characterization set-up (see section 6.2 for description) and in actual biochemical measurements. Figure 6.1 compares the modulation visible on the coupling line maxima for a current WIOS chip (a) and for the optimized layout as it has been fabricated (b). The suppression of the parasitic reflections thanks to the angle of incidence near the Brewster's angle is well visible.

Figure 6.2 (a) shows a bulk refractive index experiment for the current design, which is compared to the results obtained for the optimized layout as it has been fabricated (Fig. 6.2(b)). Although the sensor is not obtimized for cover refractive index changes, this experiment has been chosen for confirming enhanced sensitivity, as it involves purely physical and reproducible effects and does not depend on the surface properties such as hydrophobicity. The enhanced sensitivity (+55%) is well visible as enhanced peak shift. The experimental result corresponds well to the expected sensitivity enhancement (+58%) for the

cover refractive index experiment. Due to the increased SBSR ratio, it is expected that the sensors have a significant higher sensitivity increase (+80%) for biochemical experiments, as can be seen from table 6.1.

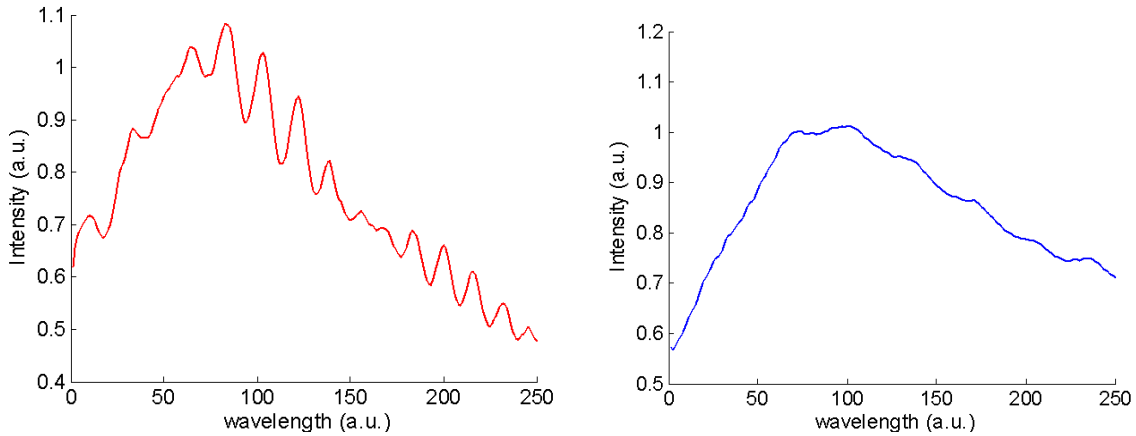

Figure 6.1: Measurement of the modulations on the coupling peak maxima of the (a) current and (b) optimized layout.

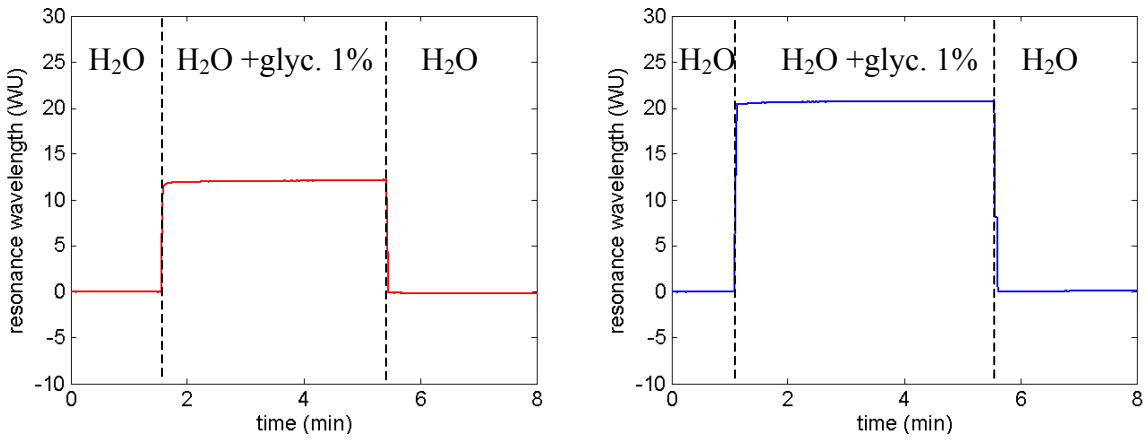

Figure 6.2: Measurement of a cover refractive index step of 1% Glycerol using the (a) current and (b) optimized layout. The step corresponds to a difference of Δn_c=0.0012

6.2 Chip testing

For the development and optimization of high quality chips, a system for characterizing chip performance was built in the framework of an industrial project [62]. The device is based on the WIOS measuring principle. As in the sensor instrument, a current-tunable diode laser source is used to scan the coupling condition of the sensing pads. The resulting resonance curve is then analyzed by characterizing it's signal position and shape. The system is suited for measuring whole wafers in the production process by providing degrees of freedom for adjusting the excitation and detection angles and for addressing individual pads. A modular holder design for the light source, the detector and chips allows characterizing the chips under different conditions. Figure 6.3 shows a picture of the measurement unit.

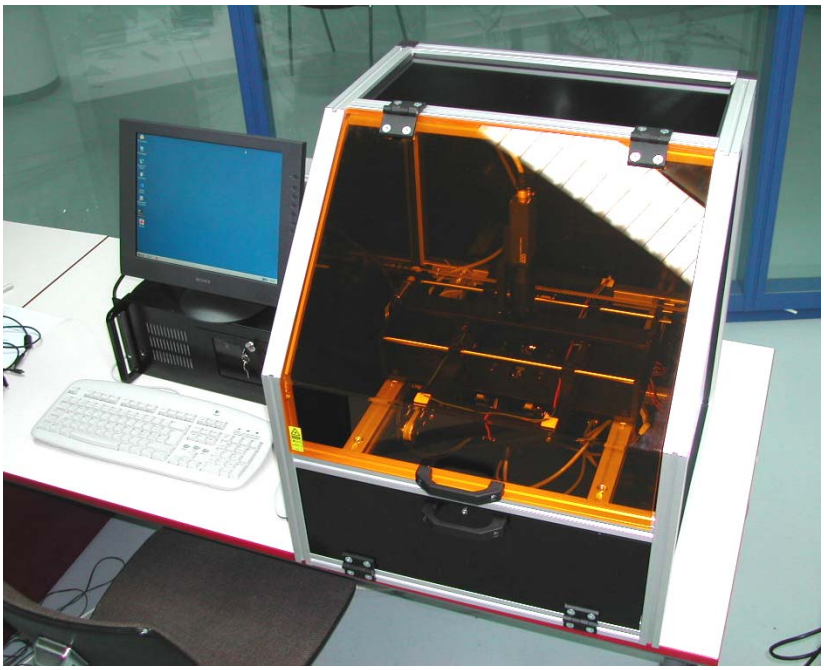

Figure 6.3: Chip characterization system

The chip characteristics, which can be measured by the system, include:

- The resonance angle and wavelength
- The variations between different sensing pads present on the chip
- The shape and distortions in the resonance curve

From this data, the film thickness (and the refractive index) is calculated using the algorithms described in section 4.2.

Due to the inherent sensitivity of the waveguide gratings to film thickness changes, sub-nanometer thickness variations can be determined over the length scale of a whole wafer using the characterization system.

The following Figs 6.4 (a) and (b) show an example of improvement of the chip quality achieved for thickness-modulated [29] chips using an optimized production process. The figures show film thickness variations inside one wafer, as measured with the characterization system. Every point represents a sensing unit. In this layout, a chip is composed of 6 sensing units, with a total of 49 chips per wafer. The measurement time for a whole wafer is below 10 minutes.

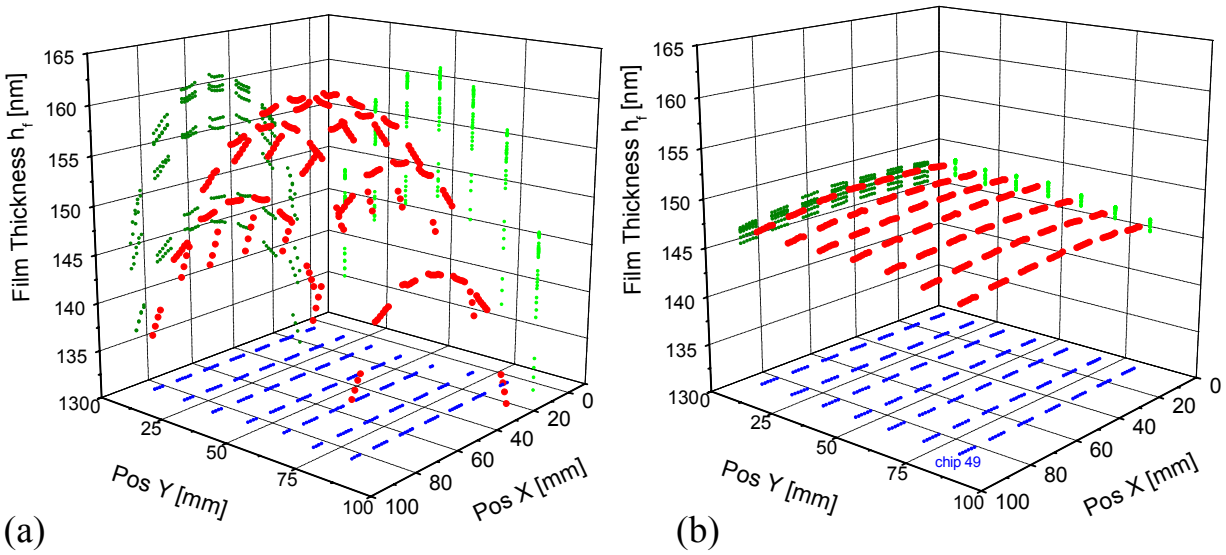

Figure 6.4: Measurement of the grating pad thickness variations on the wafer scale: waveguide thickness using (a) non-optimized production process (b) optimized process (courtesy of UNAXIS Baltzers Ltd.)

In summary, the optimization of the production process was significantly aided and sped up by the characterization and analysis methods and devices that have been developed throughout this thesis. It allowed establishing a production process at Unaxis Balzers, Ltd. for industrial chip production. High quality sensor platforms can now be fabricated in large quantities.

Chapter 7

Conclusions and Outlook

Novel approaches for modeling label-free biochemical sensors based on waveguide gratings have been presented. The methods have been introduced and discussed in detail, and the application to practical analysis and engineering tasks has been presented. In addition, an in-depth presentation of the known theoretical background necessary for understanding and evaluating such devices is given in one document for the first time.

A novel approach for deriving the mode condition in a multilayer slab waveguide has been presented. Based upon this approach, a simple yet robust formulation of a mode search algorithm has been implemented and used successfully. The software includes a complete treatment of multilayer systems having birefringent layers. It performs a wide variety of relevant design and analysis calculations, such as 2D and 3D Plots of angular and spectral dependencies, sensitivities and SBSR, as well as waveguide parameter determination based on a set of measurements by multi-variable optimization. This software has been successfully used to fulfill a variety of design and analysis tasks, such as sensor optimization and characterization.

A new method for describing mode excitation through a grating coupler has been presented. The local interference method (LIME) is a good approximation for calculating resonance shapes of (non-uniform) waveguide gratings. It includes both diffraction and waveguiding effects. Computing time is comparable to the Fourier transform method. The presented application examples show that the method is very attractive for evaluating coupling line shapes of one grating order and for gaining a deeper understanding of the coupling process. Peak distortions due to very small waveguide inhomogeneities calculated with LIME show good agreement with the corresponding measurements. The simulation results have been obtained without calculating the exact value of the grating parameters. An estimation of the latter is sufficient for the evaluation of normalized coupling line shapes.

Based on these models, a characterization set-up has been built for analysis of the sensor chips during the production process. The optimization of the fabrication process of a special type of sensor platforms has been significantly aided by this efficient measuring tool. High quality sensor platforms can now be fabricated in large quantities.

Finally, the practical relevance of the work has been demonstrated by showing the results obtained by optimized sensor platforms, engineered using the design rules and methods developed in the framework of this thesis. The chips show enhanced sensitivity combined with a lower sensitivity to parasitic bulk refractive index changes, and no interference modulations.

The present work found application in various industrial projects with international partners. Many of the projects are still ongoing and producing exciting results. New approaches for sensor design and readout not mentioned in this thesis, as well as new materials for waveguides are currently being evaluated and patented.

I hope that this thesis is a useful contribution to the research in the field of waveguide grating sensors.

References

[1] M. A. Cooper, “Optical Biosensors in Drug Discovery” Nature Reviews on Drug Discovery, 1, 2002

[2] K. Nagata, H. Handa (Eds.), *Real-Time Analysis of Biomolecular Interactions: Applications of BIACORE*, Springer, Verlag, 2000.

[3] J.Homola, S. S.Yee, G. Gauglitz, "Surface plasmon resonance sensors: review." Sensors&Actuators, B, 54, 3-15, 1999.

[4] www.biacore.com

[5] www.appliedbiosystems.com

[6] www.ti.com

[7] www.srubiosystems.com

[8] www.farfield-sensors.com

[9] www.q-sense.com

[10] F. Höök, M. Rodahl, J. Vörös, R. Kurrat, P. Böni, J.J. Ramsden, M. Textor, N.D. Spencer, P. Tengvall, J. Gold, B. Kasemo, “A comparative study of protein adsorption on titanium oxide surfaces using in situ ellipsometry”, optical waveguide lightmode spectroscopy, and the quartz crystal microbalance/dissipation, Coll. Surf. B: Biointerf. 24, 155–170, 2002.

[11] www.ciphergen.com

[12] R. Horvàth, J. Vörös, R.Graf, G. Fricsovszky, M. Textor, L.R. Lindvold, N.D. Spencer, E. Papp, “Effect of patterns and inhomogeneities on the surface of waveguides used for optical waveguide lightmode spectroscopy applications”, Appl. Phys. B 72, 441–447, 2001

[13] K. Tiefenthaler and W. Lukosz, "Sensitivity of grating couplers as integrated-optical chemical sensors," J. Opt. Soc. Am. B, Vol. 6, No. 2, 209-220, 1989

[14] R.G. Heideman, R.P.H. Kooyman and J. Greve, "Performance of a highly sensitive optical waveguide Mach-Zehnder interferometer immunosensor," Sensors and Actuators B, Vol. 10, 209-217, 1993

[15] A. Brandenburg, R. Krauter, C. Künzel, M. Stefan, H. Schulte, “Interferometric sensor for detection of surface-bound bioreactions”, Appl. Opt.-OT 39(34) 6396.

[16] A. Ymeti, J.S. Kanger, R. Wijn, P.V. Lambeck, J. Greve, “Development of a multichannel integrated interferometer immunosensor”, Sens. Actuators B 83, 1–7, 2002.

[17] R. Cush, J.M. Cronin, W.J. Stewart, C.H. Maule, J. Molloy, N.J. Goddard, “The resonant mirror: a novel optical biosensor for direct sensing of biomolecular interactions. Part 1. Principle of operation and associated instrumentation”, Biosens. Bioelectron. 8, 347–353, 1993.

[18] R. Tünnemann, M. Mehlmann, R.D. Süssmuth, B. Bühler, S. Pelzer, W. Wohlleben, H.P. Fiedler, K.H. Wiesmüller, G. Gauglitz, G. Jung, “Optical biosensors. monitoring studies of glycopeptide antibiotic fermentation using white light interference”, Anal. Chem. 73, 4313–4318, 2001

[19] G. Ladam, P. Schaad, J.C. Voegel, P. Schaaf, G. Decher, F. Cuisinier, “In situ determination of the structural properties of initially deposited polyelectrolyte multilayers”, Langmuir, 16, 1249–1255, 2000

[20] D.S. Ballantine, R.M. White, S.J. Martin, A.J. Ricco, E.T. Zellers, G.C. Frye, H. Wohltjen, *Acoustic Wave Sensors: Theory, Design, and Physico-Chemical Application*, Academic Press, San Diego, 1997.

[21] W. Lukosz, "Principles and sensitivities of integrated optical and surface plasmon sensors for direct affinity sensing and immunosensing," Biosensors & Bioelectronics, Vol. 6, 215-225, 1991

[22] Robert Horvath, Henrik C. Pedersen, Nina Skivesen, David Selmeczi, Niels B. Larsen, “Optical waveguide sensor for on-line monitoring of bacteria” Optics Letters, Vol. 28 Issue 14 Page 1233, 2003

[23] P.N. Zeller, G. Voirin and R.E. Kunz, “Single-pad Scheme for Integrated Optical Fluorescence Sensing”, Biosensors and Bioelectronics, Vol.15/11-12, 591-595, 2001

[24] W. Lukosz and K. Tiefenthaler, "Directional switching in planar waveguides effected by adsorption-desorption processes," IEE Conf. Publ. 227, 152-155, 1983

[25] R.E. Kunz, J. Edlinger, P. Sixt and M.T. Gale, “Replicated Chirped Waveguide Gratings for Optical Sensing Applications,” Sensors and Actuators A, Vol. 47, 482-486, 1995

[26] M. Wiki, H. Gao, M. Juvet and R.E. Kunz, "Compact Integrated Optical Sensor System," Biosensors and Bioelectronics, Vol. 16, No. 1-2, 37-45, 2001

[27] K. Cottier, M. Wiki, G. Voirin, H. Gao, and R.E. Kunz, “Label-free highly sensitive detection of (small) molecules by wavelength interrogation of integrated optical chips”, Sensors&Actuators B, vol 91/1-3, 241 – 251, 2003, reprinted in Appendix A of the present thesis

[28] M. Wiki and R.E. Kunz, "Wavelength-interrogated optical sensors for biochemical applications," Opt. Lett. Vol. 25/7, 463-465, 2000

[29] K. Cottier, R.E. Kunz, G. Voirin, M. Wiki, “Thickness-modulated waveguides for integrated optical sensing”, Proc. SPIE Vol. 4616, 53-63, 2002, reprinted in Appendix B of the present thesis

[30] R.E. Kunz, G. Duveneck and M. Ehrat, “Sensing Pads for Hybrid and Monolithic Integrated Optical Immunosensors,” Proc. SPIE, Vol. 2331, 2-17, 1994

[31] H. Gao, M. Sänger, R. Luginbühl and H. Sigrist, "Immunosensing with photoimmobilized immunoreagents on planar optical wave-guides", Biosensors & Bioelectronics 10, 317 – 328, 1995

[32] J. Dübendorfer, R.E. Kunz, E. Schürmann, G.L. Duveneck and M. Ehrat, "Sensing and Reference Pads for Integrated Optical Immunosensors", Journal of Biomedical Optics, Vol. 2, 391-400, 1997

[33] R.E. Kunz, "Miniature Integrated Optical Modules for Chemical and Biochemical Sensing", Sensors and Actuators B, Vol. 38-39, 13-28, 1997

[34] B. Cunningham, P. Li, B. Lin, J. Pepper, "Colorimetric resonant reflection as a direct biochemical assay technique", Sensors and Actuators B, Volume 81, 316-328, 2002.

[35] M. G. Moharam and T. K. Gaylord, "Diffraction analysis of dielectric surface-relief gratings" J. Opt. Soc. Am., 72, 1385-1392, 1982

[36] J. Turunen, "Diffraction theory of microrelief gratings." In *Micro-optics*, H. P. Herzig, editor, Taylor & Francis Inc., 1997

[37] P. Lalanne, G.M. Morris, ”Highly improved convergence of the coupled-wave method for TM polarization”, JOSA 13/4, 779-784, 1996

[38] Lifeng Li, “Formulation and comparison of two recursive matrix algorithms for modeling layered diffraction gratings”, J. Opt. Soc. Am. A 13, 5, 1996

[39] Lifeng Li, Jean Chandezon, Gérard Granet, and Jean-Pierre Plumey, “Rigorous and efficient grating-analysis method made easy for optical engineers”, Appl. Opt. 38, 304-313, 1999

[40] A. V. Tishchenko, M. Hamdoun, and O. Parriaux "Two-dimensional coupled mode equation for grating waveguide excitation by a focused beam", Opt. Quantum Electron. Special Issue on Workshop WTNM, Nottingham, 2001

[41] R.H. Morf, "Exponentially convergent and numerically efficient solution of Maxwell's equations for lamellar gratings", J. Opt. Soc. Am. A, Vol. 12, 1043-1056, 1995

[42] R.E. Kunz, J. Duebendorfer and R.H. Morf, "Finite Grating Depth Effects for Integrated Optical Sensors with High Sensitivity", Biosensors and Bioelectronics, Vol. 11, 653-667, 1996

[43] B.E.A Saleh and M.C. Teich, *Fundamentals of Photonics*, Wiley, New York, 1991

[44] S.J. Orfanidis, *Electromagnetic waves and antennas*, available online at www.ece.rutgers.edu/~orfanidi/ewa/

[45] J. W. Goodman, *Introduction to Fourier Optics*, 2nd ed., McGraw-Hill, New York, 1996.

[46] R. Ulrich, "Efficiency of optical-grating couplers", JOSA, Vol. 63 Issue 11, 1419, 1973

[47] E. Moreno, D. Erni, C. Hafner, R.E. Kunz and R. Vahldieck, „Modeling and optimization of non-periodic grating couplers", Optical and Quantum Electronics 34, 1051–1069, 2002

[48] R. Dändliker, "Coupled Waves: A Powerful concept in modern optics" Proc. SPIE, Vol. 3190, 279-288, 1997

[49] Dridi, K.H. and A. Bjarklev, "Optical Electromagnetic Vector-Field Modeling for the Accurate Analysis of Finite Diffractive Structures of High Complexity", Appl. Opt. 38, 1668-1675, 1999.

[50] G.Sztefka ans N. Holting, "Bidirectional eigenmode propagation for large refractive index steps", IEEE Photon. Technol. Lett.5, 554-557, 1993

[51] M. Born and E. Wolf, *Principles of Optics*, 6th ed., Pergamon, New York, 1980

[52] W. H. Press, S. A. Teukolsky, W. T. Vetterling and B. P. Flannery, *Numerical Recipes in Fortran (or in C or in Pascal): The Art of Scientific Computing*, 2nd Ed., Cambridge University Press, 1992. Available online at www.nr.com

[53] R.E. Kunz, K. Cottier, "Application-Tailored Integrated Optical Chips for Label-free (Bio-)chemical Sensing", submitted to S&A B

[54] K. Cottier, R.E. Kunz, H.P. Herzig, “Efficient and practical modeling of finite waveguide grating couplers”, accepted for publication in the JJAP, 2004

[55] T.Tamir and S.T.Peng, “Analysis and design of grating couplers”, Appl.Phys. 14, 235-254, 1977

[56] V.A.Sychugov, A.V. Tishchenko, B.A. Usievich, ”Optimization and control of grating coupling to or from a silicon-based optical waveguide”, Optical Engineering 35, 3092-3100, 199)

[57] M. G. Moharam, Eric B. Grann, and Drew A. Pommet, “Formulation for stable and efficient implementation of the rigorous coupled-wave analysis of binary gratings” J. Opt. Soc. Am. A. 12/.5, 1995

[58] A.V. Tishchenko ”Generalized source method: New possibilities for waveguide and grating problems,” Opt. and Quantum Electron. 32(6/8) 971-980, 2000

[59] P. Bienstman and R. Baets, “Optical modeling of photonic crystals and VCSEL’s using eigenmode expansion and perfectly matched layers,”Opt. Quantum Electron., 33, 327–341, 2001.

[60] D. Freiner, R.E. Kunz, D. Citterio, U.E. Spichiger, and M.T. Gale, "Integrated Optical Sensors based on Refractometry of Ion-selective Membranes," Sensors and Actuators B, Vol. 29, 277-285, 1995

[61] J. Dübendorfer, R.E. Kunz, G. Jobst, I. Moser and G. Urban, "Integrated Optical pH Sensor using Replicated Chirped Grating Coupler Sensor Chips," Sensors and Actuators B, Vol. 50/3, 210-219, 1998

[62] CTI project No. 5165.1, "HiPerChips: New Fabrication Methods for Low-Cost High-Performance Integrated Optical Sensor Chips," 2001-2002

Curriculum vitae

Kaspar Cottier
kcottier@postmail.ch

Education

2004	Dr. ès sciences (PhD), University of Neuchâtel, Switzerland
2001	Ing. dipl. microtechn. (MS), orientation Applied Photonics, Swiss Federal Institute of Technology Lausanne (EPFL), Switzerland
1996	Matura (BA) orientation Latin and languages, Gymnasium Liestal, Switzerland

Experience

2001-2004	PhD thesis on "Advanced Biochemical Sensors Based on Integrated Optical Waveguide Gratings" at CSEM Neuchâtel
2000-2001	Diploma work (MS thesis) on "Fourier Transform Microspectrometer System Based on Liquid Crystal Optical Elements" at CSEM Zürich
2000	Student assistant, Java programming on "Online Ray Tracing for Paraxial Systems" at the Institute of Applied Optics (IOA), EPFL
1999-2000	Initiator of the "Online Ray Tracing for Paraxial Systems" Java project in the framework of a semester project at the Institute of Applied Optics (IOA), EPFL
2000	Semester project "Adaptive Liquid Crystal Micro Lens" at the Institute of Microengineering (IMT), University of Neuchâtel
1998-2000	Student assistant, Java programming on the "Logidules Simulator" at the Microprocessor systems lab (LAMI), EPFL
1998	Freelance microcontroller (HC11) programming for Dreamlab Inc., Bern

Languages

German
French
English

List of publications and patents

Peer-reviewed Publications

- K. Cottier, R.E. Kunz, G. Voirin, "Advanced waveguide grating sensors", Encyclopedia of sensors (invited, submission July 2004)
- R.E. Kunz and K. Cottier "Application-tailored integrated optical chips for label-free (bio-)chemical sensing", submitted to Sensors&Actuators B, 2004
- K. Cottier, R.E. Kunz and H.P. Herzig, "Efficient and practical modeling of finite waveguide grating couplers", accepted for publication in JJAP, 2004
- K. Cottier, M. Wiki, G. Voirin, H. Gao, and R.E. Kunz, "Label-free highly sensitive detection of (small) molecules by wavelength interrogation of integrated optical chips", Sensors&Actuators B, vol 91/1-3 241 – 251, 2003
- T. Scharf, K. Cottier, R. Dändliker, "High Quality Adaptive Liquid Crystal Microlenses", Mol. Cryst. Liq. Cryst. 366, 2265, 2001

Conference proceedings

- K. Cottier, R.E. Kunz, H.P. Herzig, "Efficient and practical modeling of finite waveguide grating couplers", Technical digest of the ninth Microoptics Conference, 36-39, 2003
- K. Cottier, R.E. Kunz, G. Voirin, M. Wiki, "Thickness-modulated waveguides for integrated optical sensing", Proc. SPIE Vol. 4616, 53-63, 2002

Patents and patent applications

- US 60/572,556 (pending) L. Hlousek, R.E. Kunz, G. Voirin, K. Cottier "Integrated optical waveguide sensors with reduced signal modulation"
- EP04405032-6 (pending), K. Cottier, R.E. Kunz, "Incidence angle scanning device"
- EP1278049 G.C. Boer, R.F. Dangel, P.Seitz, K. Cottier, T. Scharf "Illumination module for a reflection spectrometer", 2003
- Two more patents pending

CSEM Scientific Reports, available at www.csem.ch

- "WIOS&FIOS: Smart combination of label-free and fluorescence detection for (bio-)chemical sensing applications," G. Voirin, E. Bernard , K. Cottier, R. Ischer, R.E. Kunz, 2003
- "Efficient and practical Modeling of Finite Waveguide Grating Couplers," K.Cottier, R.E. Kunz, H.P. Herzig 1), 2003
- "WIOS: an Easy-to-Use Instrument for Label Free Sensing", K. Cottier, R. E. Kunz, G. Voirin, E. Bernard, R. Ischer, F. Crevoisier, 2002
- "High-Performance Chips (HiPerChips®): Towards Industrialization", K.Cottier, R. E. Kunz, G. Voirin, H.Chai Gao, E. Bernard, R. Ischer, M.Wiki, 2002
- "Thickness-Modulated Waveguides for Integrated Optical Sensing" K.Cottier, R.E. Kunz, G. Voirin, M. Wiki 1), 2001
- "High-Sensitivity Label-Free Detection of Small Molecules" G. Voirin, R.E. Kunz, H. Chai-Gao, F. Crevoisier, E. Bernard, R. Ischer, K. Cottier, 2001
- "High-Performance Chip (HiPerChip®) for (Bio-)Chemical Sensing", R.E. Kunz, K. Cottier, G. Voirin, H. Chai-Gao, F. Crevoisier, M. Wiki, 2001
- "Handheld Fourier Transform Spectrometer Based on Liquid Crystal Optical Elements" G. Boer, P. Seitz, T. Scharf, K. Cottier, 2000

Abstracts of selected publications

R.E. Kunz and K. Cottier
"Application-tailored integrated optical chips for label-free (bio-)chemical sensing",
submitted to Sensors&Actuators B, 2004

Label-free sensing is an important method for many (bio-)chemical applications in fields such as biotechnology, medicine, pharma, ecology and food quality control. Integrated optics based on the use of waveguide modes offers a great potential and flexibility to tailor the properties of the evanescent field to different applications. The results of a numerical study show that this flexibility is founded on the many degrees of freedom that can be used for the integrated optical chip design, in contrast to other technologies such as those based on surface plasmon resonance, for which the materials' properties limit the range of choices. The applications that are explicitely considered and discussed include (1) bulk refractometry, (2) "2D sensing", for example biosensors with adsorption processes occurring within some 10 nm from the chip's surface in a "surface sensing region", (3) "3D sensing" using a "matrix sensing region" with processes to be monitored within some 100 nm from the chip's surface, for example hydrogel-based layers and "optrodes", (4) "micro-volume sensing" with processes or particles to be monitored within probe volumes extending to some 1000 nm from the chip's surface, including any kind of particles and for example biological cells. The findings will enable one to optimize various types of integrated-optical sensors, including interferometers and grating-based sensors.

For the latter three types of applications, it is demonstrated that the integrated optical chips can not only be designed for achieving maximum sensitivity, but also to obtain an optimum "signal-to-background ratio" in the sense of maximizing the sensitivity in the sensing region of interest, but minimizing it in the regions of non-interest, e.g. in the bulk analyte volume.

Keywords: Label-free sensing, (Bio-) chemical sensors, Evanescent-wave sensors, Integrated optical sensor chip, Waveguides.

K. Cottier, R.E. Kunz and H.P. Herzig,
"Efficient and practical modeling of finite waveguide grating couplers", accepted for publication in Jap. J. Appl. Phys., 2004

The local interference method (LIME) is introduced as a tool for simulating guided mode excitation by finite gratings in monomode waveguides. This efficient and versatile calculation scheme considers each grating line as a scattering center radiating into and from the forward-traveling waveguide mode, neglecting multiple scattering processes. This approximation considerably speeds up calculation time while delivering very good results for a broad range of calculation tasks, including non-periodic gratings or waveguides exhibiting small variations of the propagation constant. The algorithm is presented in detail, and it is applied to the calculation of the coupling line shapes of waveguide grating structures used for biochemical sensors, having small spatial non-uniformities.

Keywords: finite waveguide gratings, coupling line shape, numerical modeling, non-periodic gratings, inhomogeneous waveguide gratings, bio-chemical sensors

K. Cottier, M. Wiki, G. Voirin, H. Gao, and R.E. Kunz,
"Label-free highly sensitive detection of (small) molecules by wavelength interrogation of integrated optical chips",
Sensors&Actuators B, vol 91/1-3 p. 241 – 251, 2003

A biochemical sensor system based on wavelength interrogation of integrated optical sensor chips is presented. The combination of a non-mechanical scanning mechanism with sensor chips of high quality and stability allows fast and accurate multi-channel measurements. The emphasis of the present paper lies in detailed design considerations, and the application of the system to high sensitivity sensing tasks.
A series of different experiments is presented, including bulk refractometry and affinity binding. The results show that the detection limit has been enhanced markedly due to the recent developments of new chips and reliable readout instrumentation. At present, the surface mass coverage detection limit is 0.3 pg/mm^2 at a standard deviation of 100 fg/mm^2.

Keywords: Label-free sensing, (Bio-) chemical sensors, Evanescent-wave sensors, Integrated optical sensor chip.

K. Cottier, R.E. Kunz, G. Voirin, M. Wiki
"Thickness-modulated waveguides for integrated optical sensing"
Proc. SPIE Vol. 4616, p. 53-63, 2002

Novel sensor chips for evanescent wave sensing have been developed and investigated for various (bio-) chemical applications. A preferred integrated optical sensing scheme requires an array of independent sensing pads being present on the chip, each one of them having two different regions for in- and out coupling of the optical readout beam. We present a novel chip type, where this goal is achieved by thickness variations of the waveguiding film and one single grating period. The sensor chips consisted of a 300 nm thick Ta_2O_5 waveguide deposited on a glass substrate structured with a uniform grating of 360 nm period. By this optical structure a first coupling angle was defined. Sensing pads with a different coupling angle were realized by etching the film at selected regions down to a thickness of about 150 nm. The performance of the novel chips was demonstrated in various refractometric sensing applications. The experiments included cover medium refractive index variation as well as monitoring of affinity binding of small molecules. A very high resolution of $3x10^{-8}$ in the effective refractive index was achieved. The emphasis of this paper is on describing this approach and on presenting optical chip characterization methods together with modeling results.

Keywords: (Bio-)chemical sensors, Evanescent-wave sensors, Integrated optical sensor chip, Optical chip characterization

Appendix A

Label-free highly sensitive detection of (small) molecules by wavelength interrogation of integrated optical chips

K. Cottier, M. Wiki, G. Voirin, H. Gao, and R.E. Kunz

Published in Sensors & Actuators B, vol 91/1-3 p. 241 – 251, 2003

Available online at www.sciencedirect.com
SCIENCE DIRECT®
Sensors and Actuators B 91 (2003) 241–251
SENSORS AND ACTUATORS B CHEMICAL
www.elsevier.com/locate/sensorb

Label-free highly sensitive detection of (small) molecules by wavelength interrogation of integrated optical chips

K. Cottier[a,*], M. Wiki[b], G. Voirin[a], H. Gao[a], R.E. Kunz[a]

[a]*Centre Suisse d'Electronique et de Microtechnique SA (CSEM), Jaquet-Droz 1, CH-2007 Neuchâtel, Switzerland*
[b]*Unaxis Optics Ltd., P.O. Box 1000, FL-9496 Balzers, Liechtenstein*

Abstract

A bio-chemical sensor system based on wavelength interrogation of integrated optical sensor chips is presented. The combination of a non-mechanical scanning approach with sensor chips of high quality and stability allows fast and accurate multi-channel measurements. The emphasis of the present paper lies in presenting detailed design considerations, and in reporting the application of the system to several high sensitivity sensing tasks.

An excellent performance of the sensor is demonstrated for bulk refractometry and affinity measurements. The bulk refractometric measurements show a detection limit of $<10^{-6}$. For detecting small molecules, a standard deviation in terms of mass coverage of 100 fg/mm^2 is obtained, corresponding to a detection limit of 0.3 pg/mm^2. Furthermore, a very clear signal is observed for biotin (244 Da), indicating a detection limit for the present wavelength interrogated optical sensor (WIOS) system distinctly below 200 Da. For a direct immunoassay at low concentrations, a detection limit in the order of 10^{-11} M is estimated based on the experimental results. The results show that the sensor is perfectly suited for application areas such as medical, food and environmental.

Keywords: Label-free sensing; (Bio-)chemical sensors; Evanescent-wave sensors; Integrated optical sensor chip

1. Introduction

Label-free detection of several analyte molecules being simultaneously present in a liquid or in a gas with high sensitivity is a major requirement for present and future applications of (bio-)chemical sensors, especially for areas such as medical, food and environmental. In this paper, newest results are reported that have been achieved by reading the signal of multiple sensing pads on an integrated optical (IO) chip simultaneously by a tunable laser [1]. Other approaches for label-free sensing making use of dielectric waveguides include optical waveguide lightmode spectroscopy (OWLS) [2,3], chirped grating couplers [4], Mach-Zehnder [5] and Young interferometers [6,7]. Other well-known methods are based on surface plasmon resonance (SPR) [8], resonant mirror [9], reflectometric interference spectroscopy (RifS) [10], scanning angle reflectometry (SAR) [11], surface acoustic waves (SAW) [12], quartz crystal microbalance [13] and fully electrical devices.

The main advantages of the approach presented in this paper are high sensitivity, fast response, small size and low cost. With the use of sensor chips on glass instead of polymer substrates [14], the stability and reproducibility of the measurements increased markedly.

In this paper, the theoretical fundamentals are presented, followed by a description of the sensing principle and the optical scheme. Then, design considerations as well as a detailed description of effects distorting the signal shape and the corresponding calibration possibilities are given. Next, the practical realization of the readout instrument and the measurement procedure are presented. After that, the fabrication of the chips is explained. Finally, experimental results for the application of the system to refractometry, detection of small molecules and low concentrations are reported.

2. Wavelength interrogation method

2.1. Theoretical fundamentals

2.1.1. Waveguide

A planar dielectric multi-layer waveguide is shown in Fig. 1. All layers are supposed to be absorption free and

* Corresponding author. Tel.: +41-32-720-51-79; fax: +41-32-720-57-40.
E-mail address: kaspar.cottier@csem.ch (K. Cottier).

0925-4005/03/$ – see front matter © 2003 Elsevier Science B.V. All rights reserved.
doi:10.1016/S0925-4005(03)00117-5

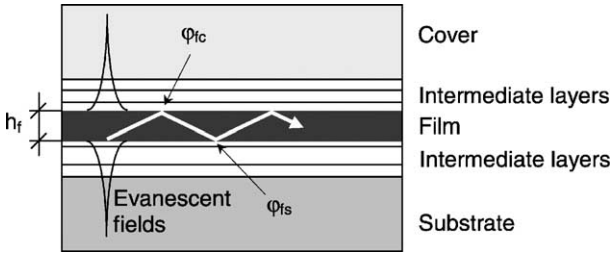

Fig. 1. Multi-layer waveguide.

without scattering. The mode propagates through total internal reflection inside the layer with the highest index of refraction, the so-called film. If the index of refraction decreases to the outer side of the system—such as no secondary waveguides are created—the guided modes fulfill the mode equation:

$$2kh_f\sqrt{n_f^2 - N^2} + \varphi_{fc} + \varphi_{fs} = 2\pi m \tag{1}$$

where h_f is the film height, n_f the film refractive index, N the effective refractive index of the waveguide, k the wave number, φ_{fc} the Fresnel reflection phase shift at top film interface, φ_{fs} the Fresnel reflection phase shift at bottom film interface and m the mode number.

In the case of a monomode waveguide, the right side of the equation reduces to zero.

The waveguide's effective refractive index N is directly proportional to the propagation constant of the mode. It is polarization dependent, as the Fresnel reflection phase shifts φ_{fc} and φ_{fs} differ for TE and TM waves.

In principle, the model only applies to unstructured interfaces. It can be used as an approximation to structured surfaces such as gratings when the grating depth h_g is small compared to the film thickness h_f. In this 'thin grating' approximation, the film height h_f does not correspond to the physical film thickness and is referred to as equivalent height. The model can be nevertheless expanded for structured interfaces by introducing additional layers with an averaged index of refraction [15].

2.1.2. Grating coupler

Light can be coupled into or out of a waveguide by means of a grating. A plane wave incident on the grating is partially diffracted into the guided mode. Maximum coupling efficiency is achieved at the resonance condition

$$n_a \sin\theta_{in} = N - \frac{m_g \lambda_r}{\Lambda} \tag{2}$$

where n_a is the ambient medium in which θ is measured, θ_{in} the angle of incidence of the plane wave, m_g the diffraction order, λ_r the resonance wavelength in the ambient medium and Λ the grating period.

2.1.3. Waveguide and grating of finite length

Both the models for waveguide and grating assume structures of infinite extent in the direction of propagation of the mode. A finite structure shows broadened resonances instead of discrete modes and coupling conditions. While the point of maximum coupling can be determined by Eqs. (1) and (2), width and shape of the resonance curve have to be determined with other models.

The effective index spread ΔN corresponding to a finite structure is derived in [16], Eq. (21):

$$\Delta N = \frac{\lambda}{L_g} \tag{3}$$

where L_g is the effective grating length.

The wavelength spread $\Delta\lambda$ in the case of a wavelength scan is given by:

$$\Delta\lambda = \Delta N\left(\frac{dN}{d\lambda}\right)^{-1} = \frac{\lambda}{L}\left(\frac{dN}{d\lambda}\right)^{-1} \tag{4}$$

where $dN/d\lambda$ is the effective index dispersion, given in [17].

The shape of the resonance curve $\eta = f(\lambda)$ of a finite grating can be approximated by a Lorentzian of center λ_r and halfwidth $\Delta\lambda/2$ [18].

2.2. Sensing principle

The wavelength interrogated optical sensor (WIOS) approach is based on scanning the resonance peak of a grating coupler by means of a current tunable laser diode.

The sensor chip is based on a monomode waveguide that is structured with two corrugated grating regions. The first one acts as incoupling pad for the incident beam, and the second grating for coupling light out of the waveguide onto a detector. When a guided mode is excited inside the waveguide, its evanescent field penetrates into the layers adjacent to the film. Changes of the optical properties in this region affect the phase shift φ_{fc} upon Fresnel reflection. The effective refractive index N of the waveguide mode changes accordingly (cf. Eq. (1)). The change in effective refractive index is monitored by observing the resonance peak of the incoupling grating (Eq. (2)).

In a classical readout scheme for a bio-chemical sensor based on waveguides and gratings, the resonance angle is scanned with a laser source of fixed wavelength [3]. In the wavelength interrogation approach, the resonance is scanned by observing the resonance wavelength at a fixed angle of incidence.

The sensing principle applies to two measurement configurations, namely (a) bulk refractive index sensing (refractive index of the cover medium n_c, Fig. 2a) and (b) measuring thickness h_l and/or refractive index n_l changes of a (bio-chemical) adlayer at the waveguide surface (Fig. 2b). Knowing the waveguide parameters, the measurand can be calculated from the relations (1) and (2).

The limited wavelength tuning range of the laser source results in a limited measurement range, tight fabrication

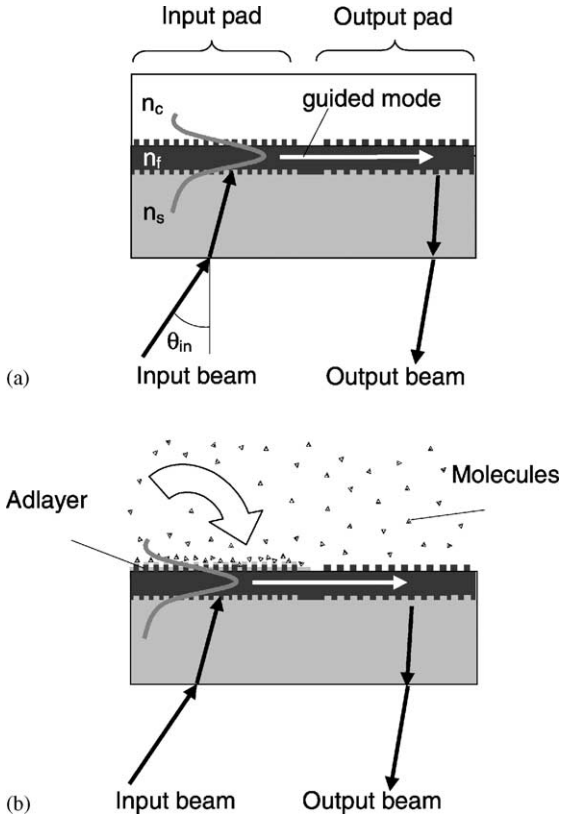

Fig. 2. (a) Bulk refractive index sensing. (b) Bio-chemical adlayer sensing.

tolerances for the sensor chips, and severe stabilization criteria. To overcome these limitations, an additional degree of freedom is introduced by adjusting the angle of incidence. Using a motorized mirror construction to set the working point introduces also the advantage of being able to perform an in situ chip calibration as described in Section 4.4

2.3. Optical scheme

The optical scheme is depicted in Fig. 3. A vertical cavity surface emitting laser diode (VCSEL) with a saw-tooth wavelength modulation is used as laser source. The collimated beam of the VCSEL is directed by a mirror towards the input pad of the chip. The mirror is used to adjust the incidence angle. At the resonance wavelength, a fraction of the light is coupled into the waveguide and coupled out through the output pad. The emitted light is collected by a multi-mode fiber and detected by a photodiode. The signal can then be acquired for peak position detection.

3. Design considerations

3.1. Substrate

For highly sensitive sensor applications, the mechanical and chemical stability of the sensor chips is of great importance. For this reason, high quality glass substrates are clearly preferred over polymers. A tradeoff is the augmented fabrication cost due to the nanostructuring of the grating, as convenient replication techniques such as hot-embossing [14] can no longer be used.

3.2. Film thickness and sensitivity

The thickness of the waveguiding film h_f is an important design parameter for adjusting the sensitivity for different measurands. Depending on the application, a different film thickness has to be chosen for maximum sensitivity. In the present case, the sensor chips are optimized for protein adlayer thickness (h_l) variations. Table 1 gives an overview of the overall sensitivity $\delta\lambda/\delta M$ of the chips for different applications. The parameters used for the calculations were

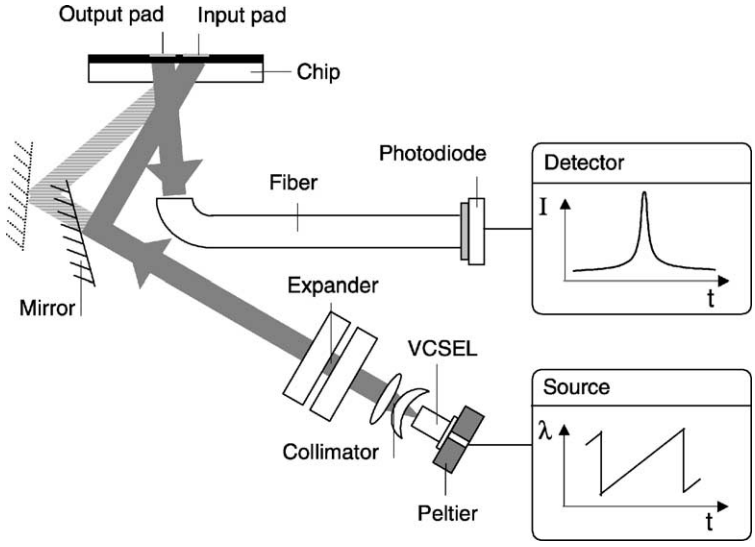

Fig. 3. WIOS optical scheme.

Table 1
Theoretical sensitivities for the WIOS system

Measurand	M	$\delta\lambda/\delta M$	Unit
Surface mass coverage	Γ	0.207	nm (mm^2/ng)
Adlayer thickness	h_l	0.122	nm/nm
Refractive index of adlayer	n_l	2.89	nm
Cover refractive index	n_c	72.8	nm

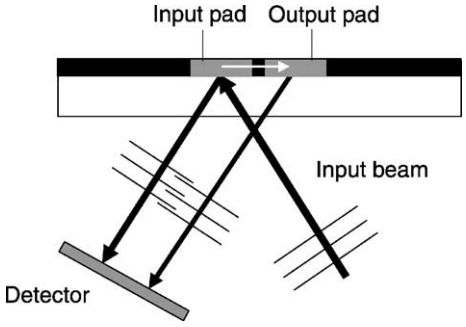

Fig. 4. Beam separation.

$n_c = 1.33$, $n_l = 1.45$, $h_l = 8.5$ nm, $n_f = 2.13$, $h_f = 150$ nm, $n_s = 1.52$, $\Lambda = 360$ nm, $\lambda = 763$ nm, TM_0. The surface mass coverage has been calculated as described in [19] with a surface coverage $\Gamma_m = 5$ ng/mm^2 corresponding to a saturated IgG monolayer of $h_l = 8.5$ nm adsorbed on a protein A layer.

3.3. Beam separation

If the input and output pads have the same coupling characteristics, reflections of the incident beam interfere with the outcoupled signal (Fig. 4). To prevent this, the in- and outcoupling angles have to be chosen differently. According to Eqs. (1) and (2), this can be achieved for instance by two gratings of different periods Λ_{in} and Λ_{out} (cf. Fig. 5a) or by two regions of same periods Λ but different film thicknesses $h_{f,in}$ $h_{f,out}$ [20] (cf. Fig. 5b). Both layouts have been fabricated, characterized and tested successfully in bio-chemical sensing applications.

3.4. On-chip referencing

In bio-chemical assays, a reference channel is used to separate specific from non-specific effects visible on the sensor response. These include changes of temperature and bulk refractive index, wavelength variations due to current instabilities of the laser diode, or non-specific binding [21,22]. The reference pad has the same characteristics as the sensing pad, but does not present the specificity of the sensing pad. During a measurement, the final signal is calculated by subtracting the reference peak position from the signal peak position.

Placing reference pads close to the sensing pads eliminates drift to a large extent, leading to much more relaxed stabilization criteria. Furthermore, it leads to a markedly increased signal to noise ratio, and therefore to a better detection limit.

4. Signal shape and calibration

4.1. Influence of parasitic reflections

The resonance curve as sensor output is disturbed in particular by parasitic reflections at the top and bottom substrate interfaces. The twice-reflected input beam is coupled into the waveguide with a phase ϕ_2 different from the phase ϕ_1 of the original wave, as can be seen in Fig. 6. As the phase difference $\Delta\phi = \phi_2 - \phi_1$ changes with the wavelength, this leads to a sinusoidal modulation of the resonance curve and to a deformation of the resonance peaks (Fig. 7).

The phase shift $\Delta\phi = \phi_2 - \phi_1$ is calculated by comparing the doubly reflected wave with the one incident at the same spot, having traveled a longer distance in the air:

$$\Delta\phi = \frac{4\pi h_s n_s}{\lambda}\left(\frac{1}{\cos\theta_s} - \sin^2(\theta_s)\right) + \varphi_{sf} + \varphi_{sa} \tag{7}$$

where n_s is the index of refraction of the substrate, λ the wavelength in air, φ_{sf} the Fresnel phase shift at the substrate-film boundary, φ_{sa} the Fresnel phase shift at the substrate-air boundary.

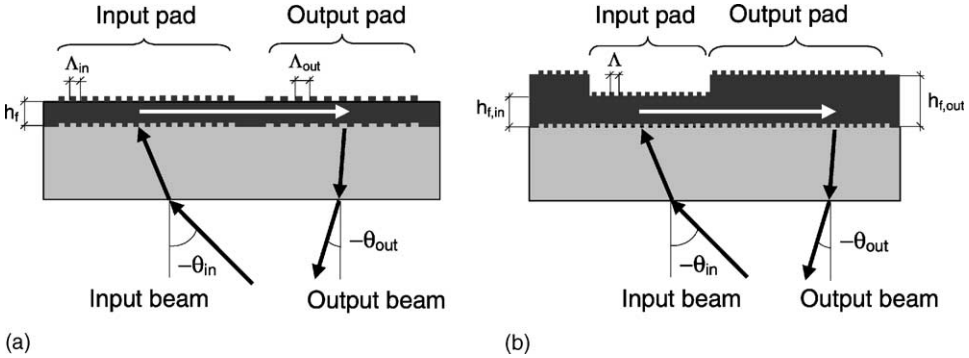

Fig. 5. (a) Cut through dual period sensor chip. (b) Cut through thickness-modulated sensor chip.

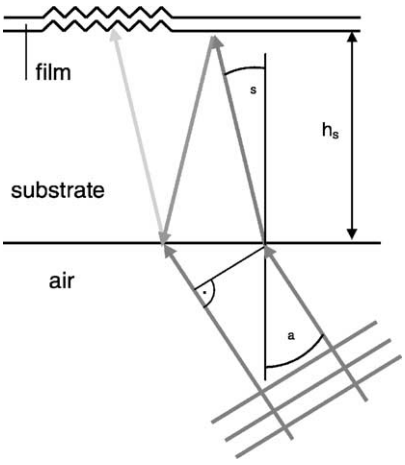

Fig. 6. Parasitic substrate reflections.

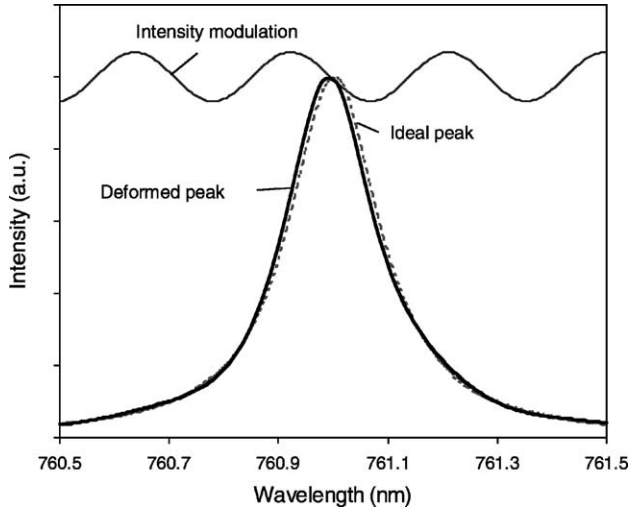

Fig. 7. Influence of parasitic substrate reflections on resonance peak shape.

The amplitude a_2 of the reflected wave is related to the amplitude a_1 of the original wave as

$$a_2 = a_1 r_{sf} r_{sa} \tag{8}$$

where r_{sf} the amplitude of the reflection coefficient at the substrate-film boundary, r_{sa} the amplitude of the reflection coefficient at the substrate-air boundary.

The intensity modulation I_{mod} of the signal corresponds to the interference term of the two waves. The impact on the signal peak shape is evaluated by expressing the modulation in terms of wavelength:

$$\frac{I_{bmod}}{I_1} = 2\frac{a_1 a_2}{a_1^2}\cos(\Delta\phi) = 2 r_{sf} r_{sa} \cos\left(\frac{\partial\Delta\phi}{\partial\lambda}\Delta\lambda\right) \tag{9}$$

where

$$\frac{\partial\Delta\phi}{\partial\lambda} = -\frac{4\pi h_s n_s}{\lambda^2}\left(\frac{1}{\cos\theta_s} - \sin^2(\theta_s)\right) + \frac{\partial\varphi_{sf}}{\partial\lambda} + \frac{\partial\varphi_{sa}}{\partial\lambda} \tag{10}$$

is the modulation frequency.

For a substrate of thickness $h_s = 0.7$ mm and refractive index $n_s = 1.52$, covered with a film of Ta_2O_5 ($h_f = 150$ nm, $n_f = 2.13$), with a grating structure of period $\Lambda = 360$ nm and illuminated with a laser source of wavelength $\lambda = 763$ nm, the resulting modulation has a relative intensity of 6.8% and a period of 0.29 nm (see Fig. 7).

4.2. Film thickness variations

If the film thickness is not constant over the whole input pad area, the resonance curve will get distorted. A different film height results in a different local propagation constant, and therefore to a different phase pickup between two adjacent grating lines. The peak broadens and its shape is altered depending on the film height profile. As the chips are optimized for maximum sensitivity to layer thickness changes, they are inevitably very sensitive to small film thickness variations.

This effect has been investigated in particular for thickness-modulated sensor chip layouts, where the etching step introduces height variations in the order of 0.5 nm. The resulting shoulder-like deformations are described in detail in [20].

4.3. Source characteristics

A current-tunable vertical cavity surface emitting laser (VCSEL) is chosen as the light source due to its compact size, low cost and high modulation frequency. The laser operates around a wavelength of 763 nm, with an accessible wavelength tuning range of about 2 nm. It has a nearly linear current–wavelength response, but output power depends also on the current. Fig. 8 shows the wavelength–power characteristics of the laser diode measured with a polarizer to select the mode polarization used for incoupling.

The resonance curve $\eta = f(\lambda)$ is deformed by the variation of the output power with the wavelength.

4.4. Calibration

The signal distortions and modulations mentioned under Sections 4.1–4.3 reduce the measurement accuracy if not properly taken into account.

In order to correct for the non-ideal peak shape, an in situ chip calibration procedure was developed.

As the incidence angle can be changed in the present set-up, the angle-resonance wavelength characteristic is recorded before the actual measurement. Therefore, the complete input angle range is scanned in small steps by the adjustable mirror (sketched in Fig. 3). For each step θ_k, several wavelength scans are averaged and the corresponding peak position $\lambda_{cal}(\theta_k)$ extracted. These data points are interpolated, resulting in the continuous curve $\lambda_{cal}(\theta)$ and its inverse relation $\theta_{cal}(\lambda)$. A linear fit is then applied to the measured points, representing the linearized characteristics $\lambda_{lin}(\theta)$.

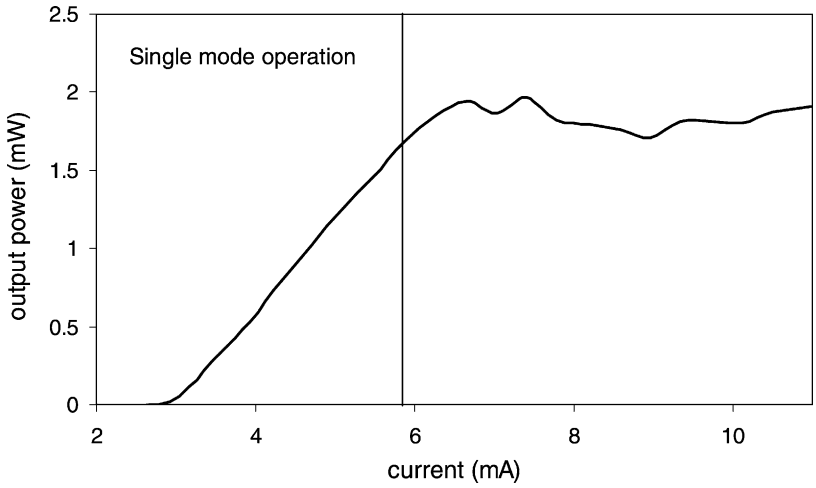

Fig. 8. VCSEL current–power characteristics.

During the actual measurement, the angle remains fixed and the wavelength scans are recorded over time. After the measurement, the measured peak positions λ_{meas} are corrected: $\lambda_{result} = \lambda_{lin}(\theta_{cal}(\lambda_{meas}))$.

For the calibration to work properly, it is necessary that both incoupling angle and effective refractive index follow a linear relation with the resonance wavelength. This condition is met inside the small measurement window.

5. Practical realization

5.1. Instrument

A compact WIOS instrument that has been realized is shown in Fig. 9. It allows the simultaneous readout of the resonance curves of four channels with a frequency of 300 Hz.

The following main components are visible on the photograph: (1) laser source, (2) beam expanding optics, (3) deflection mirror, (4) chip support with fluidic cell, and (5) array of plastic optical fibers.

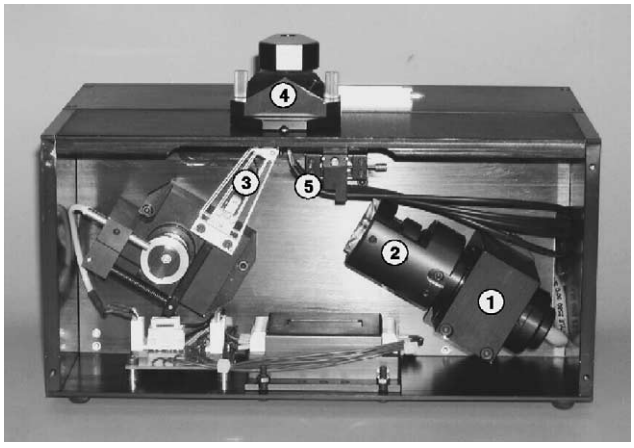

Fig. 9. Compact WIOS instrument. (1) Laser source, (2) beam expanding optics, (3) deflection mirror, (4) chip support with fluidic cell, and (5) array of plastic optical fibers.

As the light source, a VCSEL (Laser Components, SPECDILAS V-763-GMP) was used. The laser diode emits around a center wavelength of $\lambda = 763$ nm and has an accessible wavelength tuning range of about 2 nm. Its temperature is stabilized by a Peltier element, while the current is controlled by a custom electronic controller circuit. The deflection mirror has a range of 6° and is mounted on a motorized mechanical unit around the pivot axis located at the input grating. The output signal is detected by an array of photodiodes (OSRAM, SFH 206 K), amplified by a custom electronic circuit and acquired by a data acquisition board (National Instruments, PCI-6024E). The data is then treated on a personal computer.

5.2. Measurement procedure

Before starting the measurement, a proper angular working point is set. A reference cover medium (for example phosphate buffered saline solution PBS) is applied on the chip. The angular range is scanned by means of the motorized mirror. At the same time, calibration data (see Section 4.4) is collected. The mirror position then remains fixed in order to set the detected peak to a wanted starting position within the measurement range accessible by wavelength tuning. The actual measurement begins by removing the reference medium and applying the analyte. The peak positions of the reference and sensing pads are recorded over time. At the end of the measurement, the curves are corrected by applying the calibration and subtracting the reference from the sensing curve.

6. Sensor chips: fabrication

Two types of sensor chips have been realized as stated in Section 3.2. One layout consists of a waveguide structured

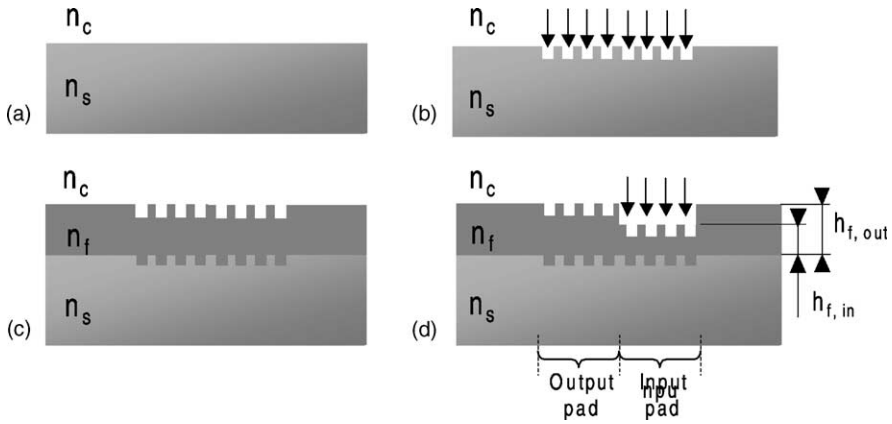

Fig. 10. Fabrication steps of depth-modulated sensor chips.

with two gratings of different period, defining the input and output pads. The other layout consists of a waveguide that is structured with a grating of uniform period, but presents two different film heights. The fabrication of the latter chip type is described in detail in the following.

For these so-called depth-modulated sensor chips, a fabrication process requiring only one holographic exposure has been established.

In Fig. 10, the main steps of the fabrication procedure are depicted. First, the surface of a 0.7 mm thick 4 in. AF45 glass wafer with a refractive index of $n_S = 1.52$ (at $\lambda = 632.8$ nm) was structured with a grating by holographic exposure (cf. Fig. 10a and b). In a second step, the grating structure was transferred into the substrate by dry etching as shown in Fig. 10b. During the etching, an aperture mask was applied to prevent gratings to be etched outside the input and output pad regions. The resulting grating had a period of $\Lambda = 360$ nm and a depth of $h_g = 13.2$ nm.

After removing the photoresist, the whole substrate was coated with a $h_{f,out} = 300$ nm thick Ta_2O_5 dielectric film using a low temperature DC magnetron sputtering process as shown in Fig. 10c. This process allows to fabricate thin, compact and homogeneous films with a high refractive index of $n_f = 2.10$ (at $\lambda = 632.8$ nm).

The structured substrate was coated with a second photoresist layer and the regions acting as input pads were exposed using an aperture mask. The film was then dry etched to a thickness of $h_{f,in} = 150$ nm as shown in Fig. 10d. While these regions acted as input pads, the regions remaining at the film thickness of $h_{f,out} = 300$ nm were used as output pads.

Finally the wafer was cut into single sensor chips of a size of 12.25 mm × 12.25 mm. Fig. 11 shows the picture of a sensor chip with six measuring channels. The dimensions of both the input and output pad were 0.8 mm × 1.0 mm. The triangular grating structure at the upper left corner is used as positioning reference.

A line-profile extracted from an AFM measurement of the transition region between input and output pad is plotted in Fig. 12. It shows that the transition width is less than one grating period. The measured step height was $\Delta h_f = h_{f,out} - h_{f,in} = 146.2$ nm. It can be seen on the graph that the grating height and profile is altered at the input pad region during the second etching step. The initial grating height of $h_g = 13.2$ nm is slightly reduced to $h_g = 12.7$ nm,

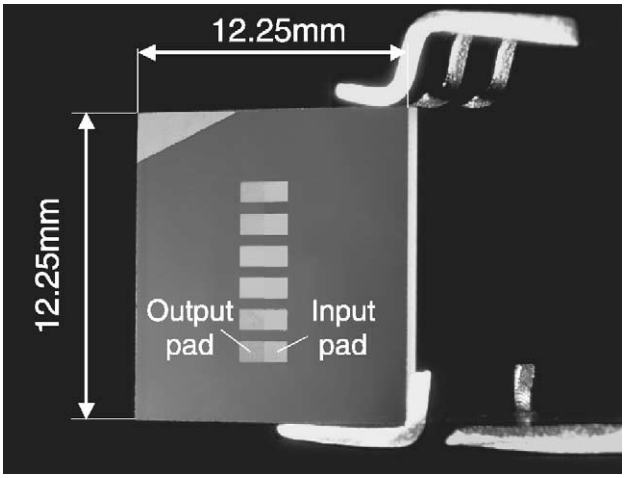

Fig. 11. Picture of the realized sensor chip with six channels.

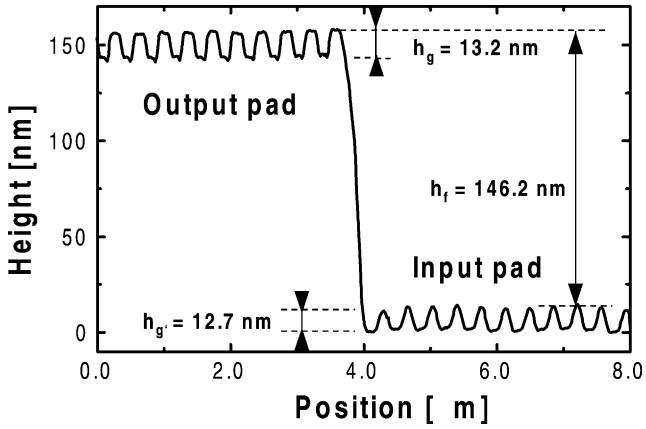

Fig. 12. AFM line profile of the transition between input and output region.

while the profile is changing from a trapezoidal to a smoother, more sinus like shape.

7. Applications

7.1. Bulk refractometry

Although the sensor chips were not optimized for refractometry of the cover medium (or bulk media in general), but for measuring thin adlayers formed near the waveguide's surface, refractometric measurements have been performed in order to evaluate the system sensitivity. For the series of measurements reported in Fig. 13, the following mixtures have been applied as the cover medium: 0.2, 1 and 5% glycerol in water, increasing the refractive index of the solutions by 0.00024, 0.0012 and 0.0058, respectively. The experiment was conducted by applying the solutions to the chip successively, always supplying water in between.

For this measurement, taking the raw data shown in Fig. 13 and determining the standard deviation of the signal over a time period of 1 min in a region with constant refractive index results in a value of 9.6×10^{-7} for the cover refractive index. This is the standard deviation for a single measuring pad, including drift and statistical fluctuations. If the signal of a reference pad is subtracted from the measuring pad signal (cf. Section 3.4), the standard deviation is reduced to 3.1×10^{-7}.

For obtaining a calibration, the measured shifts of the grating coupler resonance peak were compared with the shifts calculated using the known waveguide and grating parameters. The results confirmed the validity of all the system and chip parameters and were then used to obtain the relation between the resonance position and surface mass density of typical protein layers adsorbed on the waveguide grating.

7.2. Affinity measurements with small molecules

The most relevant applications for this system are in monitoring adsorption to and binding of molecules near the surface of the sensor chips. Many types of applications can be realized whenever a suitable recognition molecule–analyte couple exists. To demonstrate the performance of the system, the binding reaction of biotin on previously immobilized neutravidin was chosen. Using a double chamber fluid container, BSA and neutravidin were first adsorbed on two different channels of one waveguide chip, then biotin-5N-FITC with a molecular weight of 831 Da (cf. Fig. 14a) or pure biotin (cf. Fig. 14b) was supplied to both chambers simultaneously, the final concentration being 1 μg/ml. As the binding constant of biotin to neutravidin is high, the reaction takes place in a very short time (28 s) and drift due to the instrument or to the adsorbed layer is not significant. The binding of biotin can be clearly observed on the neutravidin coated pad whereas nothing occurs on the reference pad. The binding of biotin with a molecular weight of only 244 Da, one of the smallest molecules being of interest for biochemistry, is clearly demonstrated in Fig. 14b.

Examining the raw sensor signal data plotted in Fig. 14b yields a standard deviation of 0.009 peak position units for each pad, taken for 3 min in the steady regions, excluding the drift. The change of 0.613 units produced by adding the biotin solution is thus 67 times the standard deviation, corresponding to 22 times the detection limit. This indicates

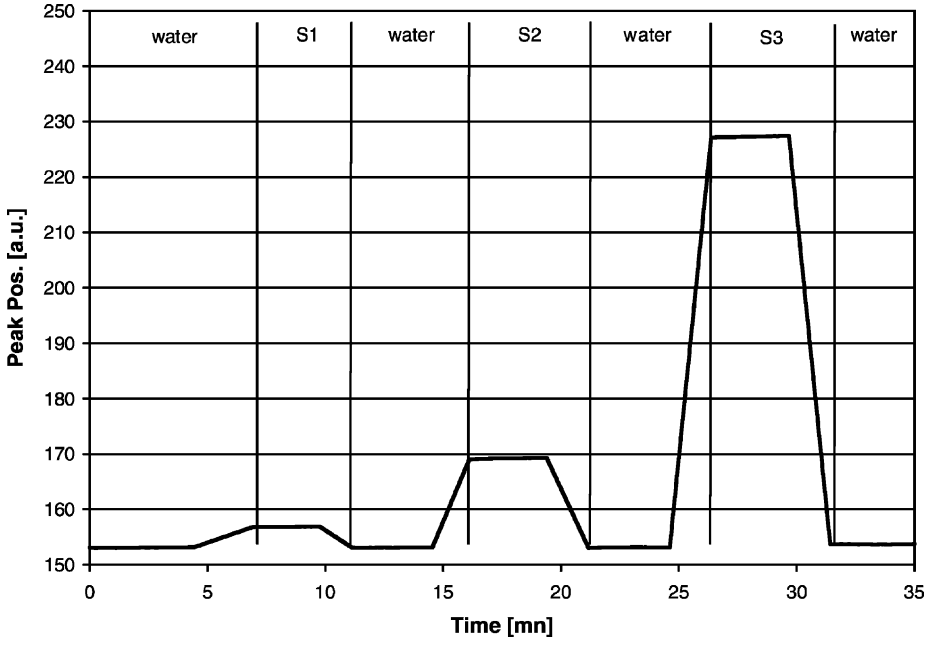

Fig. 13. Change of the resonance peak position for the three different refractive index solutions (water, *S*1: solution with $\Delta n = 0.00024$, *S*2 with $\Delta n = 0.0012$, and *S*3 with $\Delta n = 0.0058$).

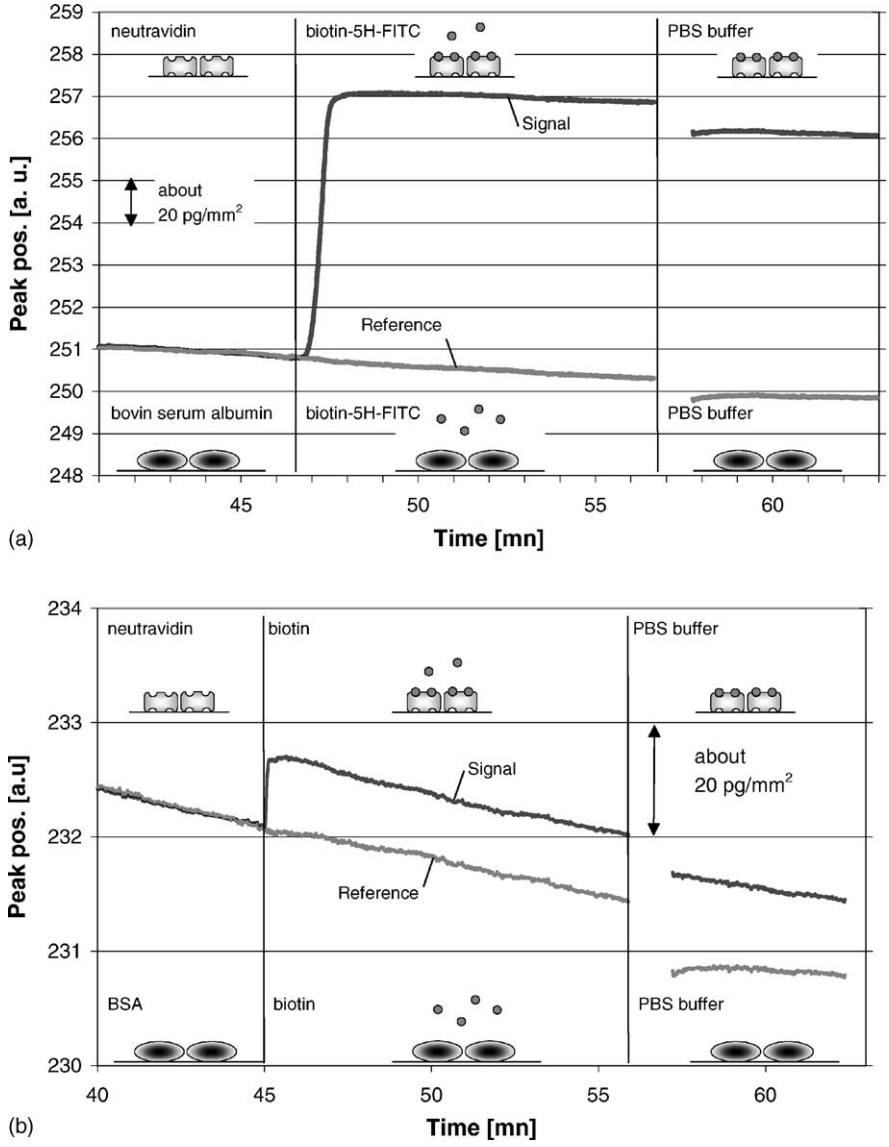

Fig. 14. Reaction of biotin-5H-FITC (a) and biotin (b) on adsorbed neutravidin (signal) and BSA (reference).

that the detection limit of the WIOS system is distinctly below 200 Da.

By making use of on-chip referencing (cf. Section 3.4), i.e. by subtracting the data of the reference from the signal curve (cf. Fig. 14b), the standard deviation is reduced to 0.005 peak position units, corresponding to about 100 fg/mm^2 and a detection limit of about 300 fg/mm^2. As in the case of bulk refractive index, this improvement is due to the fact that some signal disturbances originating for example from fluctuations in temperature and laser current, are affecting the signals from both pads in the same way.

7.3. Detection of large molecules at low concentration

Besides the detection of small molecules, the detection of larger molecules at low concentration is also an important feature for a biosensor. In order to show the performance of the WIOS approach for this type of application, we have chosen the reaction between anti-mouse antibody and mouse IgG. First, mouse IgG was immobilized on one grating pad using OptoDex® [23,24], i.e. a mixture of OptoDex® and mouse IgG (0.25 mg/ml each) were deposited on the pad. After drying, OptoDex® was activated with UV-light to induce the photobonding. The modified surfaces were then washed with phosphate buffered saline containing detergent (PBS/0.02% Tween 20) before being used in the system. A baseline was first established by supplying PBS–BSA buffer solution to the sensor cell, and then the buffer was replaced with solutions of anti-mouse IgG with decreasing concentrations of 10^{-10}, 10^{-9}, 10^{-8} M. The result of the measurement is shown in Fig. 15. It was made by pipetting without flow and without stirring. After 25 min of reaction the signal obtained with the lowest concentration is 0.26 units of peak shift, which is about five times the detection limit that can be

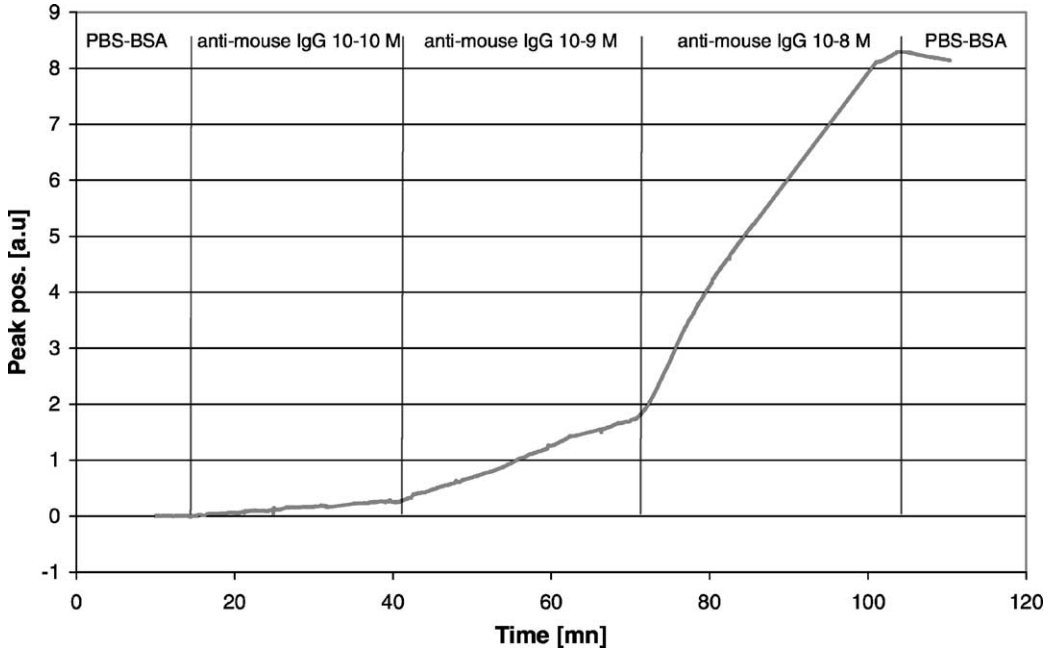

Fig. 15. Sensor signal upon the reaction of different concentrations of anti-mouse IgG supplied to the pad with immobilized mouse IgG (photobonded with OptoDex®). The reference was a bovine serum albumine coated pad.

obtained taking into account the drift of the instrument over the measurement time. A detection limit of 2×10^{-11} M can be expected for the same measurement conditions.

Considering the fact that the assay used was a direct immunoassay with photocoupled antigen, this is a very good result, especially if compared to sandwich assays. Further improvements can be achieved by making use of microfluidics and more sophisticated assays.

8. Conclusions

The WIOS bio-chemical sensor system based on wavelength interrogation of a waveguide grating has been presented. The label-free sensor combines fast readout with high sensitivity and accuracy. Some important design aspects have been pointed out, and sources of parasitic effects influencing the resonance peak shape have been identified and analyzed in detail. It has been shown that the use of a motorized deflection mirror allows calibrating the system in order to correct for these effects. The same mirror is used for setting the high-resolution measurement window within a large operating range.

The layout of two types of sensor chips has been presented together with fabrication details. The stability of the sensor chips has been enhanced by using glass rather than polymer substrates.

An excellent performance of the sensor has been demonstrated for bulk refractometry and affinity measurements. The bulk refractometric measurements show a detection limit of $<10^{-6}$. For detecting small molecules, a standard deviation in terms of mass coverage of 100 fg/mm^2 has been obtained, corresponding to a detection limit of 0.3 pg/mm^2. Furthermore, the very clear signal observed for biotin (244 Da) indicates a detection limit for the present WIOS system distinctly below 200 Da. For a direct immunoassay at low concentrations, a detection limit in the order of 10^{-11} M was estimated based on the results reported in this paper. These results show that the sensor is perfectly suited for application areas such as medical, food and environmental.

Acknowledgements

We gratefully acknowledge the help of F. Crevoisier, E. Bernard and R. Ischer with respect to performing experiments as well as for building the instruments, and B. Hitz from Unaxis with respect to chip fabrication. We also thank the Swiss CTI foundation for partly funding this project.

References

[1] M. Wiki, R.E. Kunz, Wavelength-interrogated optical sensors for biochemical applications, Opt. Lett. 25–27 (2000) 463–465.
[2] R. Horváth, J. Vörös, R. Graf, G. Fricsovszky, M. Textor, L.R. Lindvold, N.D. Spencer, E. Papp, Effect of patterns and inhomogeneities on the surface of waveguides used for optical waveguide lightmode spectroscopy applications, Appl. Phys. B 72 (2001) 441–447.
[3] K. Tiefenthaler, W. Lukosz, Sensitivity of grating couplers as integrated-optical chemical sensors, J. Opt. Soc. Am. B 6 (2) (1989) 209–220.
[4] J. Dübendorfer, R.E. Kunz, G. Jobst, I. Moser, G. Urban, Integrated optical pH sensor using replicated chirped grating coupler sensor chips, Sens. Actuators B 50–53 (1998) 210–219.

[5] R. Heidemann, R. Kooyman, J. Greve, Performance of a highly sensitive optical waveguide Mach-Zehnder interferometer immunosensor, Sens. Actuators B 10 (1993) 209–217.
[6] A. Brandenburg, R. Krauter, C. Künzel, M. Stefan, H. Schulte, Interferometric sensor for detection of surface-bound bioreactions, Appl. Opt.-OT 39(34) 6396.
[7] A. Ymeti, J.S. Kanger, R. Wijn, P.V. Lambeck, J. Greve, Development of a multichannel integrated interferometer immunosensor, Sens. Actuators B 83 (2002) 1–7.
[8] K. Nagata, H. Handa (Eds.), Real-Time Analysis of Biomolecular Interactions: Applications of 2000, Springer, Verlag, 2000.
[9] R. Cush, J.M. Cronin, W.J. Stewart, C.H. Maule, J. Molloy, N.J. Goddard, The resonant mirror: a novel optical biosensor for direct sensing of biomolecular interactions. Part 1. Principle of operation and associated instrumentation, Biosens. Bioelectron. 8 (1993) 347–353.
[10] R. Tünnemann, M. Mehlmann, R.D. Süssmuth, B. Bühler, S. Pelzer, W. Wohlleben, H.P. Fiedler, K.H. Wiesmüller, G. Gauglitz, G. Jung, Optical biosensors. monitoring studies of glycopeptide antibiotic fermentation using white light interference, Anal. Chem. 73 (2001) 4313–4318.
[11] G. Ladam, P. Schaad, J.C. Voegel, P. Schaaf, G. Decher, F. Cuisinier, In situ determination of the structural properties of initially deposited polyelectrolyte multilayers, Langmuir 16 (2000) 1249–1255.
[12] D.S. Ballantine, R.M. White, S.J. Martin, A.J. Ricco, E.T. Zellers, G.C. Frye, H. Wohltjen, Acoustic Wave Sensors: Theory, Design, and Physico-Chemical Application, Academic Press, San Diego, 1997.
[13] F. Höök, M. Rodahl, J. Vörös, R. Kurrat, P. Böni, J.J. Ramsden, M. Textor, N.D. Spencer, P. Tengvall, J. Gold, B. Kasemo, A comparative study of protein adsorption on titanium oxide surfaces using in situ ellipsometry, optical waveguide lightmode spectroscopy, and the quartz crystal microbalance/dissipation, Coll. Surf. B: Biointerf. 24 (2002) 155–170.
[14] R.E. Kunz, J. Edlinger, P. Sixt, M.T. Gale, Replicated chirped waveguide gratings for optical sensing applications, Sens. Actuators A 47 (1995) 482–486.
[15] R.E. Kunz, J. Duebendorfer, R.H. Morf, Finite grating depth effects for integrated optical sensors with high sensitivity, Biosens. Bioelectron. 11 (1996) 653–667.
[16] R.E. Kunz, L.U. Kempen, Miniature integrated optical sensors, Proc. SPIE 2068 (1994) 69–86.
[17] R.E. Kunz, J. Duebendorfer, Miniature integrated optical wavelength analyzer chip, Opt. Lett. 20 (1995) 2300–2303.
[18] R.E. Kunz, J. Edlinger, B.J. Curtis, M.T. Gale, L.U. Kempen, H. Rudigier, H. Schütz, Grating couplers in tapered waveguides for integrated optical sensing, Proc. SPIE 2068 (1994) 313–325.
[19] R.E. Kunz, G. Duveneck, M. Ehrat, Sensing pads for hybrid and monolithic integrated optical immunosensors, Proc. SPIE 2331 (1994) 2–17.
[20] K. Cottier, R.E. Kunz, G. Voirin, M. Wiki, Thickness-modulated waveguides for integrated optical sensing, Proc. SPIE 4616 (2002) 53–63.
[21] J. Dübendorfer, R.E. Kunz, Reference pads for miniature integrated optical sensors, Sens. Actuators B 38–39 (1997) 116–121.
[22] J. Dübendorfer, R.E. Kunz, E. Schürmann, G.L. Duveneck, M. Ehrat, Sensing and reference pads for integrated optical immunosensors, J. Biomed. Opt. 2 (1997) 391–400.
[23] I. Caelen, H. Gao, H. Sigrist, Protein density gradients on surfaces, Langmuir 18(7) 2463–2467.
[24] H. Sigrist, H. Gao, Biosensors @ CSEM, Chimia 53 (1999–2001) 81–86.

Biographies

Kaspar Cottier obtained the diploma (MSc degree) in microengineering with specialization in optics at the Swiss Federal Institute of Technology at Lausanne (EPFL) in February 2001. He is currently working on his PhD thesis at CSEM Neuchâtel (Switzerland) on integrated optical sensing, supervised by Rino E. Kunz.

Max Wiki studied physics from November 1991 until November 1996 at the Swiss Federal Institute of Technology (ETH) at Zurich. He finished his studies (MSc degree) with the master work entitled "Photorefractive Solitons in $KNbO_3$" at the Institute for Quantum Electronics of Prof. Dr. P. Günther. From 1996 until August 2000 he has worked at the CSEM Centre Suisse d'Electronique et de Microtechnique in Zurich on his PhD thesis on the topic of miniature integrated optical sensors systems based on disposable sensor chips, supervised by Dr. R.E. Kunz, Prof. Dr. R. Salathé (Swiss Federal Institute of Technology (EPFL) at Lausanne). In September 2000 he joined the R&D department of Unaxis Balzers Ltd. in Liechtenstein, where he is working on the design of BioChip substrates and the development of new technologies for the mass production of gratings and waveguides for biosensor applications.

Guy Voirin received his engineer diploma in physics in 1982 at ENSIEG in Grenoble, France. Then from 1982 to 1984 he carried out research on integrated optics on glass at the Institut Nationale Polytechnique de Grenoble where he received his PhD. After working at Radiall, Rosny-sous Bois, France, on the development of miniature fiber optical connector, he moved on in 1986 to CSEM, Neuchatel, Switzerland as a research and development engineer. He was involved in integrated optic technology on glass and on silicon and in the development of optical sensor for metrology. He is now involved in the development of optical biosensors. His expertise is on waveguide, waveguide sensor, grating couplers, interferometry, displacement measurement systems, evanescent wave sensing.

Hui Gao received her BS and MS degrees in chemistry from Nankai University, China, in 1985 and 1990, respectively. She received her PhD in biochemistry from the University of Bern, Switzerland, in 1994. Currently she is working in the field of surface bioengineering, which centre on photolink polymer-mediated immobilization of biomolecules on material surfaces and application in biosensor technology, biochips manufacturing and biomaterial.

Rino E. Kunz received his Matura (BA degree) from Gymnasium Winterthur, Switzerland, in 1965, and the diploma in physics (MS degree) from the Swiss Federal Institute of Technology (ETH) Zurich in 1971. Subsequently, he joined the Professur fuer Optik at ETH as a research and teaching assistant working in the field of physical optics. After having completed his PhD thesis on "Lifetimes of fluorescent molecules close to dielectric interfaces" in 1979, he enjoyed an IBM World Trade Postdoctoral Fellowship at IBM Research Laboratory in San Jose, California, USA, working on surface enhanced Raman scattering and elastic light scattering from metallic surfaces. From 1982 to 1987 he worked in the central R&D Optics Group of GRETAG Ltd., Regensdorf, in the fields of industrial laser materials processing, thin film design and photofinishing equipment design. He then joined the Optics Group at the Paul Scherrer Institute (PSI), Zurich, Switzerland, the emphasis of his work being on leading industry-related projects and PhD thesis supervising. Since 1997, his employment is with the Centre Suisse d'Electronique et de Microtechnique SA (CSEM), Zurich, holding a position of senior expert in the field of integrated optical sensing. Current research activities include integrated optical sensors, diffractive micro- and nano-relief structures, optoelectronic micro-systems and thin films. He teaches integrated optics at the Swiss Federal Institute of Technology Lausanne (EPFL) and is a member of the Optical Society of America (OSA), the Swiss Physical Society (SPG), the Swiss Society for Sensor Technology (SVS) and the Swiss Society for Optics and Microscopy (SSOM).

Appendix B

Thickness-modulated waveguides for integrated optical sensing

K. Cottier, R.E. Kunz, G. Voirin, M. Wiki

Published in Proc. SPIE Vol. 4616, p. 53-63, 2002

Thickness-modulated waveguides for integrated optical sensing

Kaspar Cottier [a], Rino E. Kunz [a], Guy Voirin [a], Max Wiki [b]
[a] CSEM SA, Jacquet-Droz 1, CH-2000 Neuchâtel, Switzerland
[b] UNAXIS Balzers Ltd., P.O. Box 1000, 9496 Balzers, Liechtenstein

ABSTRACT

Novel sensor chips for evanescent wave sensing have been developed and investigated for various (bio-) chemical applications. A preferred integrated optical sensing scheme requires an array of independent sensing pads being present on the chip, each one of them having two different regions for in- and out coupling of the optical readout beam. We present a novel chip type, where this goal is achieved by thickness variations of the waveguiding film and one single grating period. The sensor chips consisted of a 300 nm thick Ta_2O_5 waveguide deposited on a glass substrate structured with a uniform grating of 360 nm period. By this optical structure a first coupling angle was defined. Sensing pads with a different coupling angle were realized by etching the film at selected regions down to a thickness of about 150 nm. The performance of the novel chips was demonstrated in various refractometric sensing applications. The experiments included cover medium refractive index variation as well as monitoring of affinity binding of small molecules. A very high resolution of $3x10^{-8}$ in the effective refractive index was achieved. The emphasis of this paper is on describing this approach and on presenting optical chip characterization methods together with modeling results.

Keywords: (Bio-)chemical sensors, Evanescent-wave sensors, Integrated optical sensor chip, Optical chip characterization

1. INTRODUCTION

Integrated Optical (IO) Sensing schemes using gratings in demanding (bio-) chemical sensing tasks have numerous advantages over other methods. In particular, high sensitivity, small size and low cost can be mentioned[1]. The measurement principle consists in coupling light from a laser source into a waveguide by means of a grating. Every change at the waveguide surface affects the grating's resonance condition and can be measured with very high sensitivity. In the past, the resonance has been scanned for instance by varying the incoupling angle[2] or by chirped gratings[3].

Recently, a new generation of robust and highly sensitive wavelength interrogated optical sensor instruments (WIOS[4]) has been developed. Here, the resonance condition is scanned by varying the wavelength of a VCSEL source. With these instruments, the demand for disposable high performance yet low cost sensor platforms ("opto-chips"), arises. These opto-chips consist of a planar waveguide with an array of sensing and reference pads on a substrate with a surface of typically ¼ square inch.

While polymer substrates have proved their advantages in mass production by replication[5,6], the mechanical and chemical stability of glass substrates make them the first choice for IO (bio-) chemical sensor platforms. New opto-chip designs for glass substrates have to be investigated in order to facilitate mass production.

The present paper presents a novel chip design with reduced fabrication cost. In section 2, the fundamentals of IO sensing using waveguides and gratings are recalled, and the working principle of the depth-modulated chip design is presented. Section 3 gives detailed information about the fabrication process used. In section 4, optical chip characterization methods are presented together with experimental results. Section 5 contains an attempt to explain the experimental results and model chip behavior.

Optical Fibers and Sensors for Medical Applications II, Israel Gannot, Editor,
Proceedings of SPIE Vol. 4616 (2002) © 2002 SPIE ·1605-7422/02/$15.00

2. FUNDAMENTALS AND WORKING PRINCIPLE

Waveguides and grating couplers are treated in detail in [7] and [8]. A formulation of these principles applied to bio-chemical sensing can be found in [9]. The main theoretical aspects will be summarized in the following sections for convenience reason.

2.1 Waveguide

A basic planar dielectric waveguide as shown in Figure 1(a) is composed of 3 layers: substrate, film and cover. The layers are supposed absorption free and without scattering. The refractive index of the film is assumed to be higher than both the substrate and the cover refractive index, permitting total internal reflection at the film interfaces.
For a mode to be guided inside the film, it has to satisfy the mode equation:

$$2kh_f\sqrt{n_f^{\,2}-N^2}+\varphi_{fc}+\varphi_{fs}=2\pi m \qquad (1)$$

where:

N:	effective refractive index of the waveguide
k:	wave number
φ_{fc}:	Fresnel reflection phase at film-cover interface
φ_{fs}:	Fresnel reflection phase at film-substrate interface
m:	Mode number

The waveguide's effective refractive index N expresses the phase velocity vp in the direction of propagation of the mode:

$$v_p = c/N \qquad (2)$$

Note that the reflection phases are different for TE and TM polarization, the corresponding phase velocity (or effective refractive index) therefore also being different.
The simple layer model is an approximation to the case encountered in IO sensing, where one or both interfaces are structured with a grating showing a grating depth $h_g << h_f$. The approximation is often referred to as thin-film approximation.

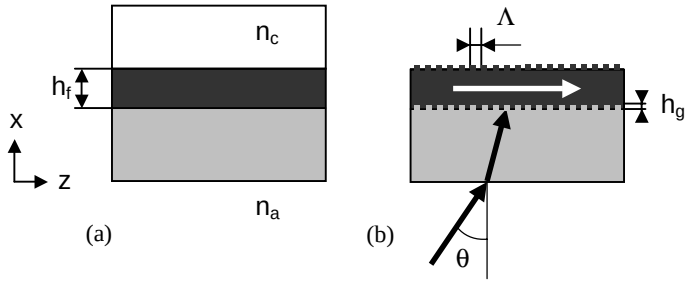

Fig. 1: Waveguide (a) and grating coupler (b)

2.2 Grating coupler

The role of a grating is to couple light from or to a waveguide (Figure 1(b)). Supposing a plane wave being coupled into a waveguide by means of a diffraction grating, maximum coupling efficiency is achieved at the resonance condition

$$n_a \cdot \sin\theta = N\text{-}m_g\lambda/\Lambda \tag{3}$$

where:

- n_a: medium in which θ is measured
- θ: angle of incidence of the plane wave, measured in n_a
- m_g: diffraction order
- λ: free space wavelength
- Λ: grating period

Note that the grating period is usually smaller than the free-space wavelength. For an infinitely long grating, the discrete diffraction orders lead to discrete coupling angles θ_{mg} for a given wavelength, or to discrete coupling wavelengths λ_{mg} for a fixed incidence angle. A finite grating shows a broadened resonance peak. The corresponding effective index spread ΔN is derived in [3], eqn (21):

$$\Delta N = \lambda/L \tag{4}$$

where

- L: effective grating length

The angular spread Δθ for a fixed wavelength λ is given in [10], eqn (2):

$$\Delta\theta = \Delta N \cdot \left(\frac{dN}{d\theta}\right)^{-1} = \frac{\lambda}{L} \cdot (n_a \cdot \cos\theta_0)^{-1} \tag{5}$$

where

- θ_0: resonance angle

The wavelength spread Δλ in the case of a wavelength scan states:

$$\Delta\lambda = \Delta N \cdot \left(\frac{dN}{d\lambda}\right)^{-1} = \frac{\lambda}{L} \cdot \left(\frac{dN}{d\lambda}\right)^{-1} \tag{6}$$

where

- dN/dλ: effective index dispersion, given in [11]

The shape of the resonance curve of a finite grating for the case of an angular scan can be approximated by a Lorentzian[10].

2.3 Depth-modulated sensor platforms

The high sensitivity of the grating's coupling condition to effective refractive index changes allows highly sensitive sensor devices. Typically, cover (also called bulk) refractive index changes or adlayer height variations are to be sensed. Every variation at the film-cover interface of the waveguide translates into a change of the Fresnel reflection phase φ_{fc},

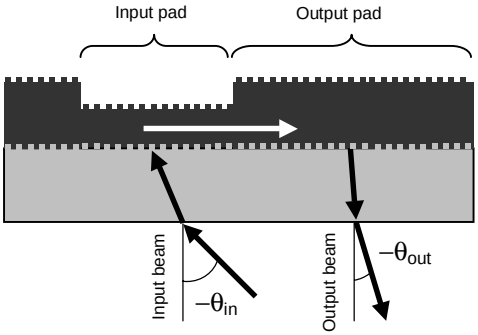

Fig. 2: Cut through depth modulated sensor chip

and therefore to a different effective refractive index N (eqn (1)). A shift of the grating's coupling condition is the consequence (eqn (2)).

A preferred layout for a sensor using depth-modulated chips is shown in Figure 2. The input pad acts as actual sensing pad. When its coupling condition at an angle θ_{in} is reached, light is diffracted into the waveguide. The output pad is used to direct a fraction of the guided wave onto a detector at an angle θ_{out}.

The reason for using two distinctly different angles is to spatially separate the reflected incident beam and the output signal in order to achieve a good signal to noise ratio (SNR). This is usually achieved by creating gratings of different period Λ_1 and Λ_2. In the depth-modulated approach, the resonance condition is altered by locally modifying the film thickness. Figure 2 shows a partial cut of this kind of chips. In the present example, the whole substrate is structured with the same grating of period Λ = 360nm. A waveguiding film of thickness h_{fo} = 300nm is deposited, and the input pads are selectively etched down to a different film height h_{fi} = 150nm.

The theoretical coupling angles for this geometry can be calculated from eqs (1) and (3) and are θ_1 = -29.9° and θ_2 = -13.4° (λ = 763nm, n_f = 2.13, n_s = 1.52, n_c = 1.33, TM_0).

2.4 Application to (Bio-)Chemical Sensors

To turn the sensor platform into a (bio-)chemical sensor, a biochemical sensing layer is applied on top of the waveguiding film. Its role is to attract specific molecules from the solution to analyze. If these molecules are present, they attach to the layer (Figure 3(a)). This translates into a shift of the coupling condition as described in section 2.3. A second grating pair with parameters equal to the first one, but without the sensing layer, acts as reference. Analyzing the difference of the two signals instead of only the sensing pad's response eliminates an important part of drift and fluctuation problems[12].

Different schemes for finding the resonance condition exist, each of them having their particular advantages and drawbacks. A setup first described in [2] consists of sweeping the angle of incidence. Another method is the use of chirped gratings, where the grating period changes over the sensor pad[3]. Recently, a new family of wavelength interrogated optical sensor (WIOS[4]) systems has been developed at CSEM. In this approach, the wavelength is continuously scanned by current tuning of a VCSEL. This readout scheme has proved its stability, accuracy and rapidity: the need for moving parts during a measurement is eliminated, and tuning frequencies in the range of kHz are easily achieved. However, it should be pointed out that in contrast to the other readout schemes described above, the scanned variable λ does not only figure in the resonance condition (eqn 3), but the effective refractive index N itself depends also on λ. A heavily non-linear behavior could be expected, but inside the small scan range (typically $\Delta\lambda$ = 2nm), a very linear response can be observed.

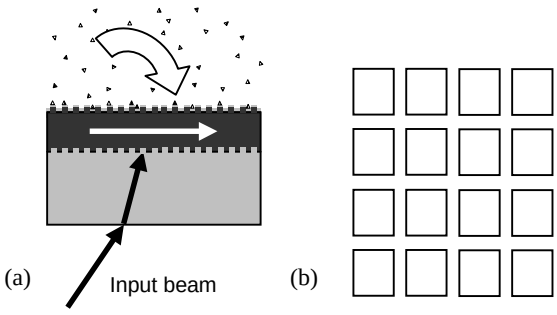

Fig. 3: (Bio-)chemical sensor layout

3. FABRICATION

For the fabrication of the depth-modulated sensor chips, a novel process requiring only one holographic exposure followed by one standard illumination procedure for defining the input and output grating pad structure has been established.

In Figure 4, the main steps of the fabrication procedure are depicted. At first, as shown in Figure 4(a), a 0.7 mm thick AF45 glass substrate with a refractive index of $n_s = 1.52$ (at $\lambda = 632.8$ nm) was structured over the whole chip surface area with a grating having a period of $\Lambda = 360$nm and a depth of $h_g = 13.2$ nm by using holographic exposure and dry etching techniques for transferring the structure into the high refractive index film (cf. Figure 4(b)).

After removing the remaining photoresist, the structured substrate was coated with a $h_{f,out} = 300$ nm thick Ta_2O_5 dielectric film using a low temperature DC magnetron sputtering process. This process allows to fabricate thin and compact films with a high refractive index of $n_f = 2.10$ (at $\lambda = 632.8$ nm).

Subsequently, the structured substrate was coated with a second photoresist layer. Using a mask aligner with a mask for defining the grating pad structure, the regions acting as input pads (IP) were exposed. The developed photoresist was used as mask for dry etching the film down to a thickness of $h_{f,in} = 153.8$ nm as shown in Figure 4(c). While these regions acted as input pads, the regions remaining at the film thickness of $h_{f,out} = 300$ nm were used as output pads P_{out}. Finally the photoresist covering the output pad (OP) was completely removed.

The quality of the resulting structure, especially of the gratings at the input and output pads and the etch depth was carefully investigated by AFM measurements (Digital Instruments) and optical methods (c.f. Section 4, Experimental). Figure 5(a) shows a 3-D view of a 10 µm x 10 µm surface-area, taken at the transition region from an input to an output pad. The thickness variation of the film as well as the grating structures are clearly visible.

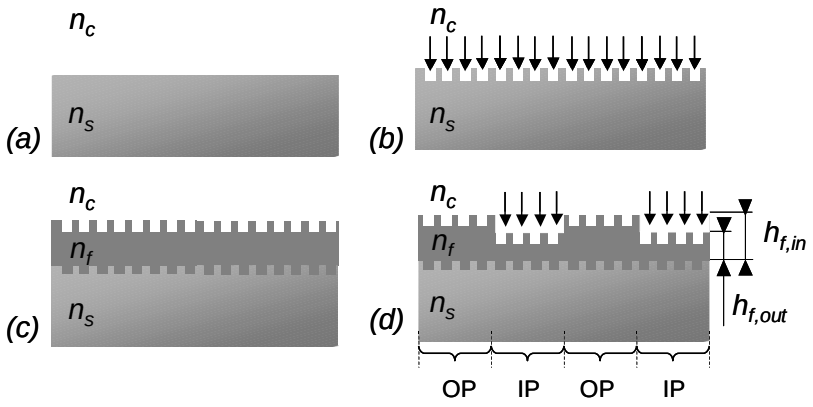

Fig. 4: Fabrication steps for depth-modulated sensor chips

An extracted line profile of this region is plotted in Figure 5(b). It clearly illustrates the accuracy of the step and shows that the transition region is less than the line width of one grating period. The measured step height was $\Delta h_f = h_{f,out} - h_{f,in} = 146.2$ nm. It can also be seen in the graph that the grating height and profile was altered at the input pad region during the second etching step. The initial grating height of $h_g = 13.2$ nm is slightly reduced to $h_g' = 12.7$ nm, while the profile is changing from a trapezoidal to a smoother, sinus like shape.

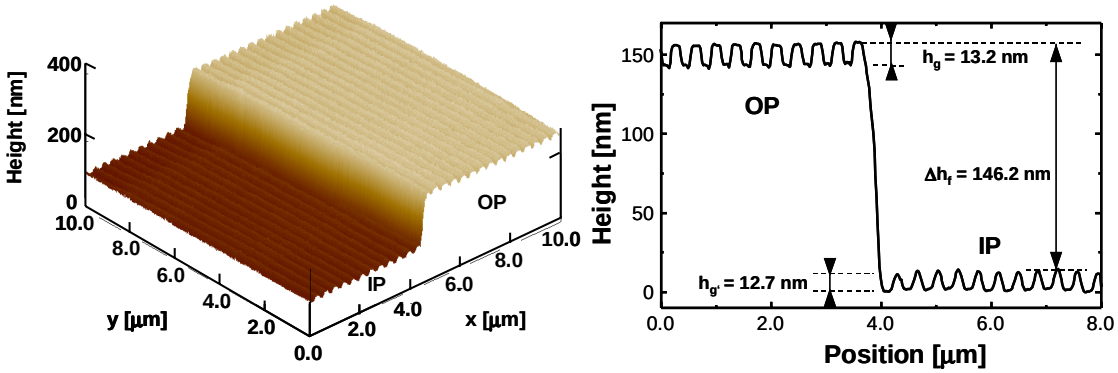

Fig. 5: AFM measurement of the transition between input and output region and corresponding line profile

4. EXPERIMENTAL RESULTS

4.1 Chip Testing

The goal of a first measurement series was to characterize the opto-chips. In order to verify the waveguide and grating parameters, the grating's resonance angles θ_0 for TE and TM mode at a given wavelength λ were determined. Knowing the grating period Λ and the parameters of substrate and cover, the film refractive index n_f and height h_f are calculated from θ_0 using equations (1) and (3). The grating period Λ is prior determined by optical measurements performed in the Littrow configuration[10].

The accuracy, with which the resonance peak position can be determined, depends on the shape of the resonance curve. To visualize this curve, the incoupled intensity η is plotted versus angle θ_{in} by performing an angular scan.

The measurements were performed using the setup seen in figure 6. A He-Ne laser source (λ = 632.8 nm) is used to illuminate the incoupling grating pad. The beam shape is controlled with a lens of large focal distance. The chip is placed in the center of rotation of a high resolution rotary table measuring θ_{in}. The wave excited inside the waveguiding film is partially diffracted by the outcoupling grating at an angle θ_{out}. The outcoupled beam is imaged through a lens on a photodiode measuring outcoupled optical power η. The surrounding medium is air (n_c = 1).

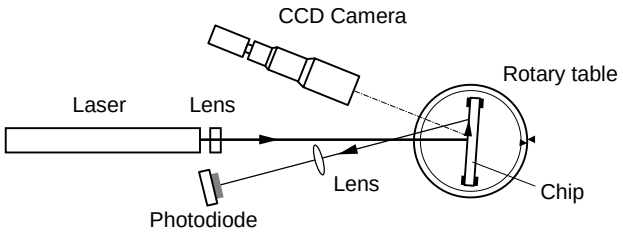

Fig. 6: Experimental set up for chip characterization

The resonance peaks for the incoupling grating were measured at $\theta_{in,TE}$ = 5.8°, $\theta_{in,TM}$ = -3.5° for TE and TM mode respectively. The outcoupling angles were determined by using the outcoupling region as incoupler and were $\theta_{out,TE}$ = 14.5°, $\theta_{out,TM}$ = 11.1°. The refractive index of the film and the film heights were calculated by solving equations (1) and (3) and are n_f = 2.13, $h_{f,in}$ = 173 nm $h_{f,out}$ = 309 nm. The figures for film height differ from the ones obtained by AFM measurements (section 3), as a different batch was analyzed.

To verify the resonance curve shape of the sensing pad, angular scans were performed using a spot covering the whole input grating pad. Figure 8(a) shows such a scan for the TM mode. The deformed resonance peak was observed for all pads that have been measured. In order to investigate the cause of this effect, further measurements had to be performed. Local coupling characteristics were obtained by illuminating only a fraction of the grating at a time.

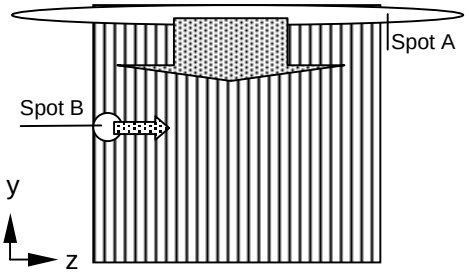

Fig. 7: Illustration of the different illumination spot shapes used for chip characterization.

A series of measurements with a line-shaped illumination as seen in Figure 7 (Spot A) were performed. The beam covered the whole pad in the direction of the z-axis having a width of approximately 75µm in y-direction. Scanning the signal shape at 11 equally distant positions along the y-axis of the pad permitted two observations. First, the resonance peak position changes significantly along the y-axis. Second, the signal shape, as seen in figure 8(b), differs both from the shoulder-type and the standard Lorentzian. An asymmetric interference pattern can be observed.

A last series of measurements was performed using a point illumination as seen in Figure 7 (Spot B). The beam diameter was approx. 100µm. Again, 11 scans were performed, at equidistant points along the z-axis in the center (y-axis) of the pad. The resonance curves obtained hereby were the first ones to follow the expected Lorentzian shape. The broadening of the resonance peak is a consequence of the partial illumination in z-direction, as the effective grating length is reduced (eqs (5) and (6)). As in the previous experiment along the y-axis of the pad, the resonance peak position changes along the z-axis.

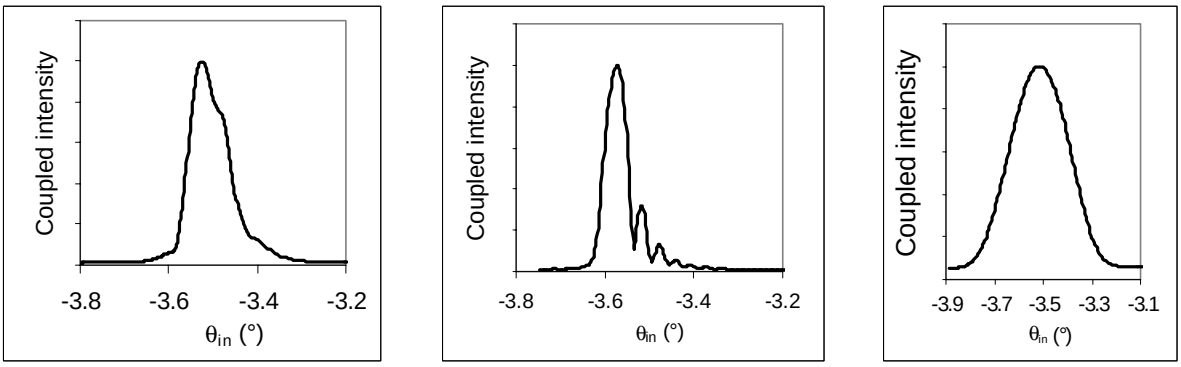

Fig. 8: Resonance curves obtained by angular scans with spot coveringthe whole incoupling pad (a), line-style illumination (b) and small spot (c)

4.2 Measuring Bulk refractive index

A refractometric measurement is a simple application example of the sensor chips. Variations of the index of refraction of the cover medium n_c are monitored using a wavelength interrogated optical sensor (WIOS[4]) instrument. In the previous experiments, the resonance was scanned by varying the incoupling angle θ_{in}, while the wavelength of the source λ remained fixed. In the WIOS instrument, λ is varied while maintaining the same θ_{in}. The main advantages of this sensing scheme are no moving parts and fast readout. A photograph of the WIOS breadboard and the corresponding schematic are shown in figure 9.

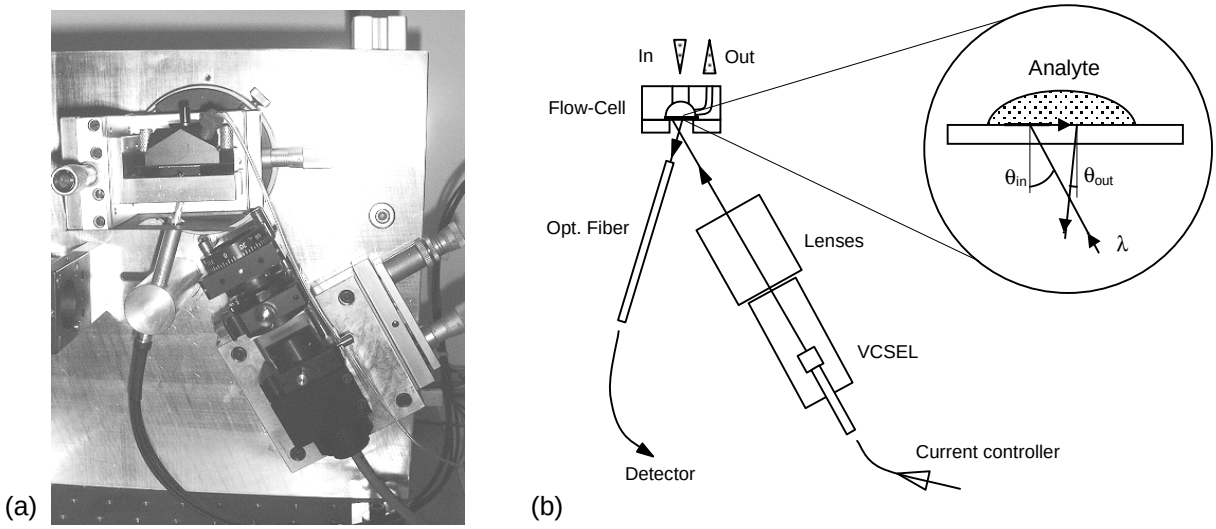

Fig. 9: WIOS breadboard (a) and corresponding schematic (b)

A current tunable ($\lambda = f(i)$) VCSEL laser source is used to illuminate the sensing pads. Collimating and expanding optics are used to produce an asymmetric spot, permitting the simultaneous readout of four channels. As mentioned above, the source is placed at a fixed angle θ_{in} with respect to the sensor chip. An optical fiber collects the light emitted by the outcoupling region at an angle θ_{out}. The resonance condition of the sensing pad is examined by plotting the outcoupled intensity as a function of wavelength $\eta = f(\lambda)$. A gaussian fitting is used for resonance peak detection. The VCSEL used is a laser components Specdilas V 763 GMP and has a current tuning range of about $\Delta\lambda = 2$ nm. The VCSEL is stabilized in temperature by a micro-peltier element.

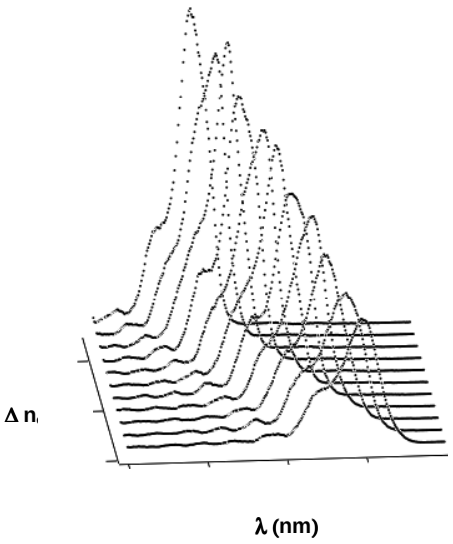

Fig. 10: Results from the Refractometric Measurements. Curves show coupled intensity versus wavelength for different cover refraction indices.

The performance of the chips was analyzed by applying liquids of known refractive index as cover medium. This was achieved using different concentrations of Glycerol 87% ($n = 1.454$) in Phosphate Buffered Saline solution (PBS, $n = 1.334$). The response of the chips to 11 Concentration steps corresponding to refractive index changes of $1.20 \cdot 10^{-3}$ has been monitored. The theoretical resonance peak wavelength shift $d\lambda/dn_c = 72$ nm can be calculated by solving eqs (1) and (3) numerically. This leads to a peak resonance shift of $d\lambda/dn_c \cdot \Delta n_c = 0.086$ nm per step. According to equation z, the expected FWHM is $\Delta\lambda = 0.24$ nm for the present configuration ($L_g = 1$ mm).

Figure 10 shows a series of wavelength scans $\eta = f(\lambda)|_{nc}$. The x axis corresponds to the wavelength λ, the y axis represents the refractive index change Δn_c with respect to 0% Glycerol.

The observed resonance shifts correspond well to the theoretical predictions. But again, signal deformations similar to the ones obtained in section 4.1 are observed.

4.3 Biosensor experiments

In order to show the performances of the chips, several experiments with biomolecules were prepared. The waveguide is first treated to receive the biomolecules: it is cleaned with detergent, rinsed and then treated to be more hydrophilic (microwave oxygen plasma or HCl overnight immersion). In a first set of experiments, mouse IgG was photobonded on the surface using OptoDex®. The Chip is then installed in the WIOS breadboard. The signal baseline is established with pure buffer on top of the waveguide, then different concentrations of anti-mouse antibody solution are applied. The binding of the molecules is monitored with the record of the wavelength resonance position versus time. In a second set of experiments, neutravidin and Bovin Serum Albumin (BSA) are first adsorbed on the cleaned waveguide surface directly on the WIOS breadboard (adsorption is also monitored). Neutravidin and BSA are adsorbed on different grating pads. After adsorption, the baseline is established with buffer, when biotin is added (final concentration 1 μg/ml), only the neutravidin pad reacts as it is expected (neutravidin is a biotin binding protein). The WIOS breadboard with the depth-modulated chips is well adapted for surface binding monitoring of molecules and can be used for large (antibody 150000 Dalton) and small molecules (biotin 244 Dalton). With a reference pad, a resolution of $3\ 10^{-8}$ on the effective refractive index can be achieved, this is equivalent to a surface density of about 100 fg/mm^2 of protein on the waveguide grating pad.

5. MODELING AND DISCUSSION OF RESULTS

In this section, an attempt to explain the unusual signal shape observed during the various experiments conducted with the depth-modulated chips is given. In the application of the chips to (bio-) chemical sensing, the shoulder-like deformation is of major concern. The peak resonance λ_0 in a wavelength scan, or θ_0 in an angular scan is the actually measured figure. If the peak resonance is not well defined, the precision of the measurement suffers accordingly.

A possible explanation of the signal deformation is a variation of the effective refractive index N inside the grating pad. In our case, due to the fabrication process, the most likely cause for a non-uniform N distribution are film height variations. As the chip is designed to be very sensitive to sensing layer height differences at the film-cover surface, it is inevitably very sensitive as well to changes of the actual film height. A first estimation using eqs (1) and (3) leads to a sensitivity in terms of resonance wavelength of $d\lambda_0/dh_f = 0.65$ nm/nm (nc = 1.33). This figure confirms the sensitivity of the chip to film height differences.

With the hypothesis of effective refractive index (N) changes due to height differences inside the grating pad, the various resonance curves obtained in section 4.1 can be used to determine equivalent height profiles. This profile is established by first determining the local peak resonance angles, and then solving eqs (1) and (3) for the film height h_f. As the model is an approximation of the reality assuming an infinitely thin grating, this equivalent height does not correspond to the actual film height.

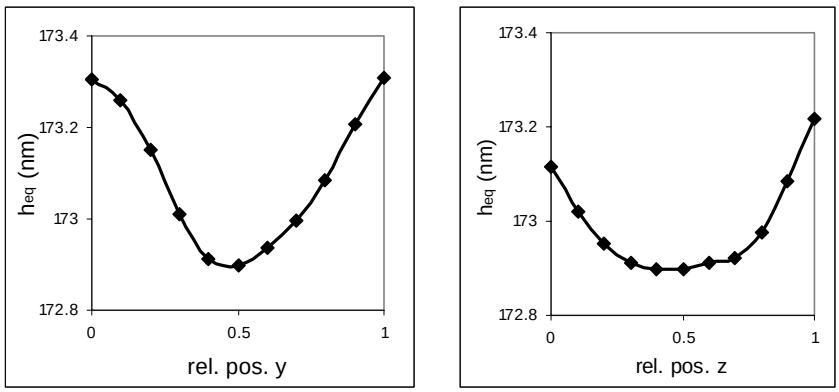

Fig. 11: Equivalent height profile reconstructed from the local coupling angles determined during chip characterization. (a) Shows the distribution for line-style illumination along y, (b) the central profile along z

The equivalent height profiles for the y-axis and z-axis have been established using the experimental

data of the corresponding scans obtained in section 4.1. Figure 11 shows the two distributions. The resolution of the reconstructed equivalent height can be estimated by calculating the angular sensitivity to height differences. A sensitivity of $d\theta/dh_f = 0.156$ °/nm can be calculated from eqs (1) and (3). Supposing that the resonance angle can be determined with a resolution of $\Delta\theta<0.01°$, a surprising theoretical resolution of $\Delta h_f = \Delta\theta/(d\theta/dh_f) = 0.06$ nm in terms of height difference is achieved.

The goal of a further investigation of this model was a simulation of the effect of arbitrary height distributions on the resonance profile $\eta = f(\lambda)$ based on eqs (1),(3),(4) and (5). This corresponds to the inverse calculation of what has been done to reconstruct the height profiles. When trying to model the observed signal, it becomes quickly clear that a key element for successful simulation is the explanation of the signal shape plotted in figure 8(b), resulting from a line- type illumination.

While the measurements along the y-axis of the pad sum up to a curve very close to the signal observed when illuminating the whole pad, the same statement cannot be made for curves along the z-axis. A simplified explanation of this phenomenon is that the light coupled into the waveguide propagates in z-direction, not interfering with waves coupled at a different y position. But light coupled at a certain z coordinate does interfere with light coupled at another position of same y but different z coordinate. Further investigations and simulations on this subject are being performed and are to be published elsewhere.

CONCLUSION

Depth-modulated chips have been designed and fabricated. The chips consist of a uniform grating covering the whole chip area, while sensing pads with different coupling conditions are introduced by locally reducing the film thickness. The chips have been characterized with angular scans and have been successfully tested in refractometric measurement using wavelength interrogated optical sensor (WIOS). The goal of angular separation of the reflection of the incoming beam and the outcoupled light has been achieved. The shape of the resonance curve presented the particularity of a shoulder-like deformation. The cause of this effect has been investigated, and it was found that effective refractive index (N) variations inside the sensing pad could explain this deformation. The N changes are most likely introduced by height variations resulting from the local etching step. As the chips are designed to be sensitive to sensing layer height changes in bio-chemical measurements, they are as well sensitive to film thickness variations.

A highly sensitive method was presented to measure N profiles inside the grating pad. By assuming that the effective refractive index (N) variations are caused by height changes, an equivalent height profile can be established with a resolution of $\Delta h_{eq}<0.1$ nm.

A better understanding of the origin of the resonance shape is of importance for two reasons. First, optimization of fabrication parameters could be achieved. Second, the peak detection algorithm used on the WIOS instrument for bio-chemical sensing could be improved in order to be less sensitive to deformed signals. Therefore, further investigations are and will be performed.

Depth-modulation is an interesting method to produce IO sensor platform chips at lower cost. High sensitivity measurements are nevertheless restricted due to the particular signal shape, making resonance condition detection difficult.

ACKNOWLEDGEMENTS

We gratefully thank François Crevoisier for his help on chip pretreatment and for performing measurements, Eric Bernard for his work on the WIOS breadboard and Réal Ischer for his contribution to the readout electronics. Acknowledgement is also made to the Swiss “Kommission für Technologie und Innovation (KTI)”, Project Number 5165.2, for partially supporting this work.

REFERENCES

1. R.E. Kunz, "Integrated Optics in Sensors: Advances Toward Miniaturized Systems for Chemical and Biochemical Sensing," *Integrated Optical Circuits and Components*, E.J. Murphy (Ed.), (M. Dekker, New York, 1999).
2. D. Clerc and W. Lukosz, "Integrated optical output grating coupler as refractometer and (bio-) chemical sensor," *Sensors and Actuators B*, Vol. **11**, 461-465 (1993).
3. R. E. Kunz and L. U. Kempen, "Miniature Integrated Optical Sensors," *Proc. SPIE*, Vol. 2068, 69-86 (1994).
4. M. Wiki and R.E. Kunz, "Wavelength-interrogated optical sensors for biochemical applications," *Opt. Lett.* Vol. **25/7**, 463-465 (2000).
5. R.E. Kunz, J. Edlinger, P. Sixt and M.T. Gale, "Replicated Chirped Waveguide Gratings for Optical Sensing Applications," *Sensors and Actuators A*, Vol. **47**, 482-486 (1995).
6. J. Dübendorfer, *Replicated Integrated Optical Sensors*, PhD Thesis Nr. 1190 (University of Fribourg and Paul Scherrer Institute, Switzerland, November, 1997).
7. P.K. Tien, "Light Waves in Thin Films and Integrated Optics," *Appl. Opt*. **10/11**, 2395-2413 (1971).
8. T. Tamir (Ed.), *Guided-Wave Optoelectronics, Electronics and Photonics*, Vol. 26 (Springer, Berlin, 1988).
9. R.E. Kunz, "Gradient Effective Index Waveguide Sensors," *Sensors and Actuators B*, Vol. **11**, 167-176 (1993).
10. R.E. Kunz, J. Edlinger, B.J. Curtis, M.T. Gale, L.U. Kempen, H. Rudigier, and H. Schütz, "Grating Couplers in Tapered Waveguides for Integrated Optical Sensing", *Proc. SPIE*, Vol. 2068, 313-325 (1994).
11. R.E. Kunz and J. Duebendorfer, "Miniature Integrated Optical Wavelength Analyzer Chip," *Optics Letters*, Vol. **20**, 2300-2303 (1995).
12. J. Dübendorfer, R.E. Kunz, E. Schürmann, G.L. Duveneck and M. Ehrat, "Sensing and Reference Pads for Integrated Optical Immunosensors," *Journal of Biomedical Optics*, Vol. **2**, 391-400 (1997).